

**University of West Bohemia  
Faculty of Electrical Engineering**

# **DISSERTATION**

**Design and Modelling of Compact Electromagnetic  
Sensors for EMC Applications**

**Mr. Abdalghfor ALMTROD**

**Pilsen, 2023**



**FACULTY OF ELECTRICAL  
ENGINEERING  
UNIVERSITY OF WEST BOHEMIA**

# **Dissertation**

**to earn the academic degree Ph.D. in the field  
Electrical Engineering**

**Mr. Abdalghfor, ALMTROD**

**Modeling and Simulation in Electromagnetic  
Compatibility**

**Supervisor: Ing. Zdeněk, Kubík, Ph. D**

**Date of the state doctoral examination: 30/06/2022**

**Date of submission of work: 19/10/2023**

## Declaration

I declare that I have elaborated the dissertation thesis individually and have used sources which I cite and list in the bibliography. In the submitted scientific work, the usual scientific procedures are used.

Plzeň, date

.....Mr. Abdalghfor ALMTROD.  
signature

## Acknowledgments

I would like to thank Allah the Almighty for supporting and protecting me in my good and bad days...

I would like to express my sincere gratitude to my supervisor **Ing. Zdeněk Kubík, Ph.D.** for his guidance and support throughout the research process. His feedback, insights, and encouragement were extremely valuable in shaping this dissertation. I am genuinely grateful for his patience, dedication, and constant encouragement, which have motivated me to strive for excellence. I am truly fortunate to have had the privilege of working with such an exceptional supervisor.

I would like to thank the Department of Electronics and Information Technology, Faculty of Electrical Engineering, University of West Bohemia, for allowing me to pursue my graduate studies and for the financial support that made this research possible. I am deeply grateful for the opportunities they provided me to develop my research skills, broaden my perspectives, and refine my analytical abilities.

I would also like to acknowledge my family and friends, who provided me with emotional support and encouragement throughout this challenging journey. Their unwavering belief in me gave me the strength to persevere and overcome the obstacles I encountered.

I would like to thank **Dr. Falih M. Alnahwi** from the Department of Electrical Engineering, College of Engineering, University of Basra, for his guidance and consultations during the internship period.

Lastly, I would like to extend my gratitude to all the ZCU staff who generously shared their time and insights with me, without whom, this research would not have been possible.

## Project leader's statement

I declare that within the SGS-2021-005: Research, development, and implementation of modern electronic and information systems project, in which this dissertation thesis was elaborated, presented results were achieved. The student participated in these results by 100%.

Plzeň, date

.....  
signature

## Abstract

This work presents compact electromagnetic sensors usable for electromagnetic compatibility (EMC) measurements. Currently, the utilized standardized 3D antennas are relatively large in size and, in some cases, not very suitable in terms of their electrical parameters and dimensions. This dissertation focuses on the possibility of realizing and using 2D sensors of compact sizes. Five structures of electromagnetic sensors have been designed, fabricated, and tested at the University of West Bohemia's EMC laboratory. Moreover, the practical verifications of the proposed structures showed promising results. The first design is a broadband Printed biconical dipole (PBD) antenna with a balun feeding method. The projection of a classical biconical antenna has inspired the proposed shape. Furthermore, the balun feeding method provides the wide impedance bandwidth. The second structure comprises of 12 elements Printed log-periodic biconical dipole array (PLPBDA) antenna, where each element is derived as the first design. Moreover, PLPBDA antenna exhibited convenient findings in terms of size reduction and bandwidth enhancement. The third design consists of Dual-stacked log periodic biconical dipole array (DSLBPBDA) antenna by stacking two LPBDA antennas with angles of  $30^\circ$  and  $50^\circ$  for the inner and outer layers. Regarding the EMC requirements, the achieved radiation pattern results of DSLPBDA antenna enabled it to work as a reference antenna for radiated emission and immunity tests. The fourth work proposes three broadband spiral circular magnetic probes for EMC measurement; One Face Three Loops (1F3L), Two Face Three Loops (2F3L), and One Face One Loop (1F1L) structures. Due to its more selective area, the 1F3L structure performs better than the 2F3L structure while the 1F1L structure offers wider bandwidth than 1F3L one due to reduce the parasitic capacitor. The fifth structure demonstrates a novel high-sensitivity magnetic probe switchable from broadband to multi-narrowband via a PIN-diode. The achieved narrowband high sensitivity is also tuned across the most critical applications with the help of the varactor diode. The frequency and radiation characteristics of the proposed antennas in terms of bandwidth, size, gain, antenna factor and radiation pattern are compared with that of the classical antenna offered for sale. Moreover, the early design of switchable broadband magnetic probe is evaluated alongside the classical magnetic probe offered for sale regarding sensitivity, spatial resolution, and isolation. The comparison results of antennas and probes are listed in tables and showed good agreement.

## Keywords

Electromagnetic sensor, Electromagnetic interference, Electromagnetic compatibility, PBD antenna, PLPBDA antenna DSLPBDA antenna, and Magnetic probe.

## Abbreviations

<b>Abbreviation</b>	<b>Full Text</b>
<b>DC</b>	Direct Current
<b>EMI</b>	Electromagnetic Interference
<b>EMC</b>	Electromagnetic Compatibility
<b>GSM</b>	Global System Mobile
<b>GPS</b>	Global Position System
<b>LTE</b>	Long Term Evolution
<b>UMTS</b>	Universal Mobile Telecommunications System
<b>3G</b>	Third Generation
<b>Wi-fi</b>	Wireless Fidelity
<b>WiMAX</b>	Worldwide Interoperability for Microwave Access
<b>WLAN</b>	Wireless Local Area Network
<b>PCB</b>	Printed Circuit Board Technology
<b>UK</b>	United Kingdom
<b>RC</b>	Reverberation Chamber
<b>OATS</b>	Open Area Site Test
<b>SAC</b>	Semi Anechoic Chamber
<b>FAC</b>	Full Anechoic Chamber
<b>VHF</b>	Very High-Frequency Band
<b>UHF</b>	Ultra-High-Frequency Band
<b>ETSI</b>	European Telecommunication System Interference
<b>PAN</b>	Personal Area Network
<b>FBW</b>	Fractional Bandwidth
<b>DUT</b>	Device Under Test
<b>CISPR</b>	International Special Committee on Radio Interference
<b>AF</b>	Antenna Factor
<b>TAF</b>	Transmit Antenna Factor
<b>UFA</b>	Uniform Field Area
<b>CST</b>	Computer Software Technology
<b>HFSS</b>	High Frequency Selected Surface
<b>PEC</b>	Perfect Electric Conductor
<b>FIT</b>	Finite Integration Method
<b>DRGH</b>	Double Ridged Guide Horn Antenna
<b>PBD</b>	Printed Biconical Dipole Antenna
<b>PLPDA</b>	Printed Log Periodic Dipole Array Antenna
<b>RL</b>	Return Loss
<b>TRF</b>	Trust Region Framework
<b>EM</b>	Electromagnetic Waves
<b>AWR</b>	Advance Wireless Revolution
<b>PLPBDA</b>	Printed Log Periodic Biconical Dipole Array Antenna
<b>1F3L</b>	One Face Three Loops
<b>2F3L</b>	Two Face Three Loops
<b>1F1L</b>	One Face One Loop
<b>DSLBPDA</b>	Dual Stacked Log Periodic Biconical Dipole Array Antenna
<b>RE</b>	Radiated Emission
<b>RI</b>	Radiated Immunity

## Symbols

Symbol	Description	Unit	Symbol	Description	Unit
$B$	Magnetic flux density	T	$d_s$	Short measurement distance	m
$D$	Electrical flux density	C/m <sup>2</sup>	$D$	Longest antenna dimension	m
$S$	Cross section area	m <sup>2</sup>	$AF$	Antenna Factor	1/m
$\tau$	Scaling factor	–	$TAF$	Transmit Antenna Factor	1/m
$\sigma$	Spacing factor	–	$A_e$	Aperture Area	m <sup>2</sup>
$\lambda$	Wavelength	m	$P_D$	Power density	W/m <sup>2</sup>
$E$	Electrical field strength	V/m	$P_{out}$	Output power	W
$H$	Magnetic field strength	A/m	$FWB$	Relative bandwidth	Hz
$J$	Electrical current density	A/m <sup>2</sup>	$G$	Gain of isotropic	dBi
$\Phi$	Magnetic flux	Wb	$\eta$	Intrinsic impedance	$\Omega$
$\varepsilon$	Permittivity	F/m	$Z$	Impedance	$\Omega$
$\varepsilon_0$	Absolute permittivity	F/m	$V_L$	Load voltage	V
$\varepsilon_r$	Relative permittivity	–	$r$	Radius	m
$\mu_r$	Relative permeability	–	$w_o$	Tangent distance for DUT	m
$\mu_o$	Absolute permeability	H/m	$w$	Angular frequency	rad/sec
$f$	Frequency	Hz	$p_t$	Transmitted power	W
$\mu$	Permeability	H/m	$\theta_{3dB}$	Beamwidth Angle	°
$\Psi$	Electrical flux	C	$E_{max}$	Maximum field strength	V/m
$i$	Induced current	A	$A_{FH}$	Magnetic antenna factor	S/m
$d_o$	Near field test distance	m	$V_{emf}$	Induced voltage	V
$Q$	Electrical charge	C			



# Contents

<b>1</b>	<b>INTRODUCTION .....</b>	<b>1</b>
<b>2</b>	<b>STATE OF THE ART ANALYSIS.....</b>	<b>3</b>
<b>3</b>	<b>DISSERTATION OBJECTIVES .....</b>	<b>24</b>
<b>4</b>	<b>DISSERTATION METHODOLOGY .....</b>	<b>26</b>
<b>5</b>	<b>MAIN RESULTS ACHIEVED.....</b>	<b>31</b>
5.1	DESIGN OF BROADBAND PRINTED BICONICAL DIPOLE ANTENNA WITH TAPERED BALUN FOR EMC MEASUREMENTS .....	31
	5.1.1 <i>Printed biconical dipole antenna design</i> .....	31
	5.1.2 <i>Feeding method</i> .....	32
	5.1.3 <i>Parametric study</i> .....	33
	5.1.4 <i>Equivalent circuit</i> .....	35
	5.1.5 <i>Fabrication process and measurement results</i> .....	37
	5.1.6 <i>Comparison between the proposed Design and the commercial design</i> ...	42
5.2	DESIGN A COMPACT PRINTED LOG-PERIODIC BICONICAL DIPOLE ARRAY ANTENNA FOR EMC MEASUREMENTS .....	43
	5.2.1 <i>Comparative analysis of conventional and biconical dipoles</i> .....	43
	5.2.2 <i>Printed log-periodic biconical dipole array antenna design</i> .....	46
	5.2.3 <i>Feeding techniques</i> .....	50
	5.2.4 <i>Simulation and measurement results</i> .....	51
	5.2.5 <i>Comparison with the literature reviewed</i> .....	56
	5.2.6 <i>Comparison with the commercial LPDA antenna (HyperLOG® 7060)</i> ... 58	
5.3	DESIGN AND MODELLING OF A STACKED LOG PERIODIC BICONICAL DIPOLE ARRAY ANTENNA FOR RADIATED EMISSION AND RADIATED IMMUNITY TESTS IN EMC MEASUREMENTS .....	60
	5.3.1 <i>Dual stacked log periodic biconical dipole array antenna design</i> .....	60
	5.3.2 <i>Feeding method of the stacked antenna</i> .....	61
	5.3.3 <i>Simulation and measurement results</i> .....	62
	5.3.4 <i>Comparison with SCHWARZBECK types of STLP9129, and STLP9149</i> . 72	

5.4 DESIGN AND MODELLING OF SPIRAL CIRCULAR MAGNETIC PROBE FOR NEAR FIELD MEASUREMENTS IN CST MICROWAVE STUDIO .....	74
5.4.1 <i>Reference board design</i> .....	74
5.4.2 <i>Spiral circular magnetic probe design</i> .....	77
5.4.3 <i>The simulation results</i> .....	78
5.5 SWITCHABLE BROADBAND TO TUNABLE NARROWBAND MAGNETIC PROBE FOR NEAR FIELD MEASUREMENTS.....	82
5.5.1 <i>Switchable Magnetic probe design</i> .....	82
5.5.2 <i>Parametric study</i> .....	89
5.5.3 <i>Biasing circuit and measurement results</i> .....	92
5.5.4 <i>Equivalent circuit of the proposed magnetic probe</i> .....	95
5.5.5 <i>Isolation and sensitivity</i> .....	97
<b>6 CONCLUSIONS.....</b>	<b>99</b>
<b>REFERENCES .....</b>	<b>103</b>
<b>LIST OF STUDENT'S PUBLICATIONS AND OUTPUTS RELATED TO THE DISSERTATION.....</b>	<b>106</b>
<b>OTHER STUDENTS' PUBLICATIONS AND OUTPUT.....</b>	<b>107</b>
<b>ANNEX. A – REPRESENTS THE MEASURED UFA POINTS DISTRIBUTION FOR THE PRACTICAL VERIFICATION OF STACKED ANTENNA .....</b>	<b>108</b>
<b>ANNEX. B – SUMMARIZES THE PRESENTED PROPOSED SENSORS AND THEIR CHARACTERISTICS .....</b>	<b>110</b>

# 1 Introduction

The first appearance of electromagnetic wave equations was by James Clerk Maxwell in 1800. Later, these equations evolved to be the central core of wireless communications. There were few electronic devices, and the researchers in this field did not have to care about environmental degradation or electromagnetic interference (EMI) between these appliances.

Recently, electronic devices have become more popular and smaller in size. According to their applications, the radiation emitted from these devices occupies the electromagnetic spectrum from DC to several GHz. Hence, an EMI will occur between these devices since they share the same range and space [1]. The ability of these devices to stay functional properly without effect on each other is called electromagnetic compatibility (EMC) [2]. The EMI phenomenon arises due to three mandatory aspects; the source of electromagnetic waves (EM), the victim affected by the EM source, and the connecting path between the EM source and the victim. This path determines the EM interference type, which can be either radiated or conducted, as shown in Figure 1 [3, 4].

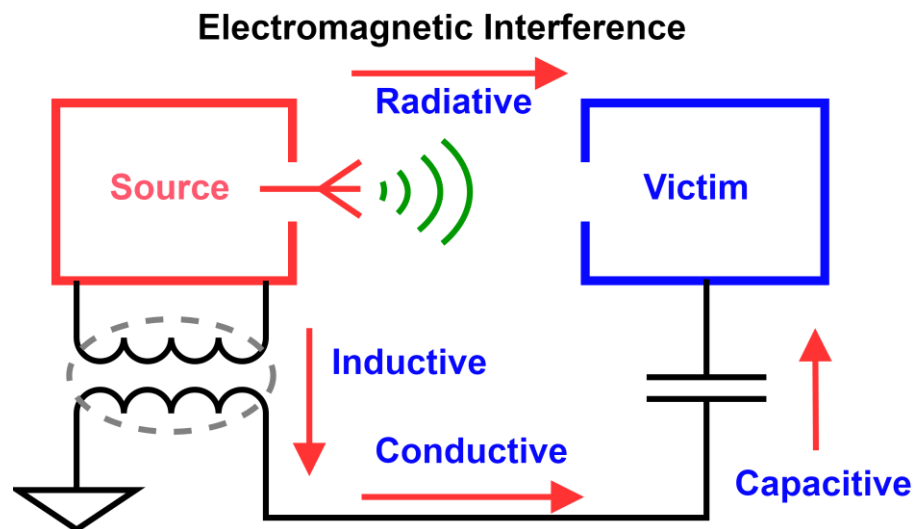


**Figure 1.** The EMI types: Radiative and conductive

Each radiated element has three field zones, a non-radiative reactive field (near-field region), a radiative near-far field region (Fresnel), and a radiative far-field region (Fraunhofer) [5]. The boundaries of these regions are based on their radius  $R$  related to their wavelength and the most extended dimension  $D$  of the element, as shown in Figure 2.

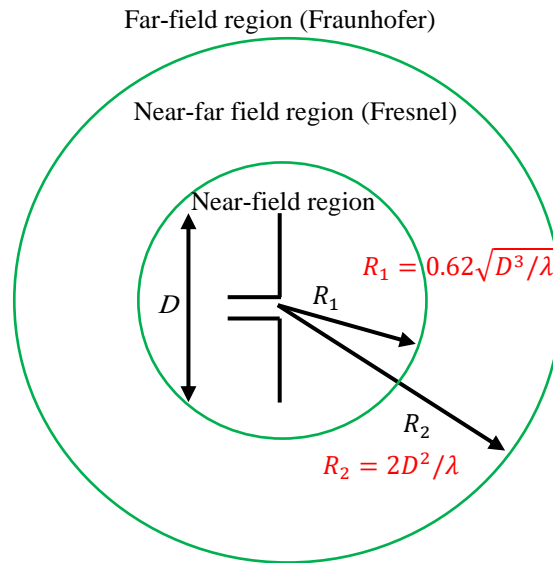
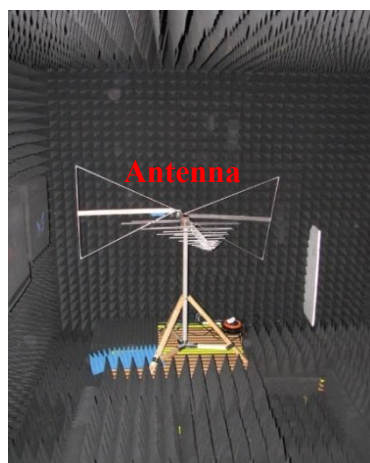


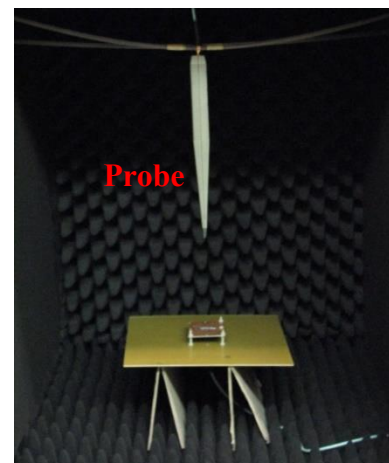
**Figure 2.** Three field regions for any radiated element

The right choice for the EMI measurement method (far-field or near-field) is based on the radiated element zones and the power level of the EM interference source. In particular, the far-field method utilizes a reference antenna to estimate or emit the electrical field inside the EMC chamber for radiated emission or immunity tests [6]. On the other hand, the near-field method uses electric or magnetic probes to collect the induced electrical or magnetic field precisely in the proximity area of the device under the test (DUT) [7], as shown in Figure 3

### Electromagnetic interference measurements



Full Anechoic Chamber  
a)



Radiated EMI near-field Probe  
b)

**Figure 3.** Two methods for measuring EMI: a) the far-field method and b) the near-field method.

## 2 State of the Art Analysis

### 2.1 Microstrip sensors

The sensor is a device that changes the physical quantity like pressure, temperature, light intensity, radiation or distance to an electrical amount, either voltage or current. Since here, we deal with electromagnetic sensors. Therefore, we can define it as a device that senses or detects electromagnetic radiation and changes it to a voltage.

The functionality of electromagnetic sensors can be in two forms based on the electromagnetic field measurement method. For instance, the far-field measurement method uses a reference antenna as a sensor to detect the radiation from the device under the test. In contrast, the near-field measurement method utilizes the magnetic/electric probe like a sensor to detect the magnetic/electric field in the proximity area above the DUT.

Working the electronic devices together in the same spatial space will create an EMI. This interference prevents the compatibility of these electronic devices from working together efficiently. Finding this problem at the operating stage will be too late since replacing the damaged parts caused by interference will cost a lot. Therefore, testing the product for emission and immunity before releasing to the markets shows the compliance of these devices. The EU EMC Directive adopted Laws in 1992 to oblige all electronic devices or appliance manufacturers to submit their products to the EMC test before releasing them into the markets. One of the compulsory parts of this test is the EM sensor, i.e., reference antenna and electric/magnetic probe. The utilized antenna for the EMC measurements should have specific considerations such as wide bandwidth, low fluctuations gain, omnidirectional or directive radiation pattern, and good antenna factor ( $AF$ ) / transmit antenna factor ( $TAF$ ). On the other hand, the magnetic probe has five specifications that every designer should be addressed, like bandwidth, antenna factor, sensitivity, spatial resolution and isolation.

#### 2.1.1 Reference antennas

Far-field measurement test inside the EMC chamber has two types. The emission test uses a reference antenna to estimate the maximum strength field  $E_{max}$  emitted from the DUT. In contrast, the immunity or susceptibility test deploys the reference antenna to emit electromagnetic noise to measure the immunity of the DUT. Moreover, several means were employed to estimate the strength of the electrical field emitted from the DUT: for instance, the reverberation chamber (RC), the open area test site method (OATS), the semi-anechoic

chamber method (SAC), and the fully-anechoic room method (FAR). This work will focus on the reference antenna that are used in the EMC chamber (SAC and FAR).

Many antenna types have served as reference antennas inside the EMC (SAC or FAR) chamber in the bands 30 – 1000 MHz and 1000 – 6000 MHz. The classical biconical and log periodic dipole array antennas usually cover the VHF range of 30 – 1000 MHz, while the double ridged horn antenna covers the UHF band above 1 GHz [8].

The classical antennas are large in size and heavy in weight. Therefore, using printed circuit board technology (PCB) to design compact structures has a lot of advantages, such as compact size, low cost, low profile, and ease of fabricating [9].

On the other hand, microstrip antennas suffer from narrow bandwidth and low efficiency. The limited bandwidth is considered a big issue in EMC applications, making using the monopole and dipole printed antennas as a basic element for the proposed structures is the best way to overcome this issue. Critical parameters must be considered in designing a printed antenna to serve as a reference antenna inside the EMC chamber.

#### **2.1.1.1 Bandwidth**

The typical operating frequency range for EMC measurement applications is 30 MHz to 6 GHz and could be broader or narrower depending on the market in which a product is being sold. The proposed reference antennas are designed usually to work in the band 800 MHz to 2.5 GHz where this band is occupied with different well-known applications which have a high probability of interference, such as global system mobile (GSM) (850 – 900 MHz), 4G LTE (800, 900, 1800, and 2100 MHz) and Wi-fi (2400 MHz) [10]. At the same time, the frequency band 2.5 GHz – 6 GHz should be taken into consideration based on the fact that it contains a set of critical applications like WiMAX (3.5 GHz and 5.3 GHz), mid-bandwidth for 5G (2.5 – 3.8 GHz), Personal Area Network (PAN) (4.8 GHz) and WLAN (5.8 GHz) [5]. Figure 4 presents the most critical applications in the frequency band starting from 100 MHz up to 10 GHz.

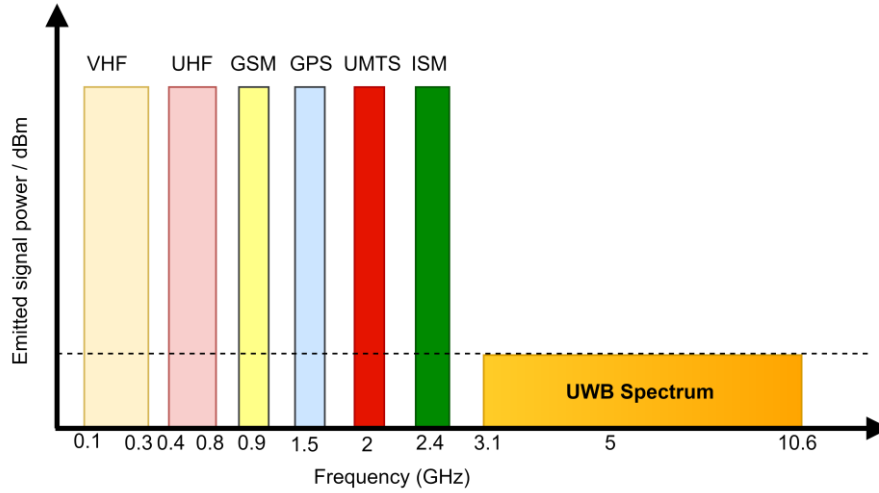


**Figure 4.** Spreading of the critical applications through the spectrum

The matric relative bandwidth  $FBW$  is used to express the percentage of bandwidth increase and can be calculated using equations (2.1) and (2.2).

$$FBW = \frac{f_h - f_l}{f_{av}} \times 100. \quad (2.1)$$

$$f_{av} = \frac{f_h + f_l}{2}. \quad (2.2)$$

where  $f_h$ ,  $f_l$  and  $f_{av}$  denote the high, low and average frequencies, respectively.

### 2.1.1.2 Size

The radiated emission (RE) test and immunity (RI) test are mandatory criteria for EMI measurements. The RE test measures the level of radiation emitted from the DUT, while the immunity or susceptibility test measures the immunity of the DUT against spreading interference. Furthermore, both EMC tests must be performed in the far-field region with a shorter measurement distance  $d_s$ . The shorter measurement distance  $d_s$  are one of the motivations for utilizing a compact microstrip antenna instead of a classical one during the EMI/EMC measurements. I.e., it offers a maximum strength field ( $E_{max}$ ) without increasing the input power.

The radiation pattern of the reference antenna must cover the DUT to achieve  $E_{max}$ . Usually, the DUTs have different dimensions, which makes it hard to cover with one antenna. Therefore, other reference antennas are required to get the  $E_{max}$ . Unfortunately, having many antennas in one EMC laboratory is not the right choice. The alternative solution is to have a small size of reference antenna. The  $E_{max}$  is obtained by changing the shorter measurement distance  $d_s$  according to the dimension of the device under the test. So, the

compact antennas help change the EMC chamber size since it has a higher permittivity for decreasing measurement distance  $d_s$  while maintaining the DUT in the far-field region [11].

The shorter measurement distance  $d_s$  is determined by the largest dimension of the antenna  $D$ , the DUT dimension, and the maximum resonance frequency  $f$  according to CISPR 16–1–2 using equation (2.3) [11, 12].

$$d_s = \begin{cases} \frac{D^2}{2\lambda}, & f > 1 \text{ GHz}, \\ \frac{2D^2}{\lambda}, & f < 1 \text{ GHz}. \end{cases} \quad (2.3)$$

Suppose we have two reference antennas operating up to 6.5 GHz. The first antenna is a classical log periodic dipole array (LPDA) antenna with the highest dimension of  $D = 340$  mm, while the second antenna is a compact size with the greatest extent of  $D = 170$  mm. Using equation (2.3) for both cases, the shorter measurement distance  $d_s$  for the LPDA antenna must be  $\geq 3$  m. On the other hand, the compact-size antenna has a  $d_s$  of about  $\geq 0.6$  m which must be larger than or equal to 1 m, according to [12]. Due to the compact size of the proposed antenna, the measurement distance  $d_s$  could be alternated to 1.25 m in the case of a small DUT, and the illumination area will be 1.5 m making it suitable for most DUTs.

### 2.1.1.3 Antenna factor and transmit antenna factor

#### A. Antenna factor $AF$

The antenna factor represents the ratio of the electrical field strength at the surface of the antenna to the induced voltage on antenna terminals. The standard antenna parameters have limitations that are updated according to the application used. Furthermore, an antenna factor is an essential parameter to compute in EMC applications since it defines the antenna's accuracy and low uncertainty [13, 14].

Since it is hard to evaluate the electrical field strength precisely inside the EMC chamber, the antenna factor can be calculated directly from the gain using equation (2.4) [15]:

$$AF = 20 \log \left[ \frac{2\pi}{\lambda} \sqrt{\frac{2.4}{10^{(G(\text{dBi})/10)}}} \right], \quad (2.4)$$

where  $\lambda$  is the wavelength, and  $G_r$  presents the realized gain of the antenna in dBi.

The aperture area  $A_e$  can be expressed in terms of the gain

$$A_e = \frac{G \times \lambda^2}{4\pi}.$$



The aperture area is equal to the ratio between the power density  $P_D$  and the load power  $P_{out}$ :

$$A_e = \frac{P_{out}}{P_D},$$

where  $P_D = \frac{E^2}{120\pi}$  and  $P_{out} = \frac{V_L^2}{Z}$ .

Since  $P_{out} = A_e \times P_D$ ,

Then  $\frac{V_L^2}{Z} = \frac{G \times \lambda^2}{4\pi} \times \frac{E^2}{120\pi}$ .

For  $Z = 50 \Omega$ :

$$\frac{120\pi}{50} = \frac{G \times \lambda^2}{4\pi} \times \frac{E^2}{V_L^2},$$

$$\frac{E^2}{V_L^2} = \frac{4\pi \times 120\pi}{G \times \lambda^2 \times 50}.$$

By taking the square root for both sides:

$$AF = \frac{E}{V_L} = \sqrt{\frac{480 \times \pi^2}{\lambda^2 \times G}},$$

$$AF = \frac{9.73}{\lambda \sqrt{G}}.$$

Since  $G_{dBi} = 10 \log G$ ,

$$G = 10^{\frac{G_{dBi}}{10}},$$

$$AF = 20 \log \left[ \frac{9.73}{\lambda \sqrt{10^{\frac{G(dBi)}{10}}}} \right].$$

The antenna factor  $AF$  in dB/m is equal to equation (2.4) with some arrangements that can be summarized by dividing the numerator by  $2\pi$  and squaring the resultant for insertion inside the square root:

$$AF = 20 \log \left[ \frac{2\pi}{\lambda} \sqrt{\frac{2.4}{10^{(G(dBi)/10)}}} \right]. \quad (2.4)$$

After calculating of the antenna factor for the compact printed antenna, it must compare with the standard antenna factor values of classical antennas at the same frequency range to verify the antenna accuracy and low uncertainty.

## B. Transmit Antenna Factor TAF

The transmit antenna factor represents the ratio of the electrical field strength at a known distance from the reference antenna to the input voltage in the antenna terminals. The transmit antenna factor can be calculated using equation (2.5).

$$TAF = 20 \log \left[ \frac{\sqrt{0.6}}{r} \sqrt{10^{(G(dBi)/10)}} \right], \quad (2.5)$$

where  $r$  is the distance from the antenna in mm, and  $G_r$  presents the realized gain of the antenna in dBi.

The power density  $P_d$  at distance  $r$  from the antenna can be calculated using the Friss transmission formula.

$$P_d = \frac{P_t G_t}{4\pi r^2},$$

where,  $P_t$  is the power input to the antenna in watts and  $G_t$  is the realized gain of the antenna. Ohm's Law for free space can also calculate power density.

$$P_D = \frac{E^2}{120\pi},$$

where  $E$  is the strength of the electrical field in V/m. Then:

$$\frac{E^2}{120\pi} = \frac{P_t G_t}{4\pi r^2}.$$

Since  $P_t = \frac{V_i^2}{Z}$ .

For  $Z = 50 \Omega$ :

$$\frac{E^2}{120\pi} = \frac{G_t}{4\pi r^2} \times \frac{V_i^2}{50},$$

$$\frac{E^2}{V_i^2} = \frac{1}{r^2} \cdot 0.6 G_t,$$

$$TAF = \frac{E}{V_i} = \frac{1}{r} \sqrt{0.6 G_t}.$$

Since  $G_{dBi} = 10 \log G$ ,

$$G = 10^{\frac{G_{dBi}}{10}},$$

$$TAF = 20 \log \left[ \frac{\sqrt{0.6}}{r} \sqrt{10^{(G(dBi)/10)}} \right], \quad (2.5)$$

where  $r$  is the distance from the antenna and  $G_r$  presents the realized gain of the antenna in dBi.

The antenna factor must be computed during the radiated emission test. In contrast, the immunity test needs the transmit antenna factor to determine the level of the electrical field at the measurement distance  $d_s$ . Although  $AF$  and  $TAF$  have the same units, they are neither identical nor reciprocal.

#### 2.1.1.4 Beamwidth

The beamwidth angle  $\theta_{3dB}$  is the minimum angle between two positions of the main lobe at the half-power. This parameter is also necessary for calculating the minimum dimension of the line tangent to the DUT for the reference antenna  $w_o$  according to the following equation (2.6):

$$w_o = 2 \times d_s \times \tan(0.5 \times \theta_{3dB}), \quad (2.6)$$

where  $d_s$  are the shorter measurement distance between the reference antenna and the DUT, which can be 1 m, 3 m, or 10 m according to the CISPR standards. Furthermore, the reference antenna can change its height  $h$  from 1 m to 4 m if the DUT is large. The computed beamwidth angle of the proposed structure must be compared with that of the classical antenna according to the CISPR standard. Figure 5 presents the EMC measurement setup inside the chamber.

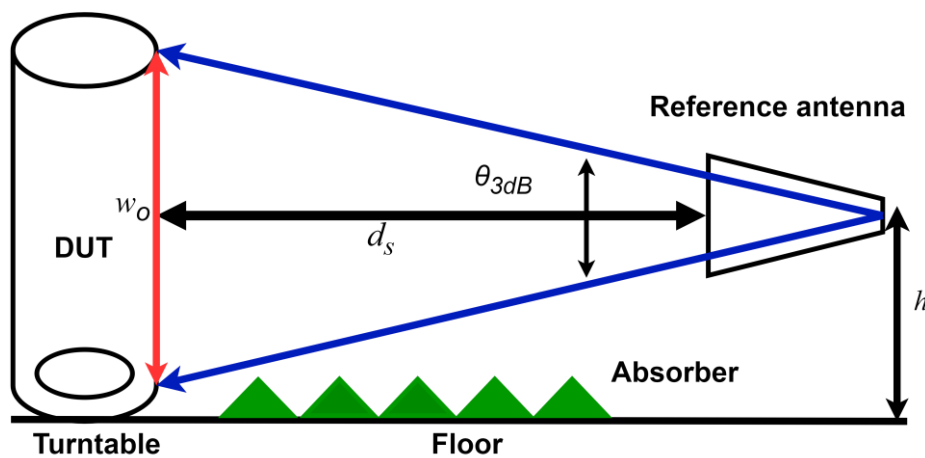


**Figure 5.** Measurements setup inside the EMC chamber, according to the CISPR standard

#### 2.1.2 Microstrip sensors (Magnetic probes)

When the interference source is small, the best choice for EMI measurement is to utilize the near-field method using magnetic and electric probes [16]. The essential part of the sensor consists of a transmission line with a detecting element, either loop for the magnetic probe or a dipole for the electric probe. Furthermore, the electric dipole probe suffers from the disturbance of the DUT by the probe itself, and the induced current  $i$  can be calculated with the capacitive model according to the following equation (2.7):

$$i = jw\varepsilon_0 E_z, \quad (2.7)$$

where  $w$  is the angular frequency in rad/sec,  $\varepsilon_0$  is the absolute permittivity in F/m and  $E_z$  is the electrical field in the z-direction.

On the other hand, the detecting element of the magnetic probe is represented by a conductor loop. Based on Faraday law, the induced voltage  $V_{emf}$  by the probe represents the instantaneous change of magnetic flux inside the loop using equation (2.8):

$$V_{emf} = -\frac{d\varphi}{dt} = -\frac{\partial}{\partial t} \iint B \cdot dS, \quad (2.8)$$

where  $\varphi$  is the flux in Wb,  $B$  is the magnetic field density in T and  $S$  is the cross-section area of the loop in  $m^2$ .

The classical magnetic probes can be easily formed by hand in several shapes like circular and square loops, whereas having low accuracy was the main issue [17]. The printed magnetic probes have grown in the last decade using PCB technology advantages like compact size, accuracy, multilayers, and fabricating ease.

With the analogy of the far-field measurement, the near-field tests can be done in a traditional laboratory rather than an EMC chamber or open area test site (OATS) method because it is less affected by the environments since it serves in the proximity area above DUT. To model the proposed probe, we need a reference board that gives reference values of the magnetic field to compare with the presented probe results. This reference board is necessary to detect the magnetic field. A conventional reference board consists of a cylindrical line of diameter  $d = 1.2$  mm above the ground plane  $h = 2.05$  mm and terminated with the  $50 \Omega$  resistor, as shown in Figure 6. The air separates between the cylindrical line and the ground plane, and this type is well known due to the easy calculation of the electromagnetic field components around the structure using the boundary image equations [18]:

$$E_y = 8K \frac{yzn}{(y^2 + (z+n)^2)(y^2 + (z-n)^2)}, \quad (2.9)$$

$$E_z = 4K \frac{n(y^2 - z^2 + n^2)}{(y^2 + (z+n)^2)(y^2 + (z-n)^2)}, \quad (2.10)$$

$$H_y = -\frac{E_z}{\eta}, \quad (2.11)$$

$$H_z = -\frac{E_y}{\eta}, \quad (2.12)$$

where  $\eta = \frac{\mu_0}{\varepsilon_0} = 377 \Omega$ ,  $K = \frac{\sqrt{2PZc}}{\ln\left(\frac{h+n}{h-n}\right)}$  and  $n = \sqrt{h^2 - a^2}$ .

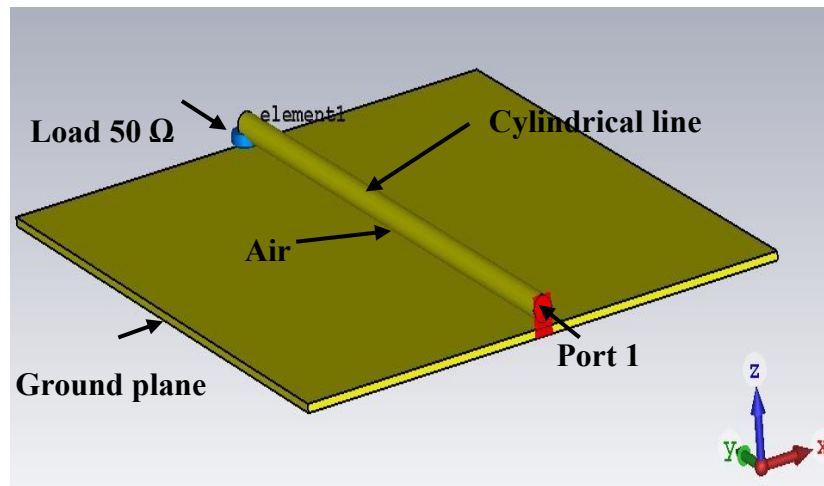


**Figure 6.** The conventional reference plane for the near-field test

The printed magnetic probe has specifications that qualify it as a sensor for estimating the magnetic field in the proximity area above the electronic circuits.

### 2.1.2.1 Bandwidth

The source noise might be spread among multi-frequency bands over the device under the test DUT. Moreover, the broadband magnetic probes cover wide bandwidth, making it an excellent choice to estimate the magnetic field above the electronic circuits. Unfortunately, it suffers from low sensitivity compared to narrow magnetic probes. I.e., narrowband magnetic probes usually have high sensitivity at a specific working frequency. The EMI at multiple frequency bands could be estimated using broadband probes with low sensitivity or multi-narrowband high-sensitivity magnetic probes. Unlike the antenna, the operation bandwidth of the broadband magnetic probe may not be as straightforward to define as it is for antennas. The probe's performance in terms of sensitivity, accuracy, and resonance characteristics across different frequencies should be considered when evaluating its operational bandwidth [19].

### 2.1.2.2 Spatial resolution

The spatial resolution is the ability of the magnetic probe to distinguish between the magnetic fields achieved by two adjacent interference sources. The size of the magnetic loop determines the degree of spatial resolution since it's inversely proportional to the spatial resolution.

### 2.1.2.3 Antenna factor

Analog to the far-field sensor, the near-field magnetic probe also has an antenna factor  $AF_h$  which represents the ratio of magnetic field strength at the loop of the probe to the induced voltage on probe terminals as described in equation (2.13):

$$AF_h = \frac{H}{V_L} = -\frac{1}{j\omega\mu nS}, \quad (2.13)$$

where  $n$  is the number of turns. According to Faraday's law, the induced EMF can be calculated using equation (2.14):

$$V_{emf} = -jn\omega\varphi, \quad (2.14)$$

and since the flux is equal to  $\varphi = B.S$ . Therefore,

$$V_{emf} = -j\omega nB.S,$$

and since the magnetic flux density is equal to  $B = \mu.H$  Therefore,

$$V_{emf} = -j\omega\mu n.H.S,$$

$$AF_h = \frac{H}{V_L} = -\frac{1}{j\omega\mu nS}, \quad (2.13)$$

This factor is beneficial for finding the magnetic field distribution above the DUT by multiplying the induced voltage across the probe terminals extracted from the CST Microwave studio with MATLAB's calculated antenna factor.

### 2.1.2.4 Sensitivity

This factor measures the strength of the induced magnetic field of the designed probe above the reference plane. Typically, a 2 mm height between the designed sensor and the reference board takes as a reference for measuring the sensitivity. This factor can be estimated using two methods; first, it represents the mutual coupling between the designed magnetic probe and the reference board (S21 parameter). Second, by measuring the magnetic field distribution with distance which tell the detection accuracy. Figure 7 shows the setup of measuring the S21 parameter of the designed probe.

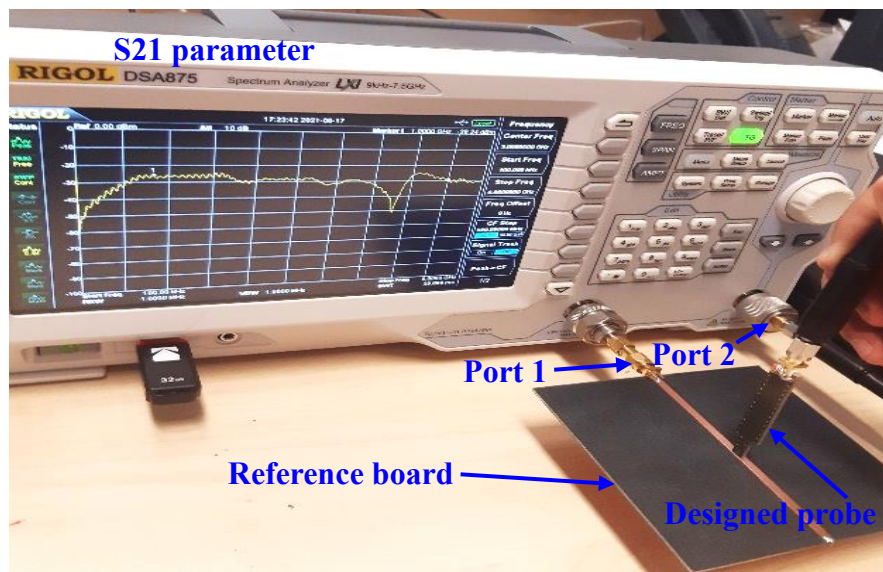


**Figure 7.** Measurement setup of the designed probe in the near-field

### 2.1.2.5 Isolation

Isolation is one of the critical parameters of magnetic probe design, i.e., it represents the ability of the magnetic probe to suppress the unwanted electrical field. Each probe can sense both electrical and magnetic fields. Since we deal with the magnetic field, the electrical field is undesired. The isolation represents the difference between magnitude of these fields in dB which they can be evaluated from the S12 parameter. Moreover, the same S12 parameter gives us the E and H field values according to the probe's orientation regarding the reference trace, as shown in Figure 8; orthogonal or parallel. In the near field area, the E and H field have  $90^\circ$  between them, but they are out of phase.

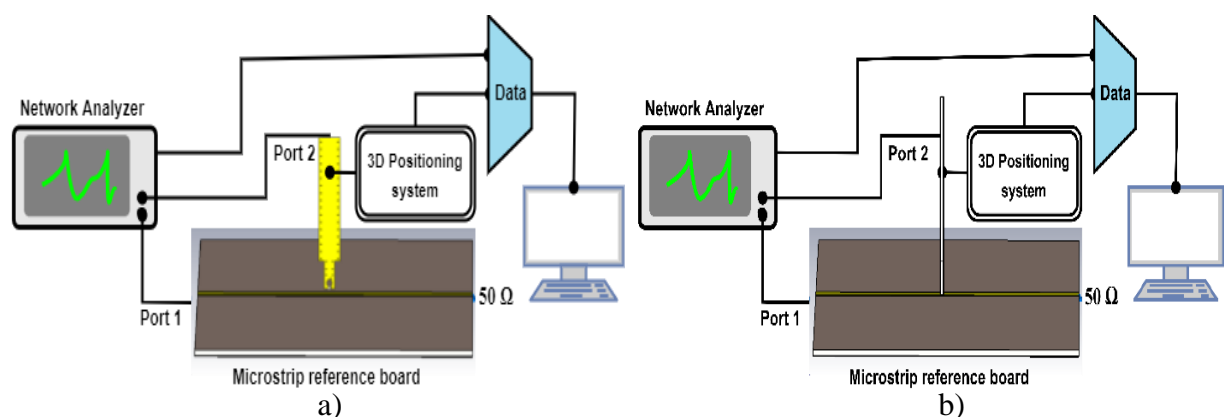


**Figure 8.** Isolation measurement setup in the near field, a) H-field, and b) E-field

The shielded magnetic probe has high isolation and is more sensitive to the magnetic field than electrical one. The typical shielding covers the structure with a perfect electrical conductor (PEC), as depicted in Figure 9, consisting of two copper layers connected through

vias. Moreover, it has a gap at the centre of the shielded layers to create an open circuit for the electrical current, thus minimizing the electrical field.

It is worth mentioning that there is a trade-off between spatial resolution and sensitivity in the magnetic probe design since both are related directly to the size. In particular, the spatial resolution is inversely proportional to the size. Therefore, the compact size will make the probe more selective and accurate but less sensitive. Designing a small-size magnetic probe for higher accuracy is the best solution since the sensitivity can be enhanced using other facilities like a preamplifier [20].

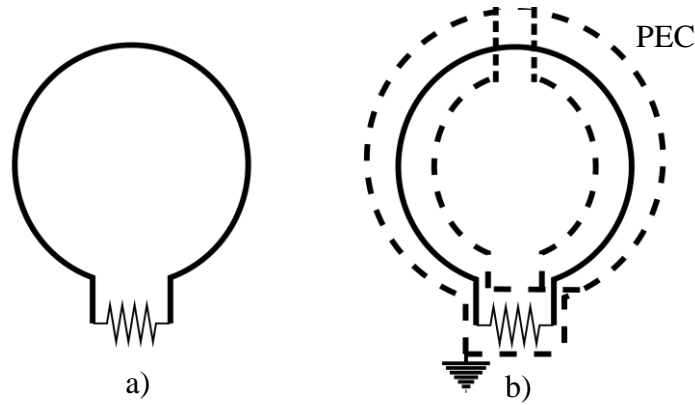


**Figure 9.** Different magnetic probe design a) unshielded probe and b) shielded probe

## 2.2 Simulation in CST Microwave Studio

Modelling and simulating reference antennas and magnetic probes can be performed using various Software tools, such as Ansys HFSS, CST Microwave Studio, etc. The whole structures' modeling and simulation processes in this work will be performed using CST Microwave Studio based on the Finite Integration Technique (FIT) [21].

In 1976, Weiland proposed the Finite Integration Technique. This method is based on discretizing the volume into vertical and horizontal mesh grids to have orthogonal Cubic's, one for the electrical and the other for the magnetic fields, as shown in Figure 10. Moreover, each finite mesh will be solved using Maxwell equations' integral form as follows.

The integral form of Maxwell equations is:

$$\oint \vec{E} \cdot d\vec{A} = - \int \frac{d\vec{B}}{dt} \cdot d\vec{A} , \quad \oint \vec{H} \cdot d\vec{A} = - \int \left( \frac{d\vec{D}}{dt} + \vec{J} \right) \cdot d\vec{A} . \quad (2.15)$$

$$\oint \vec{D} \cdot d\vec{A} = - \int \rho \cdot dv , \quad \oint \vec{B} \cdot d\vec{A} = 0 . \quad (2.16)$$



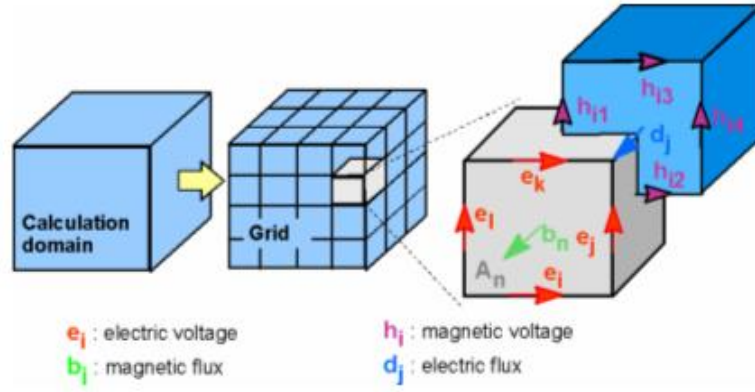


**Figure 10.** The mesh system of finite integration technique

### 2.2.1 Maxwell grid equations

The Maxwell grid equations are necessary to solve electromagnetic problems described by these two orthogonal mesh grids. The first loop or grid  $\mathbf{G}$  is represented in terms of the integral form of the Maxwell equation (Faraday law) by summing the electrical voltage along the loop to get the time-varying of magnetic flux with a different sign and orthogonal direction to the surface. The previous process will repeat itself by applying the integral form of the second Maxwell equation (Ampere law) to the second grid  $\tilde{\mathbf{G}}$  (orthogonal to the first grid).

$$e_i + e_j - e_k - e_l = -\frac{d}{dt} b_n, \quad h_{i1} + h_{i2} - h_{i3} - h_{i4} = -\frac{d}{dt} d_n + j,$$

$$[1 \quad 1 \quad -1 \quad -1] \begin{bmatrix} e_i \\ e_j \\ e_k \\ e_l \end{bmatrix} = -\frac{d}{dt} [b_n], \quad [1 \quad 1 \quad -1 \quad -1] \begin{bmatrix} h_i \\ h_j \\ h_k \\ h_l \end{bmatrix} = -\frac{d}{dt} [d_n],$$

$$\mathbf{C} \mathbf{e} = -\frac{d}{dt} \mathbf{b}, \quad \check{\mathbf{C}} \mathbf{h} = -\frac{d}{dt} \mathbf{d} + \mathbf{j}. \quad (2.17)$$

$$\check{\mathbf{S}} \mathbf{d} = \mathbf{q}, \quad \mathbf{S} \mathbf{b} = \mathbf{0}. \quad (2.18)$$

where  $\mathbf{C}$  and  $\check{\mathbf{C}}$  is the curl factor for the first and second grids, respectively.

$\mathbf{S}$  and  $\check{\mathbf{S}}$  is the divergence factor for the first and second grids, respectively.

Then we have the material equations:

$$\vec{\mathbf{D}} = \varepsilon \vec{\mathbf{E}} \Leftrightarrow \mathbf{d} = \mathbf{M}_\varepsilon \mathbf{e}, \quad (2.19)$$

$$\vec{\mathbf{B}} = \mu \vec{\mathbf{H}} \Leftrightarrow \mathbf{b} = \mathbf{M}_\mu \mathbf{h}, \quad (2.20)$$

$$\vec{\mathbf{J}} = \sigma \vec{\mathbf{E}} + \vec{\mathbf{J}}_s \Leftrightarrow \mathbf{j} = \mathbf{M}_\sigma \mathbf{e} + \mathbf{j}_s. \quad (2.21)$$

These matrix equations can solve electromagnetic field problems using spatial discretization with two orthogonal mesh grids.

## 2.3 Literature review

### 2.3.1 Sensors for far field measurement

Several structures of the antennas were proposed to utilize to work as a reference in the far field measurement. The authors in [22] presented the characteristics of  $AF$  for sleeve dipole antenna for EMC measurements. The changing of dipole parameters offered a size reduction of 86% compared to the classical biconical antenna of the same characteristics. In [23], authors improved the performance of the classical LPDA antenna with the help of a saw-tooth shape feedline technique. The vertical component of the electrical field is eliminated by arranging the successive dipoles in the same horizontal plane. Ref [24] proposed a complimentary LPDA antenna with circular polarization. The proposed structure consisted of an extra set of dipoles arranged orthogonal to the original LPDA antenna, reflecting a circular polarization without any hybrid junction. A double ridge guide horn (DRGH) antenna with a linearly tapered width was presented in [25]. Consequently, the effective radiation aperture was increased, and the beamwidth was reduced compared to conventional 1 – 18 GHz DRGH.

Classical antennas are large in size and heavy in weight. Therefore, PCB technology for antenna design is the best choice for this purpose. The microstrip antenna has many advantages: its low cost, low profile, and easy fabricating [9]. On the other hand, it suffers from narrow bandwidth and low efficiency. The limited bandwidth is considered a big issue in EMC applications, making using the monopole and dipole printed antennas as a basic unit for the proposed structures is the best way to overcome this issue.

**In 2009**, a printed log-periodic dipole array (PLPDA) antenna was presented to work as EMI Sensor. This structure was based on an FR-4 substrate with relative permittivity of  $\epsilon_r = 4.3$  and loss tangent  $\tan \delta = 0.002$ . Furthermore, the achieved bandwidth covered three influential bands from 625 MHz to 2.6 GHz. The antenna boasted a robust design comprising ten printed elements, five on each side, seamlessly connected to a tapered feeding line that commences with a width of  $w_f = 3$  mm and culminates in 20 mm. The reshaping process was applied on the 2<sup>nd</sup>, 3<sup>rd</sup>, 4<sup>th</sup>, and 5<sup>th</sup> elements to enhance return losses, bandwidth, and gain by adding a triangular shape on the top side of each of the abovementioned four elements. This structure was designed and optimized using commercial Software IE3D. Additionally, the structure has an optimized size of  $0.412 \times 0.35 \lambda$ , and relative bandwidth of 125% [26].

**In 2016**, a compact PLPDA antenna that operates from 800 MHz to 2.5 GHz was presented. The design started with evaluating the antenna parameters in free space

conditions, and then modifications were done to take into account the effective dielectric substrate ( $\epsilon_{eff}$ ). This design was based on an epoxy FR-4 substrate with relative permittivity of  $\epsilon_r = 4.3$  and loss tangent  $\tan \delta = 0.002$ . According to the desired gain value of 6.5 dBi, the corresponding scaling and spacing factors were 0.78 and 0.14, respectively. The achieved return loss RL with nine dipoles was not satisfying the condition ( $VSWR < 2$ ). It did not have  $-10$  dB for the whole frequency band. There were two frequency bands ( $RL > -10$  dB); one started from 1 GHz to 1.05 GHz, and another commenced from 1.88 GHz to 1.985 GHz. Therefore, three extra dipoles were added, and the whole structure was optimized using CST Microwave Studio to achieve the optimized size. The final design had 12 dipoles with a small size of  $0.426 \times 0.4 \lambda$  and a relative bandwidth of 103% [27].

**In 2016**, the authors in [28] proposed a balanced method for feeding the PLPDA antenna to cover a wide range from 500 MHz to 3 GHz using 12 dipoles. The bandwidth enhancement and size reduction achievements were compared with PLPDA achievements in [27], where both antennas had the same number of dipoles and were based on an FR-4 substrate. The balance feeding method was utilized to compensate for the effect of soldering coaxial cable shield. It thus enhanced the radiation characteristics reflecting an almost flat gain of 7 – 7.5 dBi, with a scaling factor of 0.86 and a spacing factor of 0.15. These achievements made the design an excellent choice to use as a reference antenna in EMC measurement. The overall size was  $0.443 \times 0.25 \lambda$  while the relative bandwidth was 143%.

**In 2017**, the authors of [29] demonstrated an optimized shape of a compact PLPDA antenna designed with 48 elements. The overall dimensions were optimized using CST Microwave studio built-in optimizer to get wideband coverage from 0.55 GHz to 9 GHz. Size reduction was achieved using the hat-loaded enhancement method on the first three elements and T-shape loaded on the following three elements. Simultaneously, feedline meander and trapezoidal stubs were utilized to provide good impedance matching and bandwidth enhancements of 177%. This design was based on Rogers RO4003 substrate with relative permittivity of  $\epsilon_r = 3.55$  and loss tangent  $\tan \delta = 0.0027$ . The scaling factor and the spacing factor were 0.93 and 0.173, respectively. The measured gain had high fluctuations of 2.48 to 7.89 dBi, while the overall optimized size was  $0.49 \times 0.355 \lambda$ .

**In 2018**, Trusted Region Framework (TRF) algorithm was used to achieve the optimal parameters of PLPDA antenna for EMC application. Initially, a structure like in [27] was utilized with 12 dipoles element, a scaling factor of 0.86, and a spacing factor of 0.14 based on FR-4 substrate (relative permittivity  $\epsilon_r = 4.3$  and loss tangent  $\tan \delta = 0.002$ ), where the

whole parameters had been optimized. This design had a suitable impedance matching from 800 MHz to 2.5 GHz, with a fluctuated gain of 4.5 – 6.3 dBi. Using the TRF algorithm did not improve bandwidth better than [27]. On the other hand, it provided size reduction. The overall size was  $0.426 \times 0.373 \lambda$  while the relative bandwidth was 103% [30].

**In 2018**, the wide bandwidth of shortened LPDA antenna was achieved using printed dual-band dipole elements instead of the classical dipole. These dipoles were optimized in a manner where their frequency bands overlapping led to wideband behaviours (0.5 – 10 GHz), reflecting bandwidth enhancement of 181% and size reduction of 40%. The number of dipoles used was 25 compared to 40 elements for the conventional dipole. Furthermore, Rogers RO4003 substrate (relative permittivity  $\epsilon_r = 3.55$  and loss tangent  $\delta = 0.0027$ ) was used with a scaling factor of 0.916 and a spacing factor of 0.16. The overall size was  $0.36 \times 0.43 \lambda$ , and the realized gain fluctuated 3 – 6 dBi [31].

**In 2020**, wide bandwidth (0.4 – 8 GHz) PLPDA antenna was obtained. The bandwidth enhancement had gotten from changing the shape of the most extended dipole into a triangular and optimizing the last four dipoles' length. This antenna was intended to serve as a reference antenna in the EMC measurement since it had a wide bandwidth (relative bandwidth of 180%) and size reduction of 29%. It did not have  $-10$  dB for the whole frequency band, where there were three frequency bands ( $RL > -10$  dB), one from 0.6 to 0.8 GHz, another from 1 to 1.2 GHz and the last one from 1.5 to 1.7 GHz. The authors hypothesized that further improvement of return losses could be obtained for the whole frequency band by replacing the proposed design's 22<sup>nd</sup>, 23<sup>rd</sup> and 24<sup>th</sup> dipole elements with triangular dipoles. This antenna consisted of 25 dipole elements fabricated on an FR-4 substrate with a scaling factor of 0.9 and a spacing factor of 0.16. The realized gain had many fluctuations of an average value of 5.5 dBi, and the overall size was  $0.36 \times 0.37 \lambda$  [32].

**In 2021**, the authors in [33] presented an ultra-wideband (3 – 18 GHz) dual-stacked log-periodic dipole array (DSLPPDA) antenna. Furthermore, this structure was proposed to tackle both goals, gain improvements and size reduction. For instance, the achieved maximum gain was 11.75 dBi with a small size of  $0.905 \times 0.379 \times 0.559 \lambda$ . Both E and H planes radiation patterns were directive with almost the same power value, making the proposed design a good candidate as a reference antenna for immunity test in EMC measurement.

### 2.3.2 Sensors for near field measurement

Testing of compliance of electronic devices at the final stages is performed according to the EMC regulations. However, these tests required expensive equipment and tools. The statistical data obtained from the EMC tests ensured that more than 85% of the DUT failed to pass the test the first time. Thus, the pre-test or pre-compliance test is strongly recommended to increase the chance of getting better compliance test results and decrease the number of tests, and in this case, the EMC measurement will be part of the design procedures [20].

The radiation above the PCB arises from the current movement through traces due to the differential mode, which acts as a small magnetic loop and radiates in the far-field and near-field regions. As mentioned before, far-field radiation can be detected using a reference antenna. On the other hand, the near-field radiation could affect the other components in the same device or nearby devices and the far-field measurements may not detect this radiation. Therefore, the magnetic probes are utilized to accurately estimate the magnetic field radiated by these devices since the measures will perform in the proximity area above the PCB.

Electromagnetic probes measure the interference when the radiation source power is relatively minor such as detecting the magnetic field surrounding the PCB. In general, electromagnetic probes can be electrical or magnetic probes. These probes need a small area (reference board) to compare the reference field and the field achieved from the designed probe. This reference board will simulate the actual DUT in the simulation software [34]. Ordinary magnetic probes can be fabricated by hand with a circular or elliptical loop. Therefore, they are unsuitable for high-resolution measurements due to low accuracy [35].

On the other hand, microstrip magnetic probes have the advantages of low cost, low profile and easy fabrication, making them suitable for high-resolution magnetic field measurements [9]. The broadband magnetic probes cover wide bandwidth, making them an excellent choice to estimate the magnetic field above the electronic circuits. Unfortunately, they suffer from low sensitivity compared to the narrow magnetic probes that transmit more power to the DUT than broadband magnetic probes.

**In 2005**, a novel rectangular broadband (up to 7 GHz) magnetic probe was presented. The emission of the electromagnetic field from the ground plane was suppressed effectively by an adopted tapered transition between the rectangular loop and the proposed probe's coplanar waveguide  $50\ \Omega$  transmission line and air-bridge coplanar grounds connections. This transition eliminated the capacitive effect and enhanced the operation bandwidth compared to the conventional probe with the same covering band. The results were verified

using S-parameter and H-field distribution over the reference plane. The presented structure offered sensitivity in terms of S21 parameter of about  $-40$  dB at 1 GHz and reached up to  $-25$  dB at 7 GHz. However, it performed better than the conventional one, especially at 2 GHz and 6 GHz, reflecting enhancement in isolation [36].

**In 2009**, a printed novel circular magnetic broadband (up to 9 GHz) probe was proposed to serve as a sensor for near-field measurement [19]. The proposed probe was built on fiberglass microwave substrate FR-4 with relative permittivity of  $\epsilon_r = 4.4$  and thickness of  $h = 0.8$  mm. A group of quasi-periodic notches was milled in the feeding line to work as a band-stop filter to eliminate the probe's self-resonance. Furthermore, the proposed structure had high accuracy in detecting the magnetic field with high isolation by suppressing the unwanted electrical field.

**In 2013**, highly sensitive resonance magnetic probe for measuring radio-frequency interference was presented in [37]. The enhancement in sensitivity came from incorporating the LC resonance circuit in differential mode with Marchand balun. Moreover, 8.63 dB sensitivity enhancement in terms of the S21 parameter was obtained at the resonance frequency of 1.57 GHz. Application of the fabricated structure of this probe in measuring the PCB traces and in the actual world cell phones showed its validity.

**In 2014**, the design and simulation of a high-sensitive resonance electrical probe operating at 1.57 GHz were introduced [38]. The designed probe consisted of LC resonators followed by quarter-wavelength transformers of the resonator, achieving optimal power transformation at 1.57 GHz. This design was dedicated to sensing the changing voltage source of the device under the test. Moreover, the sensitivity enhancement was more than 6.6 dB in terms of the S21 parameter compared with the result of broadband equivalent size probe.

**In 2015**, a tuneable resonance magnetic probe was designed, fabricated, and investigated in [39]. The proposed structure used a varactor diode to switch the frequency bands among the GSM900, UMTS, and GPS applications. 7 – 9 dB enhancement in sensitivity was achieved by comparing the achieved sensitivity at the three frequency bands above with the sensitivity of a broadband magnetic probe of the same size. The authors in [39] used Advance design system (ADS) software to model the equivalent circuit of this probe, and the measurement results showed good agreement with the simulation results from ADS.

**In 2016**, an ultra-band up to 20 GHz magnetic probe was proposed in [40]. The proposed probe utilized a via-fence technique to suppress the resonance at the operating

frequency, making S21 parameter smoother. Moreover, the via-fence technique did not provide a flat transition for the whole frequency band. For instance, the sensitivity in terms of S21 parameter was about  $-40$  dB at 2 GHz, then reached up to  $-30$  dB at 12 GHz and came back again to  $-40$  dB at 20 GHz.

**In 2017**, a miniaturized broadband magnetic probe for near-field measurement was presented in [17]. It was based on an FR-4 substrate (thickness = 0.8 mm, relative permittivity  $\epsilon_r = 4.4$ , and loss tangent  $\tan \delta = 0.002$ ) with three layers – the top and bottom for shielding while the middle layer acts as a strip-line. Moreover, the sensitivity had a good value in terms of the magnetic field distribution. At the same time, the high spatial resolution was achieved with  $800 \times 800$   $\mu\text{m}$  aperture slot, reflecting a 20% size reduction compared to the conventional probe operating at the same frequency range from 1 MHz to 1 GHz.

**In 2018**, an ultra-wideband miniature magnetic probe with a high spatial resolution was presented in [41]. The operating frequency was extended by reducing the parasitic inductance and capacitance using small loop and tapered transition techniques. Moreover, the presented probe worked up to 30 GHz with good sensitivity in terms of an S21 parameter of about  $-30$  dB. At the same time, a high spatial resolution was achieved with a  $250 \times 250$   $\mu\text{m}$  aperture slot with the ability to detect the magnetic field in small devices. The designed probe suffered from high sensitivity fluctuations through the operating band.

**In 2020**, a broadband small shielded magnetic probe for magnetic field measurement was presented in [42]. The structure was based on an FR-4 substrate and consisted of sticking up four layers. Furthermore, using an inverted G-shape inductive line, enhanced the relative sensitivity by about 5 dB for the covering band from 100 MHz to 6 GHz. The via, fence and metal canned techniques were utilized simultaneously to suppress unwanted electrical fields.

**In 2021**, a wideband printed magnetic probe for near-field measurement was designed and studied [20]. The design intended to work as a sensor for EMI interference during the design process for the pre-compliance EMC measurement. Moreover, the structure was based on a standard PCB stuck-up technique with six layers; the top and bottom for insulating the probe and providing pads to connect SMA, the 2<sup>nd</sup> and 5<sup>th</sup> layers for shielding, and the 3<sup>rd</sup> and 4<sup>th</sup> layers for symmetrical loop tracks. The simulation and measurement results showed a flat sensitivity response in the S21 parameter with an average value of about  $-27$  dB through the whole frequency bands from 180 MHz to 6 GHz.



## 2.4 Identifying research gap

**Section 2.1** provides the characteristics of electromagnetic sensors for far field and near field measurements. In **Section 2.2**, the simulation mechanism for modelling these sensors in CST is described, and **Section 2.3** reports their literature reviews. Based on these sections, the study problems are summarized and the motivation is explored as follows.

During far field EMC measurements in EMC chambers, classical antennas are typically use, which could be large and heavy (depends on the frequency range). Unfortunately, these antennas cause several issues.

- A. To ensure that the DUT (device under test) is in the far field of the transmitting antenna, a large measurement distance is required due to the antenna's size. However, this creates an issue of increasing the input power to achieve maximum electrical strength at the DUT point which can result in excessive power consumption.
- B. Test configuration issue: When the large-sized antenna is vertically oriented, it can interfere with the ground plane and cause reflections and scattering of electromagnetic waves. This can alter field patterns and potentially affect the accuracy of measurements, as shown in Figure 11. Such interference can have a negative impact on the quality and reliability of EMC test results when the testing antenna has big size and excecng the standand distance with the ground (25 cm).

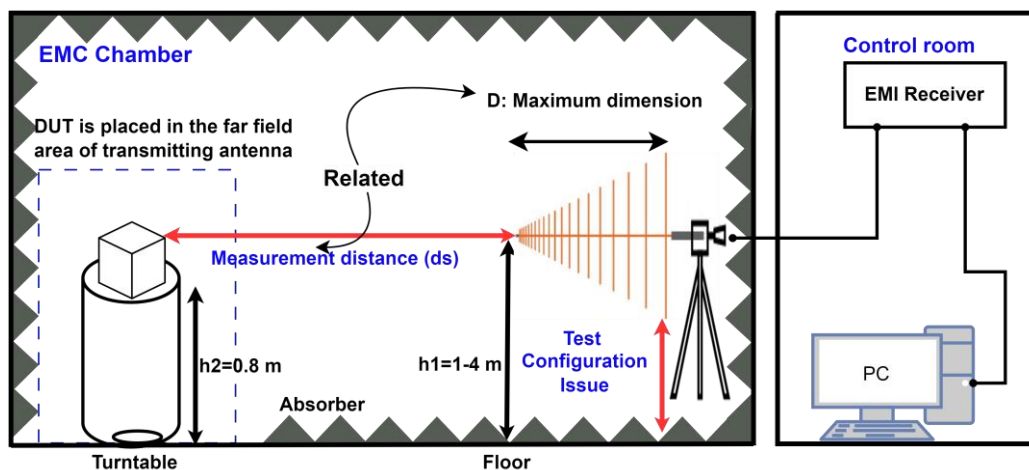


**Figure 11.** EMC measurements setup

However, due to their considerable size and weight, handling and maneuvering them can be challenging, particularly when they need to be repositioned or replaced to meet the requirements of EMC tests. This may cause delays in the testing process, as it increases setup time and effort.



To address these issues, compact antennas have been designed for EMC measurements, taking advantage of their small size and light weight to overcome the challenges posed by large measurement distances and test configurations. This simplifies the process of replacing or repositioning the antenna during the required EMC tests ( radiated emission or immunity test).

For near field measurements, narrowband and wideband magnetic probes are often utilized.

- A. A narrowband magnetic probe is designed to measure the magnetic field component of the electromagnetic radiation emitted by the DUT at a specific frequency or a narrow range of frequencies. These probes are typically tuned to a specific frequency using a resonant circuit. The advantage of using a narrowband magnetic probe is that it provides a higher sensitivity and selectivity at the desired frequency. This makes it suitable for detecting and analyzing specific sources of EMI or identifying resonant frequencies of the DUT. However, the narrowband nature of the probe restricts its applicability to a limited frequency range, requiring different probes for different frequencies or a scanning technique to cover a wider range.
- B. A wideband magnetic probe is designed to capture a broader range of frequencies. It does not have a resonant circuit and can measure magnetic field emissions across a wide frequency spectrum. The advantage of using a wideband magnetic probe is its versatility, as it can cover a wide range of frequencies without the need for tuning or switching probes. This makes it suitable for general EMI troubleshooting and characterization of devices with broadband emissions. However, wideband probes typically have lower sensitivity compared to narrowband probes at specific frequencies. They may also have reduced selectivity, making it harder to isolate and identify specific sources of interference.

The contribution of this field is to use the advantages of both types by design and modelling a novel type of magnetic probe for pre-compliance test which has high sensitivity, desired bandwidth and consumes less time during measurements.

### 3 Dissertation Objectives

After summarizing the problem statements of the far and near fields EMC measurements in the previous section, the motivation of this dissertation is to solve these issues by designing new types of EMC sensors and tackling the most influential parameters, especially in size, weight and bandwidth.

The dissertation objectives summarize using the PCB technology features to build electromagnetic sensors for far-field and near-field measurements inside the EMC chamber.

#### 3.1 Far field sensors

Three compact antennas are proposed for different far field measurements inside the EMC chamber as follows.

1. Create a small printed biconical dipole (PBD) antenna that can be used for EMC measurements inside a chamber and for quickly evaluating test sites in OATS EMC measurements. This antenna can effectively measure background noise in the frequency band ranging from 700 MHz to 2.3 GHz, which covers a variety of standards such as EN 61000-6-3 / 6-4, EN 55032, EN 50121, etc.
2. Design a compact printed log-periodic biconical dipole array (PLPBDA) antenna for EMC measurements. The proposed antenna is planned to serve as a reference antenna inside the EMC chamber as an alternative to the traditional antenna. It uses a biconical shape of a dipole instead of the usual shape, providing wide bandwidth and reduced size. Moreover, the design is optimized to operate from 0.5 to 6.5 GHz, with consistent gain and an improved antenna factor compared to the classical reference antenna.
3. Design and fabricate a new dual-stacked log-periodic biconical dipole array (DSLBPBDA) antenna for radiated emission and immunity tests. The proposed antenna aims to enhance the accuracy and efficiency of EMC testing, contributing to improved assessment and mitigation of EMI issues. It consists of two LPBDA antennas stacked with angles of 30° and 50° for the inner and outer layers. Furthermore, this design offers almost the same power radiation in both E and H planes, making it suitable for immunity tests by satisfying the conditions for the Uniform field area (UFA) points.

### 3.2 Near field magnetic probes

Two structures of printed magnetic probes are demonstrated to achieve broad bandwidth and high sensitivity goals, as follows:

4. Design and investigate several structures of a circular magnetic probe for near-field measurement (1 MHz to 1 GHz) in CST Microwave studio. The investigation includes, firstly, a comparison between the conventional reference board and microstrip reference board. Then, we compare different loop configurations like one-face three-loops (1F3L), two-face three-loops (2F3L), one-face one-loop (1F1L), and so on. The aim of these investigations is to get a comprehensive idea of the magnetic probes' behaviours of the presented structures and to create a ground plane for the next innovated probe.
5. Design a novel compact size switchable broadband to tuneable multi-narrowband magnetic probe for near-field measurements. The proposed probe is devoted to detecting the magnetic field in broadband (1 – 3.5 GHz) and narrowband range of (3.5 – 6 GHz) with the help of PIN and varactor diodes, respectively. Moreover, isolation techniques like via, and fence are planned to employ in the structure to get high electrical field suppression.

## 4 Dissertation Methodology

The methodology of this work has two phases. The first phase belongs to the far-field measurement by designing three structures of reference antennas for OATS fast evaluation of background noise, radiated emission, and radiated immunity tests, respectively.

The first structure is a printed biconical dipole (PBD) antenna with a tapered balun. It is inspired by a classical 3D biconical antenna projection and works from 700 MHz to 2.3 GHz, as seen in Figure 12. The design is based on the idea that a thicker dipole leads to a broader bandwidth, and this has been changed to a planar biconical to achieve a wide bandwidth. Further investigations will be conducted using CST Microwave Studio to test its ability to function as a reference antenna. These investigations will include the parametric sweep of the biconical angle and the study of different types of tapered balun such as linear, log, etc.

The frequency and radiation characteristics of the antenna should be verified using a Network analyzer and an anechoic chamber, respectively. It is worth mentioning that this antenna can be reconfigured to cover lower / higher frequency bands at the expense of size. For instance, an antenna size of  $297 \times 200$  mm will cover a frequency band from 330 MHz up to 2.3 GHz. On the other hand, increasing the higher frequency band for this design requires changing the sharp lines of the virtual triangular into curvature lines toward the antenna. Moreover, using another software like AWR Microsoft Studio to represent the equivalent circuit of the electromagnetic (EM) structure designed in CST Microwave Studio by lumped elements is another way to verify the analysis of this antenna.

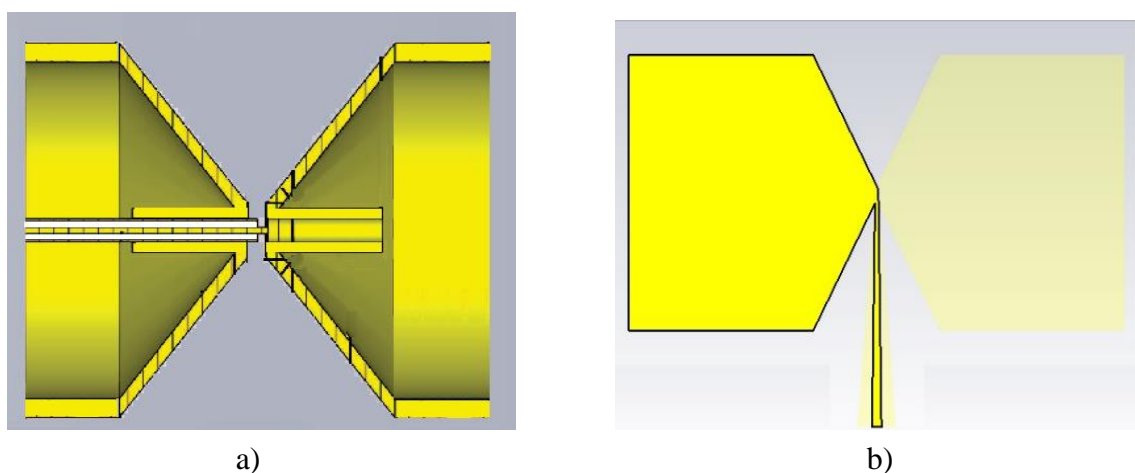


**Figure 12.** The geometrical shape of the biconical antenna, a) 3D configuration [43] and b) 2D printed configuration

The PBD antenna is used as the foundation for the design of a printed log-periodic biconical dipole array (PLPBDA) antenna in the second structure, which is intended for EMC measurements. This design aims to reduce its size and enhance its bandwidth by substituting the standard dipole of a PLPDA antenna with biconical shape dipoles, as illustrated in Figure 13. The procedures start with finding the spacing and scaling factors using a Carrel diagram based on the desired gain. The most critical parameters, like the number of elements, the length of each dipole, the width of each dipole and the spacing between each successive dipole can be calculated using the well-known equations in [27]. However, since we intend to use an FR-4 substrate instead of air, these parameters must be scaled to account for the substrate's effective permittivity.

In the beginning, a comparison between single classical and single bow-tie dipole has been made. The results indicated that the bow-tie dipole can achieve the same resonance frequency with a smaller size than the classical dipole. Additionally, the bow-tie dipole offers a broader bandwidth. These findings suggest that using a bow-tie dipole in a PLPBDA antenna could significantly reduce the size and improve relative bandwidth. Simulation results showed that a PLPBDA antenna yielded a 170% relative bandwidth and 50% size reduction compared to a classical PLPDA antenna.

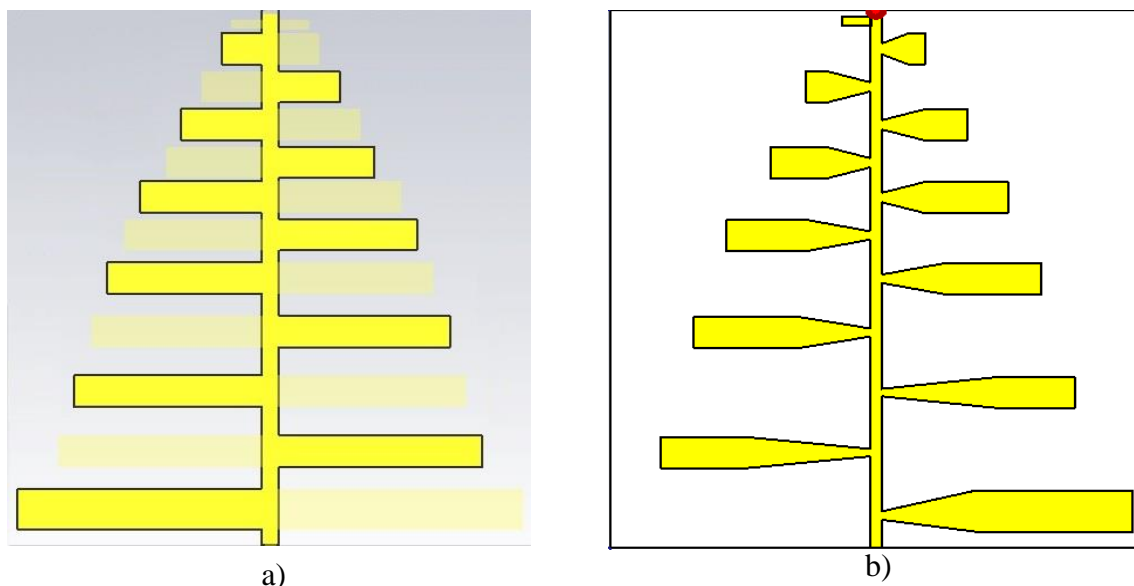


**Figure 13.** The geometrical shape of PLPBDA antenna using a) conventional dipoles and b) bow-tie dipoles

Using the PLPBDA antenna as the primary unit, the third structure designs, models, and analyses a dual-stacked log-periodic biconical dipole array (DSLBPBDA) antenna for radiated emission and immunity tests. The proposed antenna design includes two LPBDA

antennas stacked at  $30^\circ$  and  $50^\circ$  for the inner and outer layers as illustrated in Figure 14. The design exhibits wide impedance bandwidth (0.8 GHz – 6 GHz) and a relatively small size ( $176 \times 157 \times 160$  mm) with the help of the coaxial cable feeding method and biconical dipole technique, respectively. The proposed antenna showed promising results in serving as a reference antenna for radiated emission and immunity tests by fulfilling the design's EMC requirements. For instance, a wide bandwidth antenna with a small size overcomes the test configuration issue, a stable radiation pattern provides a balanced structure and wide beamwidth angles for E and H-field are mandatory to achieve the required level of the electrical field in the UFA.

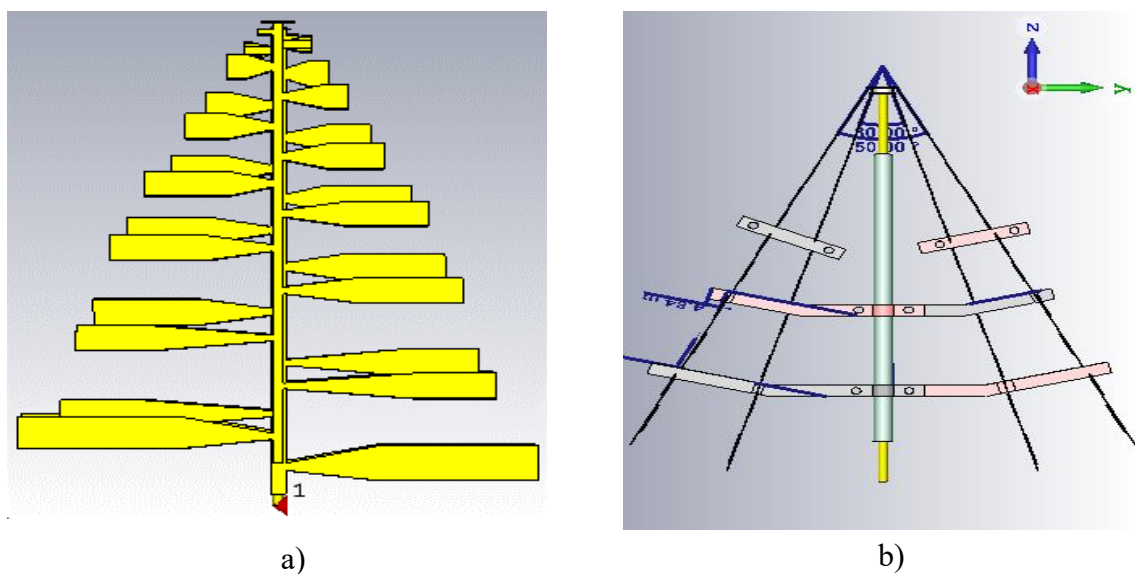


**Figure 14.** The geometrical shape of the stacked antenna, a) front view, and b) side view

The following steps for the previous structures include verification of antenna characteristics that make them suitable to use as a reference antenna inside the EMC chamber instead of the classical one. For instance, wide bandwidth is required for all designs, directive or omnidirectional radiation patterns are selected depending on the intended use, flat realized gain and radiation pattern stability transition reflect a good value of antenna factor compared to the classical one. In addition, the results of each structure will be compared to that of a conventional antenna that is available for purchase.

The second phase belongs to the near-field measurements by designing different structures of magnetic probes to locate the EMI source in the compliance test precisely and this phase contains two parts. The first part consists of a series of investigations, as shown in Diagram 1, to determine the optimum way to design the printed magnetic probe as follows.

The first investigation includes designing and simulating two reference boards: the conventional reference board and the microstrip reference board. The magnetic field distribution above the conventional reference board is calculated first by implementing an algorithm based on image theory in MATLAB. In addition, the conventional and microstrip reference boards are modeled in CST Microwave Studio. It found that the microstrip reference board performs better than the conventional one because the microstrip reference board and the device under the test have the same substrate, probably FR-4.

The second investigation stage compares two printed circular probe configurations, one face three-loop (1F3L) and two face three-loop (2F3L) configurations. These two configurations were tested using the microstrip reference board based on the result of the first investigation. The (1F3L) structure performs better than the (2F3L) configuration in terms of selectivity because it has a more selective area, and thus it can work effectively for the whole frequency band from 1 MHz to 1 GHz.

Based on the results of our second investigation, two configurations have been analysed and studied: one face three-loop (1F3L) and one face one loop (1F1L) configurations. The (1F1L) configuration has wider frequency bandwidth than the (1F3L) design since decreasing the number of turns or loops will directly impact broadening the frequency due to reducing the parasitic capacitor.

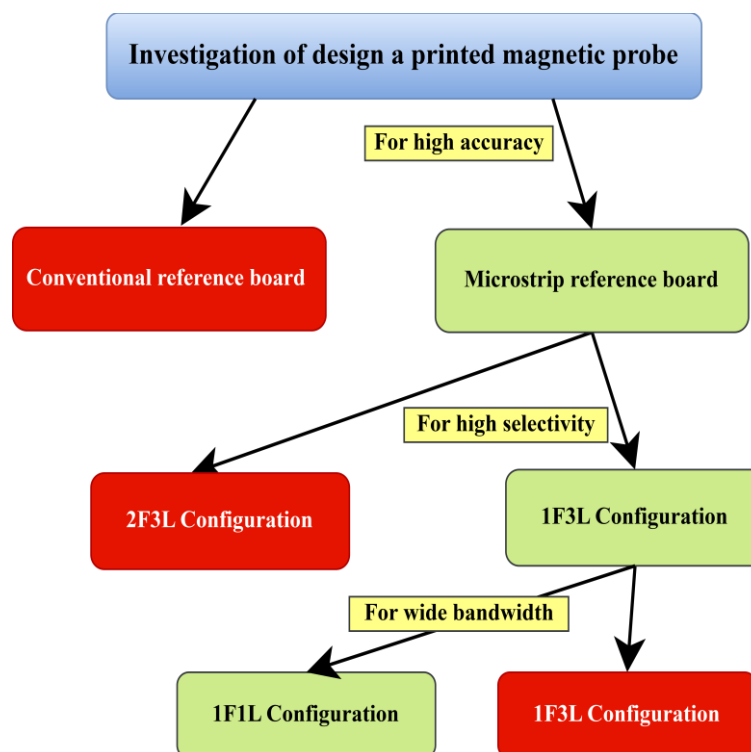


**Diagram 1.** The flowchart shows the optimum way to design the magnetic probe

The second part of the near field probe design is based on the result of the previous three investigations above by designing switchable broadband to tuneable narrowband printed magnetic probe structure with high sensitivity. This methodology starts with creating a simple loop gap resonator (LGR) of a small gap with a  $50\ \Omega$  transmission line. The designed resonator can be a reference probe for magnetic field estimation from 1 to 6 GHz. Moreover, it exhibits good sensitivity up to 3 GHz and is better than that of the frequency band 3 – 6 GHz sensitivity. A PIN diode was involved in the small gap and switched the resonance from broadband to a single band operating at 3.5 GHz to get high sensitivity for the band 3 – 6 GHz.

The switching from broadband to narrowband is achieved with a PIN diode by interchanging the dimensions of the LGR. Simultaneously, the Varactor diode is utilized to tune the narrowband resonance frequency across the band 3 – 6 GHz for the desired frequency like 3.5 GHz, 4.8 GHz, 5.2 GHz, and 5.8 GHz by increasing the parasitic capacitor of the resonator loop.

The separation between the E and H fields in the near field is achieved by loading two layers on top and bottom and connecting them through vias. These vias are arranged like a fence with an optimized distance between each other to suppress the electric field components and to enhance the isolation.

It is crucial to acknowledge that FR-4, the substrate that is widely utilized, possesses a relative permittivity of 4.3 and a loss tangent of 0.025 is suitable for designing the printed structures with a height of 1.6 mm. Its characteristics make it a reliable choice for such designs, ensuring optimal functionality and performance.



## 5 Main Result Achieved

This section presents the design, modelling, simulation, realization and test of the proposed five electromagnetic sensors : **Section 5.1** presents PBD antenna, **Section 5.2** demonstrates the PLPBDA antenna, the DSLPBDA antenna is depicted in **Section 5.3**, **Section 5.4** exhibits the broadband magnetic probe, and **Section 5.5** shows the design and modelling of switchable broadband to tuneable narrowband magnetic probe.

### 5.1 Design and Modelling of Printed Biconical Dipole Antenna with Tapered Balun for EMC Measurements

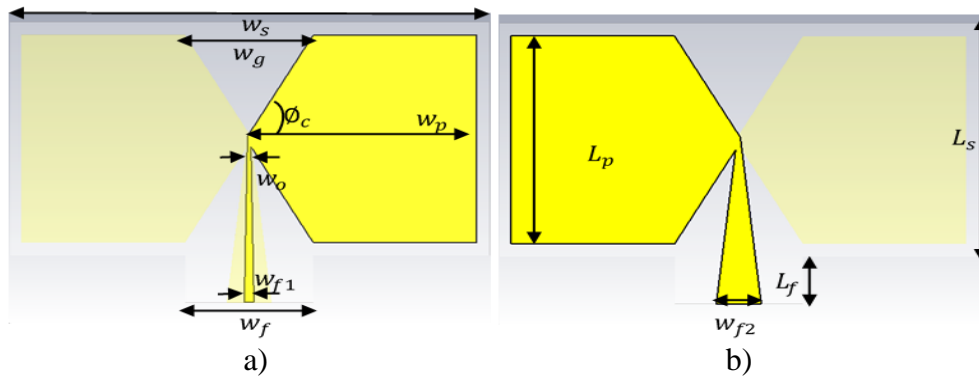
This work investigates the design, modeling, and fabrication of a small-size broadband printed biconical dipole (PBD) antenna to work as a reference antenna for EMC measurements. The printed biconical shape has been inspired by the projection of the classical biconical antenna to offer wide bandwidth from 0.65 GHz to 2.3 GHz. Moreover, suitable  $AF$  along the covering frequency reflects this design's accuracy and low uncertainty. This work is organized as follows; **Section 5.1.1**, **Section 5.1.2**, and **Section 5.1.3** present the antenna design, feeding method, and parametric study, respectively. The reflection coefficient is verified by modeling the structure's equivalent circuit in terms of lumped elements in **Section 5.1.4**. Additionally, the simulation and measurement results of the standard antenna parameters and the antenna factor are illustrated in **Section 5.1.5**. Finally, **Section 5.1.6** provides a brief comparison of the proposed structure and the commercial design offered for sale (BicoLOG 20300). The result of this section has been published in an impacted factor journal [A2].

#### 5.1.1 Printed biconical dipole antenna design

The proposed structure comprises two planner dipoles based on FR-4 substrate with relative permittivity of  $\epsilon_r = 4.3$  and loss tangent  $\tan \delta = 0.025$ , as illustrated in [9]. Furthermore, this dipole's shape and feeding lines have been modified to suit the EMC applications. The basic idea was inspired by the dipole characteristic and the fact that a thicker dipole would exhibit wider bandwidth. As a result, the thicker dipole was transformed into a planner to achieve this goal [8]. A virtual triangular slot with a width  $w_g$  was created between the two trapezoidal shapes placed at the top and bottom layers of the structure with  $(0.25 \lambda \text{ monopole})$  for each shape [44]. Thus,  $L = 0.25 \lambda = W_p = 71 \text{ mm}$ , the length  $L$  dimension was adjusted to shift the resonance frequency among the desired band. Figure 15 shows the geometrical shape of the proposed biconical antenna with the balun feeding method, while Table 1 lists the optimum dimensions of the antenna parameters.

**Table 1.** The overall parameters of the proposed antenna

Parameter	Value / mm	Parameter	Value / mm
$w_s$	150	$L_s$	90
$w_p$	71	$L_p$	80
$w_{f1}$	3	$w_{f2}$	14
$w_o$	1.5	$w_g$	40
$w_f$	40	$L_f$	18

**Figure 15.** The geometrical shape of the proposed biconical antenna, a) front view and b) back view

### 5.1.2 Feeding method

A balun can be defined as a transformer between the unbalanced port (antenna legs) and the balanced port (coaxial cable with  $50 \Omega$ ). It decreases the feeder radiation by controlling the flowing of currents and providing a balanced surface current at each antenna's legs. It prevents currents from propagation on the transmission line's outer surface to avoid distortion of the radiation properties [45]. The achieved wideband impedance matching with a balun feed line makes the structure suitable for EMC measurement applications that require wide bandwidth. Two cases are investigated here to determine the feeding line width with more stability and wider bandwidth.

Case–1: Both sides of transmission lines have the same width,

Case–2: The top and bottom sides of transmission lines have different widths.

The linear tapered balun feed method is dedicated to feeding this design [46]. Tapered transmission lines are printed on both sides of substrate layers with the same length and different widths. Moreover, the first end of the transmission line (port side) with a width of  $w_{f1} = 3 \text{ mm}$  is connected to a  $50 \Omega$  coaxial cable. While the other end of this transmission line (antenna side) with a width of  $w_o = 1.5 \text{ mm}$  is connected to the front face of the biconical antenna. On the other hand, the first end of the back transmission line (port side)

with a width of  $W_{f1} = 14$  mm is connected to a  $50 \Omega$  coaxial cable. While the other end of this transmission line (antenna side) also has a width of  $W_o = 1.5$  mm, and it is connected to the back face of the biconical antenna.

### 5.1.3 Parametric study

The proposed printed biconical antenna was modeled and simulated using CST Microwave Studio [21]. The parametric sweep feature in this software allowed us to sweep any parameter value to obtain the desired result. CST Microwave Studio uses Finite Integrated Method for its T-transient solver by discretizing the integral form of Maxwell's equations. Three parameters were swept as follows.

#### 5.1.3.1 The width of the virtual slot between two trapezoidal shapes $w_g$

This parameter presents the transition from the trapezoidal shape ( $w_g > 0$  mm) to the rectangular shape ( $w_g = 0$  mm). Since the  $w_p$  value is still constant, the parameter  $w_g$  is swept from 0 to 90 mm, and the corresponding S11 parameter is shown in Figure 16.

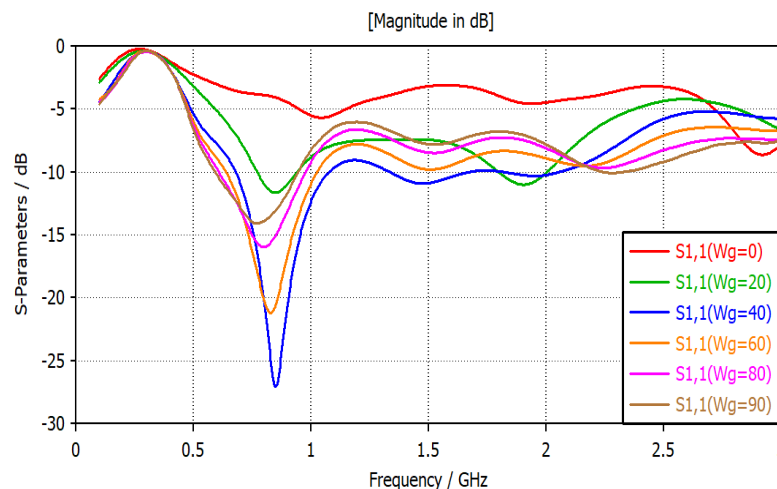


**Figure 16.** S11 parameter for different values of  $w_g$

It is clear that there is no matching at  $w_g = 0$  mm (rectangular shape), while the reflection coefficient offers  $S_{11} = -12$  dB at  $w_g = 20$  mm. The resonance frequency remained at the same point for different values of  $w_g$ , and the effect is only carried on the bandwidth. The best value of the  $w_g$  is 40 mm, which offers good value of reflection coefficient and broader bandwidth. The discontinuity of the trapezoidal shape increases the reactive part of the input impedance and causes high-standing wave ratio. Thus, minimizing the reactive part of the input impedance by increasing the cone angle would achieve wider impedance bandwidth [47].

### 5.1.3.2 Balun feeding method (straight line versus tapered line)

Two investigations are performed on the type of feeding line – Linear tapered lines and parallel lines. The reflection coefficient results of tapered and straight lines are presented in Figure 17. It is clear that the linear tapered feeding lines exhibit a  $-10$  dB impedance bandwidth wider than that of straight (parallel) lines, as indicated in the red curve.

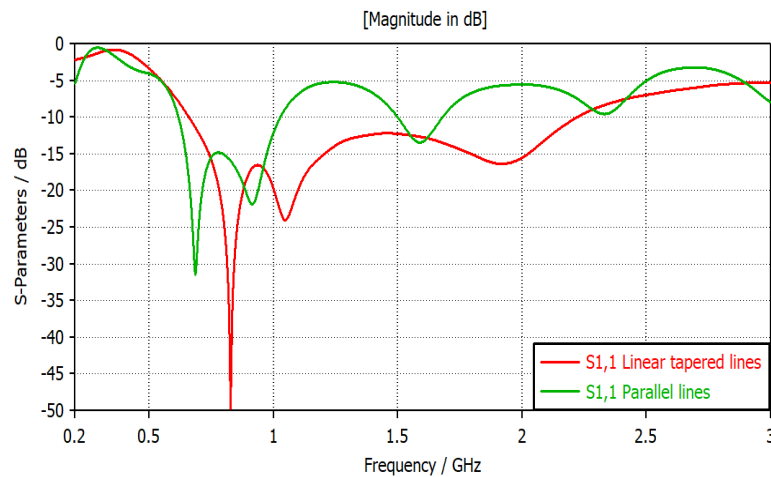


Figure 17. S<sub>11</sub>-parameter for both straight and tapered feeding lines

### 5.1.3.3 The separation gap between the trapezoidal shapes ( $d_o$ )

The gap distance  $d_o$  in mm between the two trapezoidal shapes significantly affects impedance bandwidth and the gain, as shown in Figure 18 a) & b), respectively. The green curve represents the optimum value of separation distance at  $d_o = 0$  mm, reflecting the maximum realized gain of 4 dBi and suitable impedance matching with broad bandwidth (0.7 – 2.3 GHz) [48].

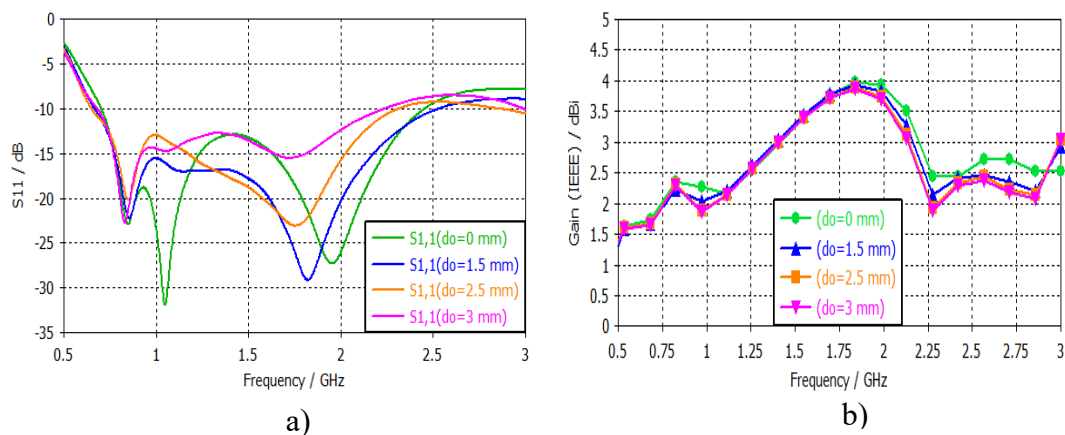
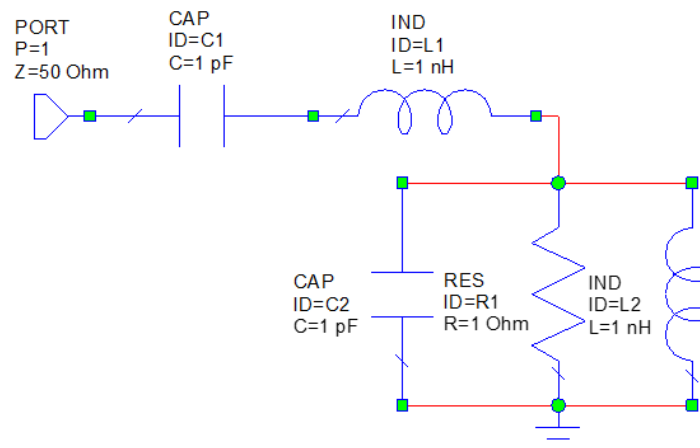


Figure 18. a) S<sub>11</sub> parameter for different values of  $d$  in mm and b) the realized gain for different values of  $d$  in mm

### 5.1.4 Equivalent circuit

Lumped-element equivalent circuits are employed in conjunction with 3D antenna simulations to analyze the impedance behaviour of the antennas under study. The biconical antenna is derived from the classical planar dipole, where the most common lumped elements model consists of series impedance ( $C_0$  and  $L_0$ ) and parallel resonator ( $C_1$ ,  $L_1$ , and  $R_1$ ) [49]. Figure 19 presents the equivalent circuit of the classical dipole, where the transmission line is modeled by the series impedance ( $C_0$  and  $L_0$ ) while the parallel resonator represents the two resonance arms. However, two extra parallel resonators are loaded to broaden the bandwidth to cover the frequency band from 0.7 to 2.3 GHz.



**Figure 19.** Equivalent circuit typical dipole antenna with default values of lumped elements

Figure 20 presents the circuit model for the broadband printed biconical dipole antenna in AWR Microwave Studio. The reflection coefficient of the suggested design was obtained from CST Microwave Studio and brought into AWR Microwave Studio. The optimization feature in AWR was then utilized to adjust the values of the lumped elements to match the imported reflection coefficient from CST. The S11 parameter results for the PBD antenna and its equivalent circuits in AWR are shown in Figure 21, while Table 2 lists the optimum values of the equivalent circuit-lumped elements.

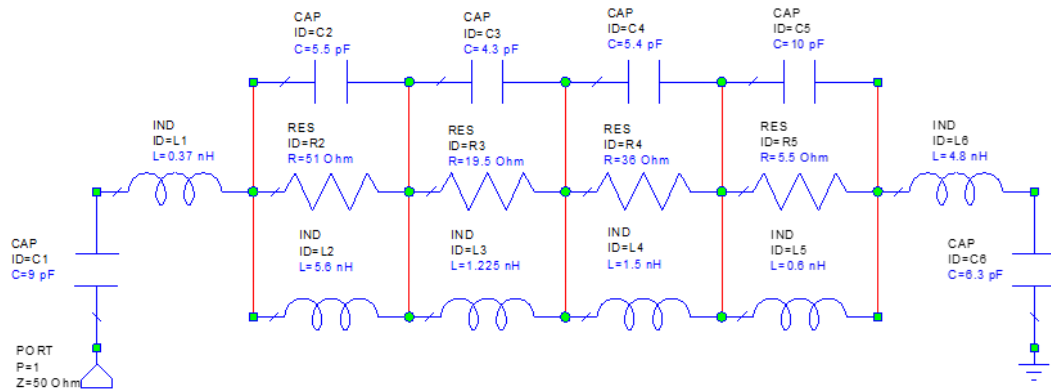


**Figure 20.** Equivalent circuit of the wideband printed biconical dipole antenna in AWR

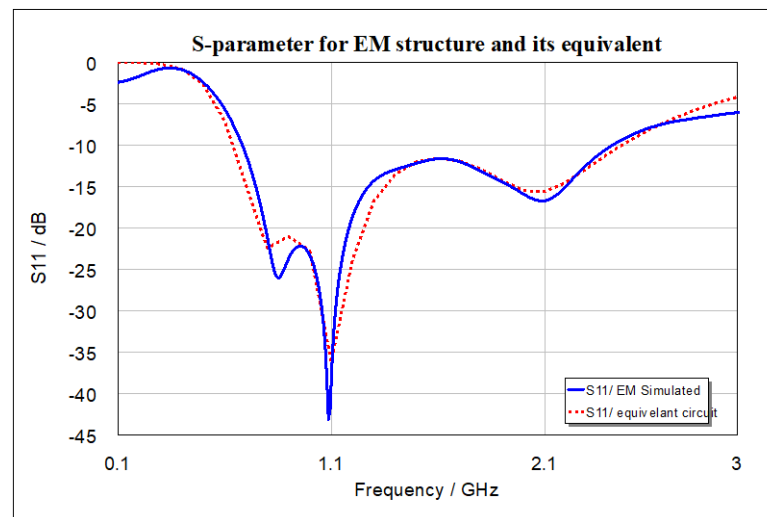


**Figure 21.** S11 parameter for wideband biconical dipole antenna and its equivalent circuit in AWR

**Table 2.** The optimum values of the lumped elements.

Element No.	1	2	3	4	5	6
R / $\Omega$	–	51	19.5	36	5.5	–
L / nH	0.37	5.6	1.22	1.5	0.6	4.8
C / pF	9	5.5	4.3	5.4	10	6.3

### 5.1.5 Fabrication process and measurement results

The CST Microwave Studio Software displays simulation results for standard antenna parameters that indicate whether the antenna is suitable for EMC measurements, except for the antenna factor. The antenna factor is a critical parameter in the design and can be calculated using the simulated realized gain using equation (2.4).

Figure 22 shows the prototype of the proposed design in both the front and back views. The proposed structure was fabricated using PCB technology with the help of CNC Machine. The spectrum analyzer (RIGOL DSA875) and the bi-directional coupler (RIGOL VB 1032) are utilized to measure the reflection coefficient, as presented in Figure 23. On the other hand, the radiation characteristics are measured using an anechoic chamber, a Microwave Signal Generator (MSG10), and a Microwave Signal analyzer (MSA10).

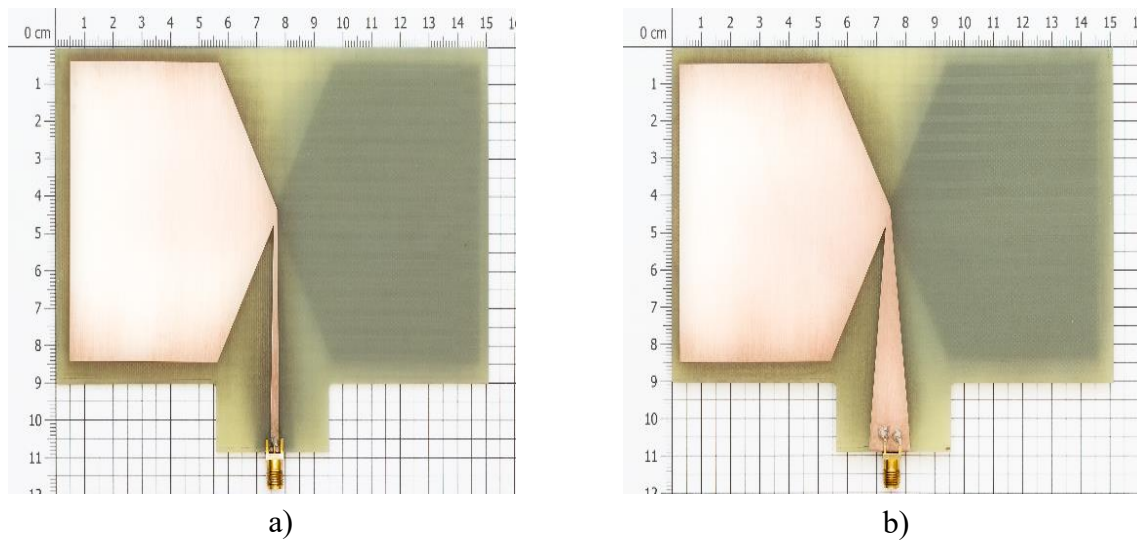


**Figure 22.** The prototype of the biconical dipole antenna: a) front view and b) back view

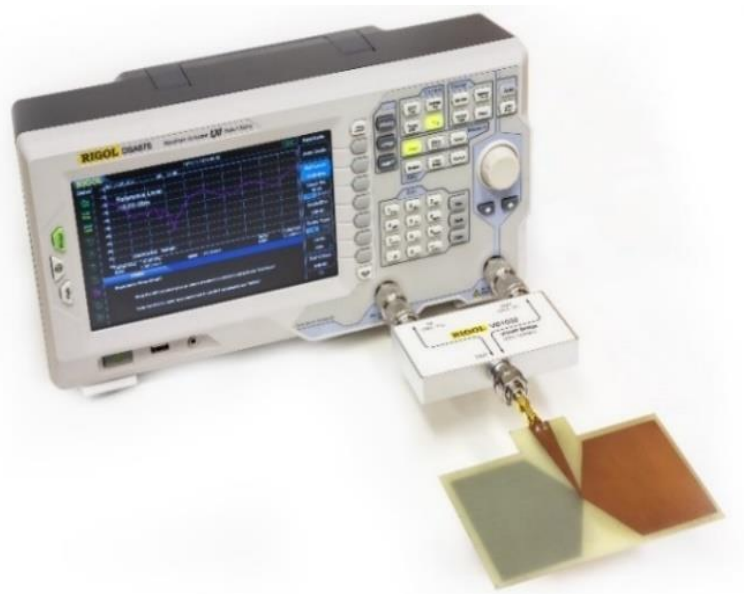


**Figure 23.** Measurement setup of S11 parameter using the spectrum analyzer



### 5.1.5.1 Reflection coefficient and VSWR

The reflection coefficients and VSWR are the same coin's two sides. Figure 24 a) shows simulated and measured reflection coefficients of the proposed antenna. It expresses about  $-30$  dB reflection coefficients at a resonance frequency of 1 GHz, with impedance bandwidth beginning from 750 MHz and ending at 2.5 GHz. The measured reflection coefficient (S11 parameter) is in good agreement with the simulated result, reflecting the Voltage standing wave ratio  $VSWR < 2$  in this broadband, as shown in Figure 24 b).

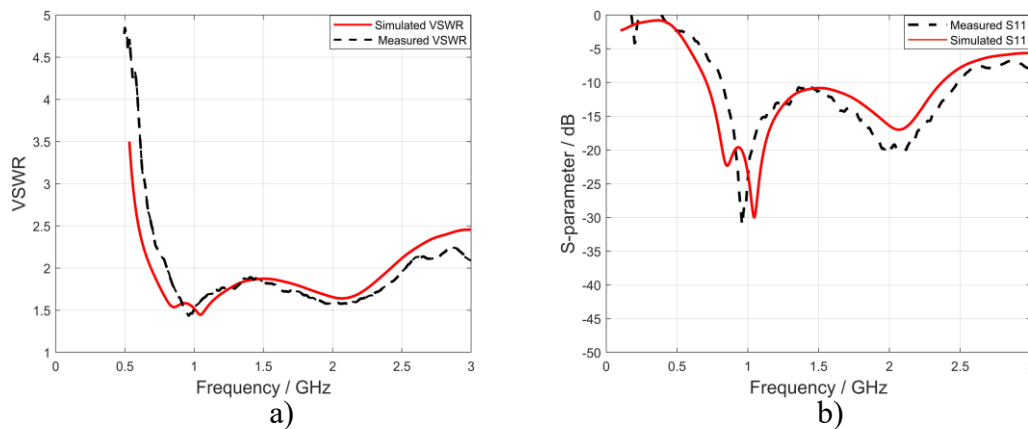


**Figure 24.** Simulated and measured results of a) S11 parameter and b) VSWR

### 5.1.5.2 Surface current distribution

Observing the distribution of the surface currents and following their behaviour is the best way to understand the physics behind the results. The results of surface current distribution at 1 GHz for the proposed structure in both the front and back view are shown in Figure 25. It shows the role of the tapered balun for balancing the current on both sides, as indicated in the red arrows, reflecting  $50 \Omega$  impedance matching between the antenna legs and the coaxial cable.

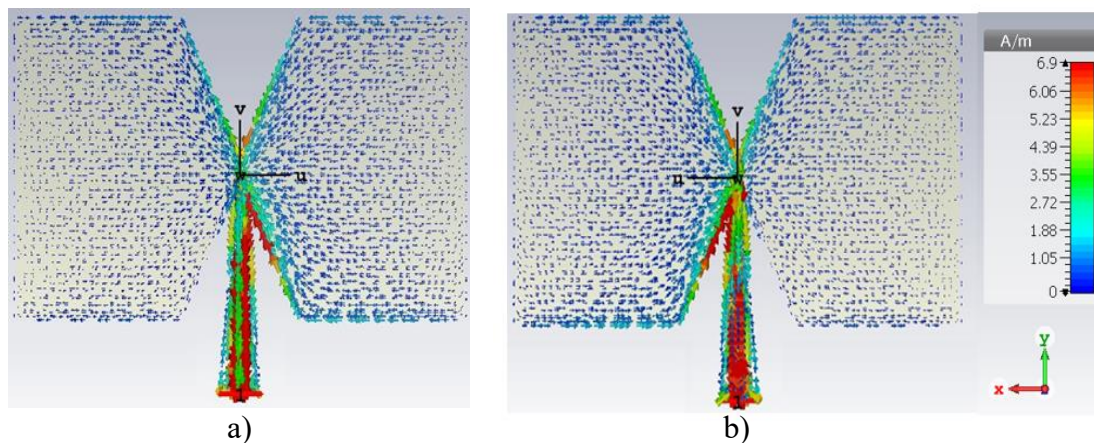


**Figure 25.** Surface currents distribution at 1 GHz: a) front view and b) back view



### 5.1.5.3 Realized gain and radiation efficiency

The antenna's realized gain value depends on its radiation pattern type. A directive radiation pattern offers high gain, while an omnidirectional pattern has relatively low gain, which is sufficient for EMC applications. Figure 26 a) demonstrates the simulated and measured results of the realized gain versus frequency. The comparison method is utilized to estimate the realized gain inside the anechoic chamber resulting in a maximum value of 3.8 dBi at 1.69 GHz with more than 85% simulated radiation efficiency, as demonstrated in Figure 26 b).

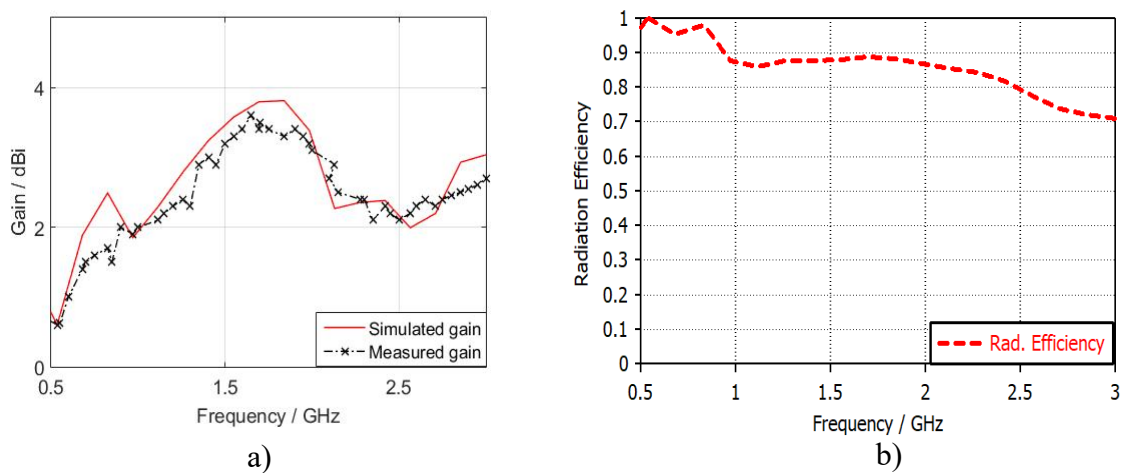
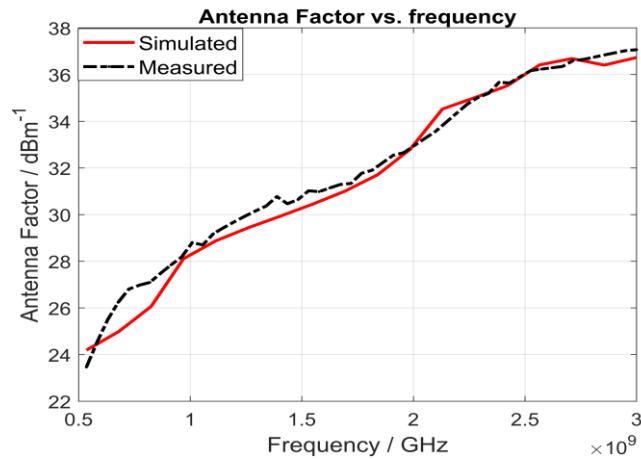


**Figure 26.** a) The simulated and measured gain in dBi and b) the simulated radiation efficiency

### 5.1.5.4 Antenna factor

The antenna factor is a crucial parameter in measuring how much this antenna is good to utilize as a reference antenna for EMC measurements. It equals the difference between the incident electrical field and the received voltage in dB [14, 50]. Equation (2.4) is used for calculating the antenna factor from the simulated and measured gain, respectively [51].

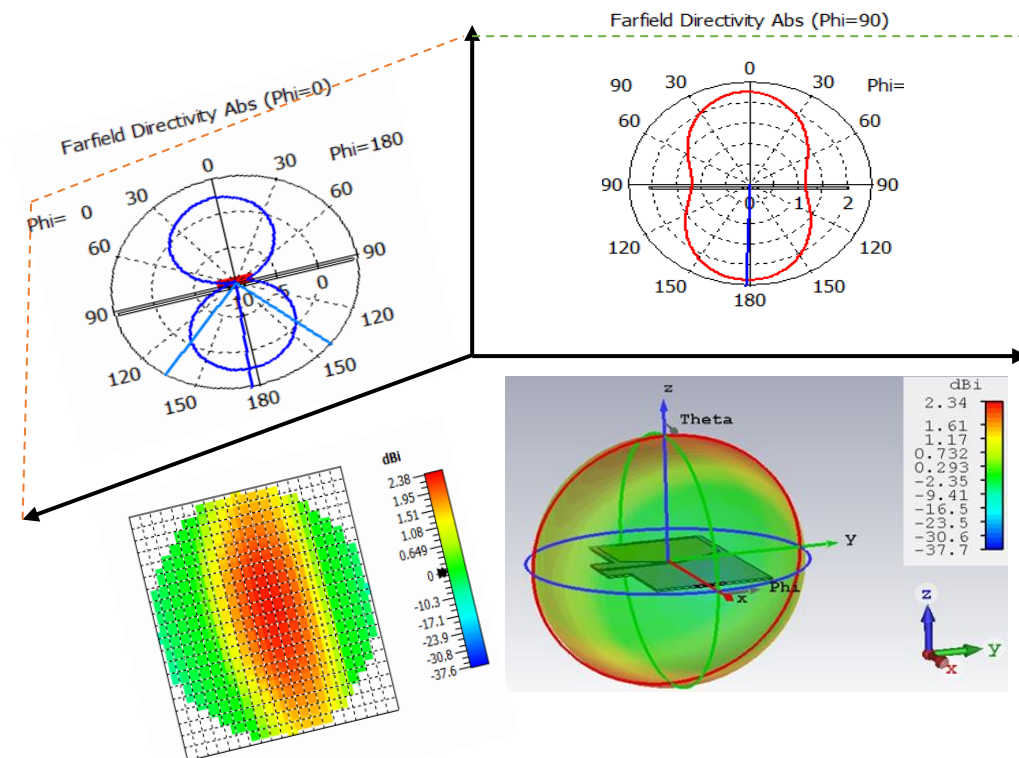
The calculated antenna factor for the proposed structure from the simulated and measured gain is depicted in Figure 27. The behaviour of the antenna factor is changing regarding the impedance matching. In particular, the antenna factor regularly increases at a well-matched band above 650 MHz, reaching up to 2.5 GHz. In contrast, it grows in non-regular steps above 2.5 GHz due to the miss match and the fact that the radiation pattern shape is changing toward directive rather than omnidirectional above 2.5 GHz.



**Figure 27.** Antenna factor in  $\text{dBm}^{-1}$  vs. frequency for printed biconical dipole antenna

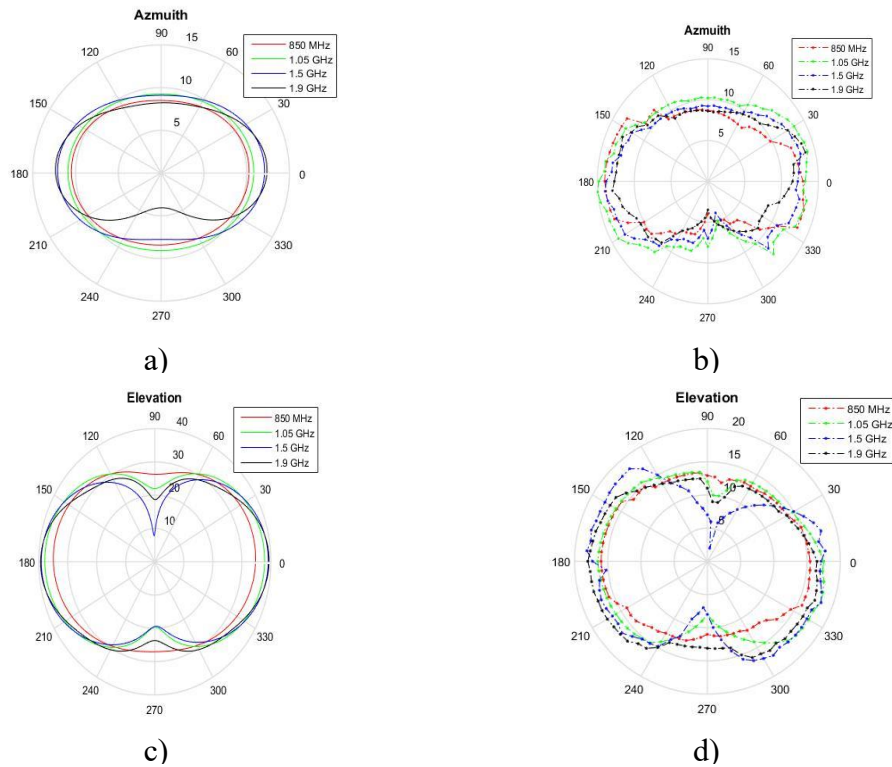
### 5.1.5.5 Radiation pattern

Figure 28 shows the 3-D radiation pattern of the proposed antenna. It can be seen that the azimuth line or longitude line can be obtained with  $ph = 90^\circ$  (the red line), where this line is almost equal in value along its radius. Furthermore, the elevation line or latitude line will be achieved at  $ph = 0^\circ$  [51]. The projection of the radiation pattern on a surface shows an elliptical shape which reflects the relation between the E and H fields for this design.



**Figure 28.** The simulated radiation pattern of the printed biconical dipole antenna

The simulated and measured results for both planes (azimuth and elevation) for different frequency bands are presented in Figure 29. The omnidirectional behaviour clearly appeared at lower frequencies. On the other hand, the radiation pattern is directive rather than omnidirectional at high frequencies, which explains the high directive gain above 2.5 GHz in Figure 24 a). Figure 30 presents the radiation measurement setup inside the anechoic chamber.



**Figure 29.** Simulated and measured radiation pattern: a) simulated azimuth, b) measured azimuth, c) simulated elevation and d) measured elevation.

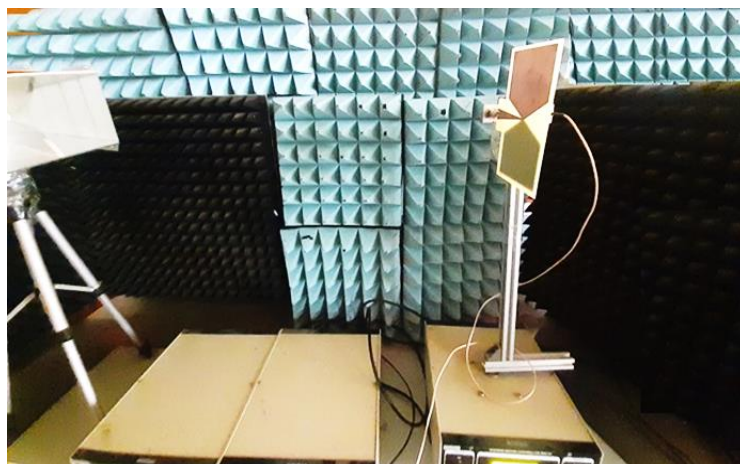




**Figure 30.** Radiation pattern measurements setup inside the anechoic chamber

### 5.1.6 Comparison between the proposed design and the commercial one

Table 3 briefly compares the specifications of the proposed PBD antenna and the (BicoLOG 20300) offered for sale. The specifications of the (BicoLOG 20300) are taken from the datasheet posted on the website [52]. Both structures are based on the biconical shape that reflects an omnidirectional radiation pattern. The proposed design has a compact size with a low profile and is lightweight compared with the classical one due to the advantage of using PCB technology. This technique has the disadvantage of small bandwidth (650 MHz – 2.3 GHz) compared to the classical antenna (20 MHz – 3 GHz). In contrast, the planar bi-conical antenna offers an acceptable realized gain of a maximum value of 3.8 dBi, while the classical antenna's maximum gain is 1 dBi. Finally, both designs have good antenna factor values, making them suitable for use as reference antennas inside the EMC chamber.

Table 3. Design specifications of the PBD antenna and commercial antenna (BicoLOG 20300)

Specifications	BicoLOG 20300	Proposed Design
Dimensions / mm	350 × 160 × 140	150 × 90 × 1.6
Design	Biconical	Printed biconical
Substrate	–	FR-4
Weight / g	350	50
Gain / dBi	–45 – 1	2 – 3.8
Frequency range / MHz	20 – 3000	650 – 2300
Antenna Factor* <sup>1</sup> ) / dBm <sup>-1</sup>	22 – 44	24 – 36
RF Connector	SMA Female	SMA Female
Picture		

\*<sup>1</sup>) frequency range from 0.6 to 2.3 GHz.

The achieved antenna factor values for the proposed design are in line with commercial antenna design values BicoLOG 20300, as illustrated in Table 4.

Table 4. Numerical antenna factor comparison of the proposed antenna with the commercial antenna (BicoLOG 20300)

F / GHz	0.5	1	1.5	2	2.5
AF (BicoLOG 20300) / dBm <sup>-1</sup>	22	28	29	39	42
AF (Proposed Design) / dBm <sup>-1</sup>	24	28	30	33	36

## 5.2 Design a Broadband Printed Log-Periodic Biconical Dipole Array Antenna

The proposed printed biconical (PBD) antenna design in **Section 5.1** exhibited convenient specifications for the EMC measurements regarding size reduction and bandwidth enhancements. However, it has an omnidirectional radiation pattern, making it suitable for different EMC tests, like fast evaluation of the background noise in the OATS and radiated emission test. In the radiated emission test, the radiation pattern of the reference antenna must cover the DUT to obtain the maximum field strength. Therefore, this test needs a high-gain reference antenna with a sufficient beamwidth angle. The proposed PBD antenna will be the basic unit for the next design by utilizing its advantages of small size and wide bandwidth.

This work presents the design, modeling, and fabrication of a printed log-periodic biconical dipole array (PLPBDA) antenna for EMC measurements. The proposed structure has replaced the traditional dipoles with bow tie-shaped dipoles to tackle both goals: size reduction and bandwidth enhancement. The content of this work is broken down into the following sections: **Section 5.2.1** compares the traditional and bow tie-shaped dipoles. The mathematical analysis for the LPDA antenna is described in **Section 5.2.2**. **Section 5.2.3** discusses the feeding method for the PLPBDA antenna and its effect on the other parameters like bandwidth, gain, ... etc. The simulated and measured results are presented and discussed in **Section 5.2.4**. Finally, brief comparisons between the proposed structure, the literature reviewed, and the commercial antenna offered for sale (HyperLOG 7060) are listed in **Section 5.2.5** and **Section 5.2.6**. The results of this section have been published in EI conference [A4], AE conference [A5] and impacted factor journal [A6].

### 5.2.1 Comparative analysis of conventional and bow tie-shaped dipoles

This section focuses on the benefits of using a biconical dipole instead of a classical one. The benefits of size reduction and bandwidth enhancement have been demonstrated by designing and simulating two dipoles – conventional dipole and biconical dipole – using CST Microwave studio with a discrete feeding port. Figure 31 presents the geometrical shape of these structures, while Table 5 illustrates the optimal dimensions.

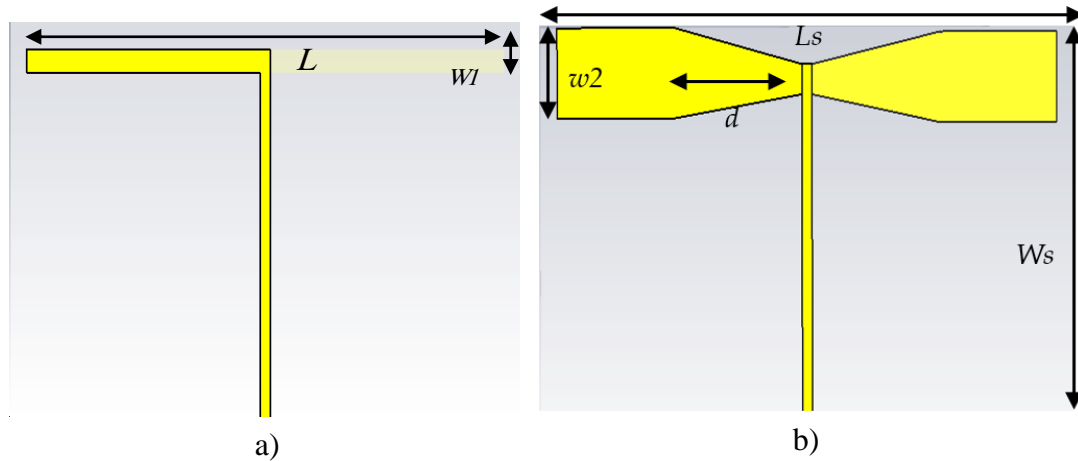


**Figure 31.** Two dipoles are modeled in CST Microwave Studio: a) conventional dipole and b) biconical dipole

**Table 5.** Lists the dimensions for the conventional and proposed dipole antenna

Parameter	$L$	$W1$	$W2$	$Ls$	$Ws$
Value / mm	170	6	16	180	160

The reflection coefficient versus frequency for both structures is shown in Figure 32. The biconical dipole requires a length less than a conventional dipole to achieve the same resonance frequency. Moreover, the proposed dipole offers wider bandwidth than the traditional one, as is evident in the biconical dipole impedance curve in Figure 33, which is flatter with frequency than the conventional dipole curve.

The role of parameter  $d$  in tuning the impedance bandwidth of the proposed dipole is shown in Figure 34. Increasing the value of  $d$  in mm will shift the resonance frequency toward lower bands with a narrower bandwidth. The impact of parameter  $d$  in controlling both frequency location and the impedance bandwidth is a valuable feature in designing a PLPDA antenna. The achieved wide impedance bandwidth of the biconical dipole is attributed to the closing starting points of the electromagnetic waves, which are controlled by parameter  $d$ .

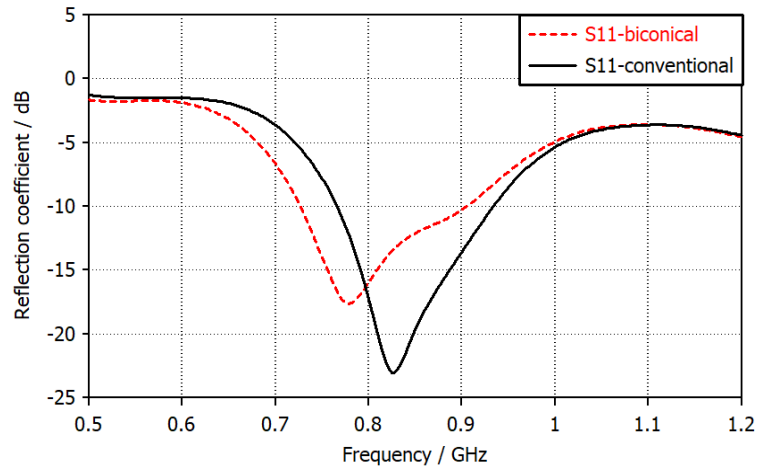


**Figure 32.** Reflection coefficient for conventional and biconical dipole

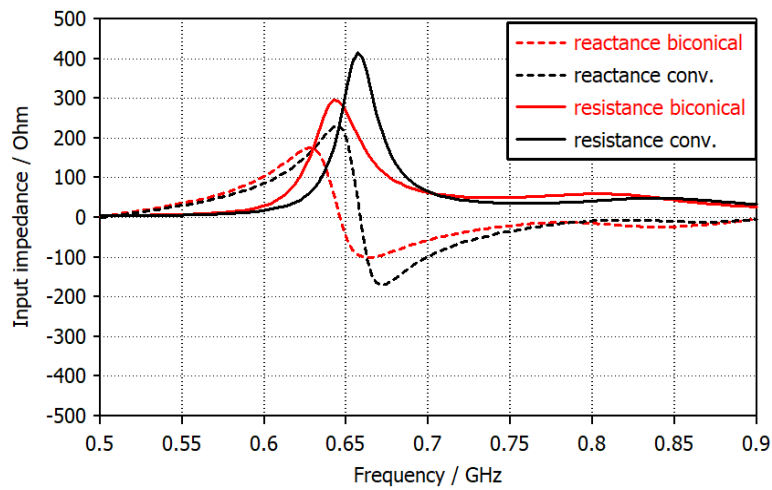


**Figure 33.** Input impedance versus frequency for conventional dipole and biconical dipole

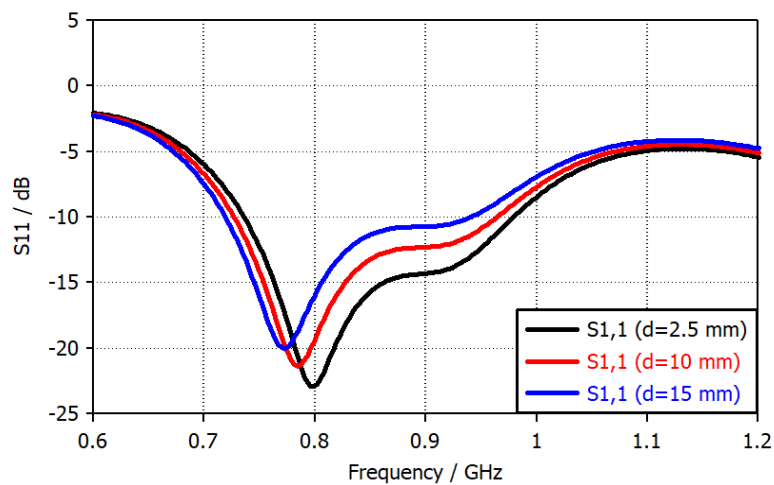


**Figure 34.** S11 parameter for different values of  $d$  in mm

### 5.2.2 Printed log-periodic biconical dipole array antenna design

The classical log-periodic dipole array (LPDA) antenna was deduced firstly from the classical dipole (radiate at  $\lambda/2$ ) by Isbell [53]. The LPDA antenna consists of several dipoles arranged in a logarithmic style with  $\lambda/2$  length for each dipole. The energy will start flowing from the 50  $\Omega$  point at the narrower tip toward the wider end. At any specific frequency, only one dipole radiates at its wavelength. The dipoles with lengths smaller than the wavelength act as directive dipoles, whereas they would act as reflectors if their lengths are larger than the wavelength [54]. The straightforward procedures for designing the classical LPDA antenna were described by Carrel [55] as follows.

According to the desired directivity or gain, the scaling factor  $\tau$  and the spacing factor  $\sigma$  can be computed from the point intersection of the line  $\sigma = 0.243\tau - 0.051$  in the carrel diagram.

Based on the achieved parameters from the carrel diagram ( $\tau$  and  $\sigma$ ), equations (5.1), (5.2), and (5.3) are used to evaluate the maximum number of dipoles (integer number).

$$N = 1 + \frac{\log B_S}{\log \frac{1}{\tau}}, \quad (5.1)$$

$$B_S = B \cdot B_{ar} = \frac{f_{upper}}{f_{lower}} \times B_{ar}, \quad (5.2)$$

$$B_{ar} = 1.1 + 7.7(1 - \tau)^2 \frac{4\sigma}{1 - \tau}, \quad (5.3)$$

where  $B_S$  and  $B_{ar}$  present the structure bandwidth and the active region bandwidth, respectively.

The length of the first dipole (the most extended one) that matches the lower frequency ( $f_{lower}$ ) can be calculated using equation (5.4).

$$L_1 = \frac{1}{2} \times \frac{3 \times 10^8}{f_{lower}}. \quad (5.4)$$

The distance between each successive dipole ( $R_1 - R_2$ ) can be found from equation (5.5).

$$R_1 - R_2 = \frac{L_1 - L_2}{2} \times \frac{4\sigma}{1 - \tau}. \quad (5.5)$$

Equations (5.6) and (5.7) are utilized to evaluate the dipoles' width  $W_n$ .

$$Z_0 = \frac{377}{\pi} \left( \ln \left( \frac{L_n}{a_n} \right) - 2.25 \right), \quad (5.6)$$

$$W_n = \pi \times a_n, \quad (5.7)$$



The length  $L_n$ , distance  $W_n$  and width of successive dipoles  $R_n$  can be computed from equations (5.8), (5.9) and (5.10), respectively.

$$L_{n+1} = \tau \times L_n, \quad (5.8)$$

$$R_{n+1} = \tau \times R_n, \quad (5.9)$$

$$W_{n+1} = \tau \times w_n, \quad (5.10)$$

The calculated results of the length, distance, and spacing between dipoles should be scaled by the square root of the effective dielectric constant  $\frac{L_n}{\sqrt{\epsilon_{eff}}}$ ,  $\frac{W_n}{\sqrt{\epsilon_{eff}}}$  and  $\frac{R_n}{\sqrt{\epsilon_{eff}}}$  respectively [32]. The effective dielectric constant is described by equation (5.11).

$$\epsilon_{eff} = \frac{\epsilon_r + 1}{2} + \frac{\epsilon_r - 1}{2} \left[ 1 + 12 \frac{h}{w} \right]^{-\frac{1}{2}}. \quad (5.11)$$

Moderate bandwidth and large size were the main issues in the PLPDA antenna design to work as a reference antenna for the EMC measurements. In particular, the reference antenna inside the EMC chamber requires wide bandwidth to cover the EMI with the communication bands spreading in the spectrum. On the other hand, size is an essential factor in the shorter measurement distance ( $d_m$ ) and test configuration issues.

The proposed PLPBDA antenna utilized biconical dipoles instead of the classical dipole elements to mitigate the size and bandwidth issues since the biconical dipole offered wide bandwidth and a smaller size than the classical dipole [9]. Therefore, the proposed PLPBDA antenna has achieved size reduction and bandwidth enhancement goals. Figure 35 presents the geometrical shapes for the conventional and proposed PLPBDA antenna.

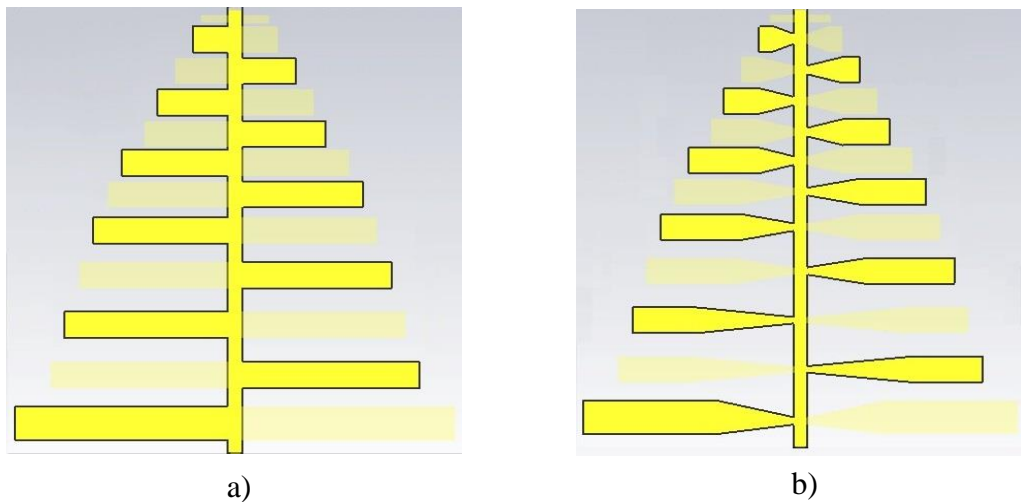


**Figure 35.** The geometrical structure of 11 elements of a) conventional design and b) proposed PLPBDA design

The spacing between the adjacency dipoles becomes smaller as it approaches the high-frequency dipoles. In contrast, low frequencies at the longest dipoles have higher bandwidth than the lowest length dipoles, which have sharp bands. Therefore, the spacing should be getting small to make these narrower bands close to each other, leading to achieving a wide band. Figure 36 presents the simulated S11 parameter versus frequency for the conventional and the proposed structure. The effect of using biconical dipoles appears clearly by noticing the achieved impedance bandwidth (0.5 – 5.5 GHz) compared with that of linear dipoles (0.7 – 3.3 GHz).

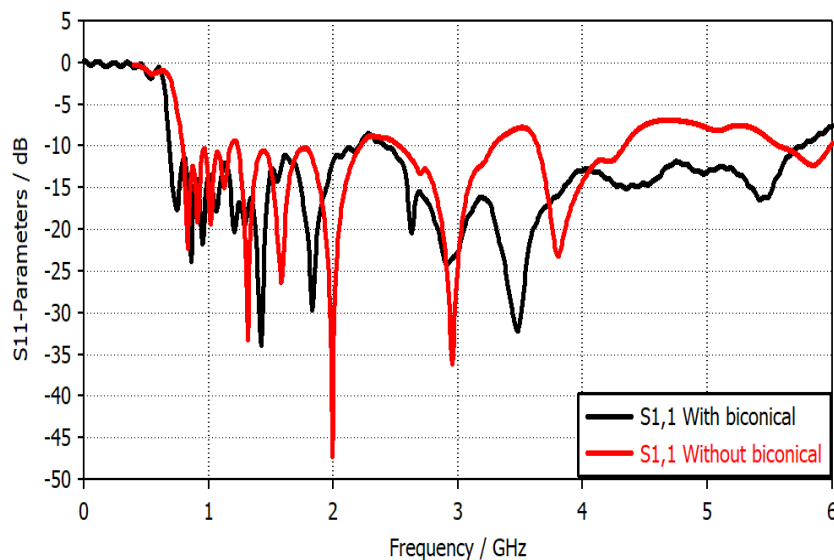


**Figure 36.** S11 parameter with/without biconical structure

The proposed structure has better performances than the conventional one since it exhibited wider impedance matching. The voltage standing wave ratio (VSWR) simulated result is still above 2, particularly at 2.4 GHz (about  $-9$  dB reflection coefficient). An additional dipole (classical one) has been designed and optimized to enhance the reflection coefficient value at 2.4 GHz. This extra dipole was inserted between the  $50 \Omega$  input port and biconical dipole number 11. The reflection coefficient results with and without an additional dipole are presented in Figure 37. It is obvious that using an extra dipole has enhanced the reflection coefficient in the band from 0.5 GHz to 6 GHz with  $VSWR < 2$  (the reflection coefficient value is less than  $-10$  dB).

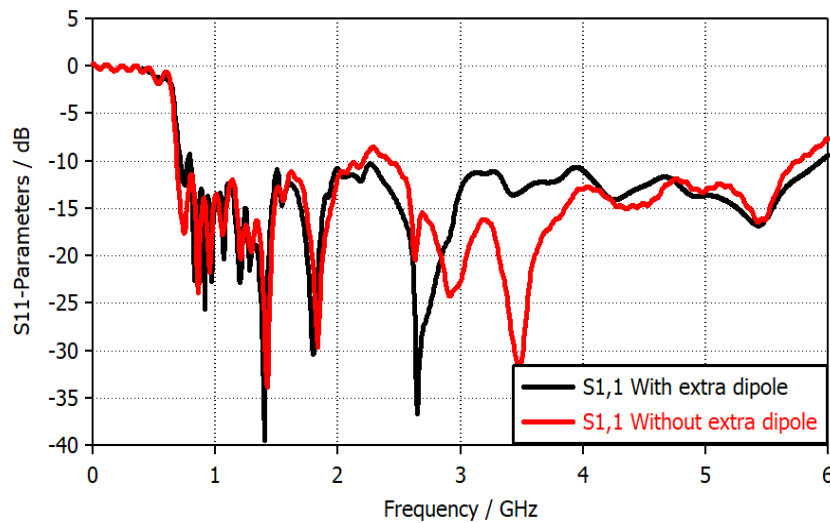


**Figure 37.** S11 parameter with/without extra dipole

It is worth mentioning that there was another advantage of adding the additional dipole besides the reflection coefficient improvement. The antenna's gain has been significantly affected by changing the length of the extra additive dipole, as shown in Figure 38. The lowest gain fluctuations are obtained with the dipole length  $L_{12} = 10$  mm, which is mandatory to achieve a good antenna factor result with low uncertainty. However, there is a trade-off between the antenna gain and the impedance matching. For instance, increasing the additive dipole length will achieve a flatter gain curve while offering undesirable impedance matching. The optimum value of the additive dipole length is  $L_{12} = 10$  mm, which provides compromise results for both the S11 parameter and the antenna gain.

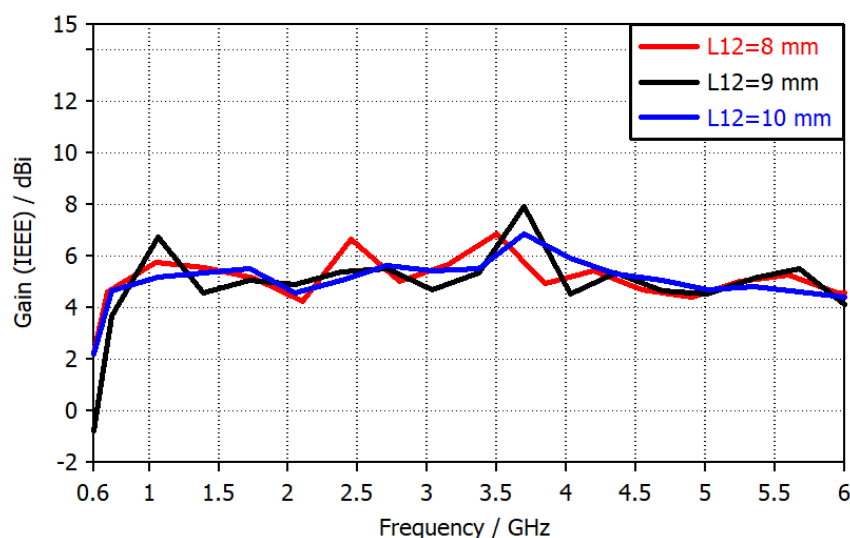


**Figure 38.** The simulated gain with different lengths of an extra dipole

Figure 39 shows the optimized geometrical shape of the proposed PLBPDA antenna, while Table 6 lists the dimensions of each dipole element. The width of all dipoles  $W$  is set to be 10 mm except for the first dipole ( $W_1 = 13$  mm) and the extra dipole ( $W_{12} = 5$  mm). In contrast, parameter  $d$  plays a vital role in having a broadband impedance bandwidth since it is crucial in modifying every dipole's biconical shape, as presented previously in Figure 34. Finally, an optimization process has been performed on the antenna parameters to achieve better performances using Microwave CST Studio's facilities [21]. The utilized substrate is epoxy FR-4 with a relative permittivity  $\epsilon_r = 4.3$ , and loss tangent of  $\tan\delta = 0.025$ .

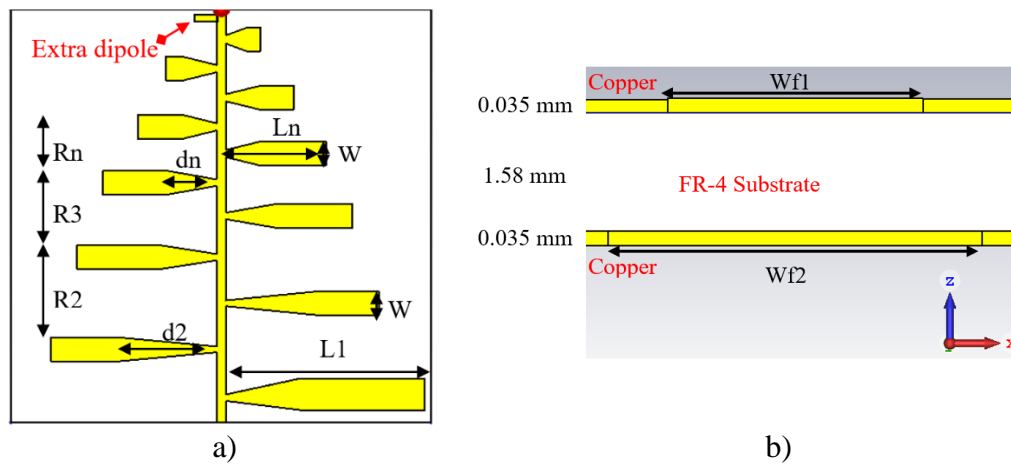


**Figure 39.** The optimized geometrical shape of the proposed antenna: a) front view and b) side view

**Table 6.** Illustration of optimum values of the parameters

No.	1	2	3	4	5	6	7	8	9	10	11	12
L / mm	77.5	65	60	55	50	45	40	31.8	27.5	21.2	15	10
W / mm	13	10	10	10	10	10	10	10	10	10	10	5
R / mm	20	19	19	17	13.7	12	12	12	12	12	12	-
d / mm	20	30	27.5	13.75	11.25	11.25	11.25	5	5	5	5	-

### 5.2.3 Feeding techniques

The right choice of feeding method for LPDA antenna reflects better behaviour in both frequency and radiation characteristics. The conventional feeding method comprises two non-radiated lines connecting the consecutive dipoles attached to both sides of the substrate. There is a  $180^\circ$  phase shift between every two successive dipoles, guaranteeing the energy radiates from the exciting dipole and preventing energy radiation from the next dipole by coupling since it has a reverse direction and hence increases the radiation efficiency. The width of each microstrip feeding line  $w_f$  can be computed using equation (5.12) [9].

$$z_0 = \frac{87}{\sqrt{\epsilon_r + 1.41}} \ln\left(\frac{5.98 \times h}{0.8 \times w_f}\right). \quad (5.12)$$

where  $h$  is the height of the substrate, and  $z_0$  represents the characteristic impedance  $50 \Omega$ . This work has utilized a balanced feeding method which consists of two microstrip lines with different widths to create a balun and balance the surface current on both sides. The optimized value of the top microstrip line width is  $w_{f1} = 3.5$  mm, while the bottom microstrip line has a width of  $w_{f2} = 5$  mm. A parametric sweep has been performed using CST Microwave Studio to achieve the optimum values reflecting  $-10$  dB impedance matching with all array elements and covering the band from 0.5 GHz to 6 GHz.

#### 5.2.4 Simulation and measurement results

Figure 40 shows the prototype of the fabricated design. The proposed structure has been manufactured and measured in the EMC laboratory at the University of West Bohemia, Faculty of Electrical Engineering. Moreover, CNC machine type LPKF ProtoMat S100 CNC is utilized for this fabrication based on an epoxy FR-4 substrate.

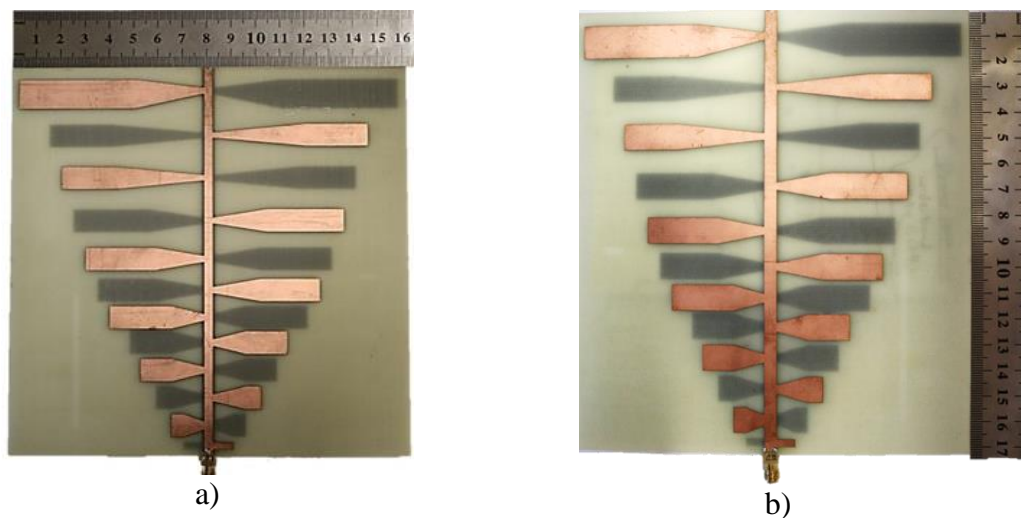


**Figure 40.** The prototype of the proposed design: a) front view and b) back view

##### 5.2.4.1 Reflection coefficient

The frequency characteristics of the proposed design have been demonstrated by measuring the reflection coefficient ( $S_{11}$  parameter) with the help of The RIGOL DSA875 spectrum analyzer and directional couplers (RIGOL VB 1032 and RIGOL VB 2032). However, the operation bandwidths of the directional couplers completed each other to cover the band from 1 MHz up to 8 GHz (RIGOL VB 1032: 0.01 – 3.2 GHz) and RIGOL VB 2032: 2 – 8 GHz). Figure 41 a) shows the simulated and measured  $S_{11}$  parameter versus

frequency, while the measurement setup of the reflection coefficient is depicted in Figure 41 b). It can be seen that this design offers a wide impedance bandwidth of 0.55 – 6 GHz in both simulation and measurement results.

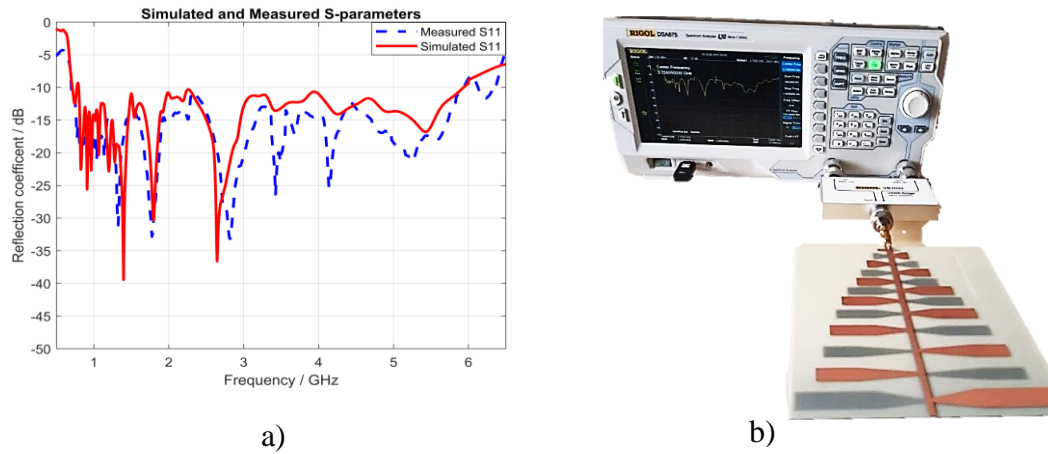


**Figure 41.** a) simulated and measured reflection coefficient and b) the measurement setup of the reflection coefficient

#### 5.2.4.2 Surface current distribution

To have a deep sight into the structure's behavior, the surface currents distribution of this structure is demonstrated and studied. The simulation results of the surface current at various frequency bands can be obtained using CST Microwave Studio, as shown in Figure 42. The active region's transition from the most extended dipoles toward the smaller dipoles coincides with the resonance frequency transition. Moreover, this smooth and continuous transition will reflect the achieved high gain and stability in the radiation pattern.

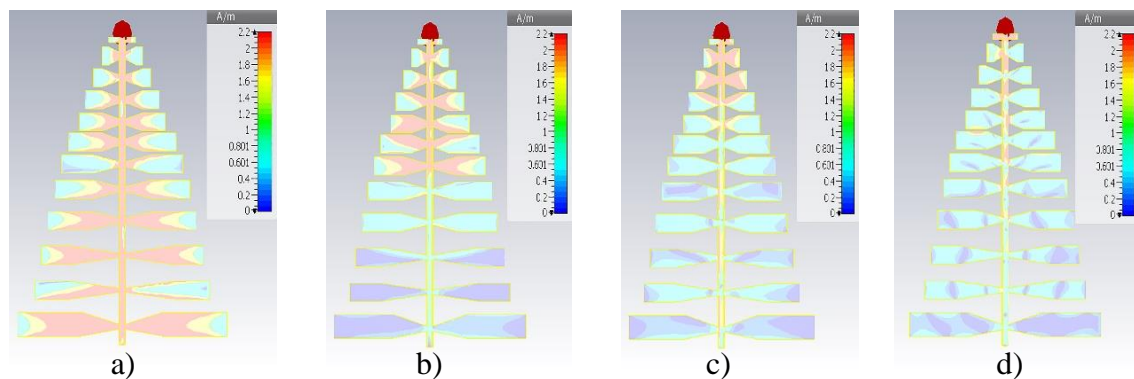


**Figure 42.** Surface current distribution at a) 0.7 GHz, b) 1.2 GHz, c) 2.2 GHz, and d) 4.5GHz

### 5.2.4.3 Radiation pattern

Figure 43 presents the simulated radiation pattern components of the proposed structure. The projection of the radiation pattern on a surface has created an elliptical shape that reflects the relation between the E and H fields. Moreover, the presented radiation pattern can cover the DUT making this antenna a good candidate as a reference antenna for the EMC radiated measurements.

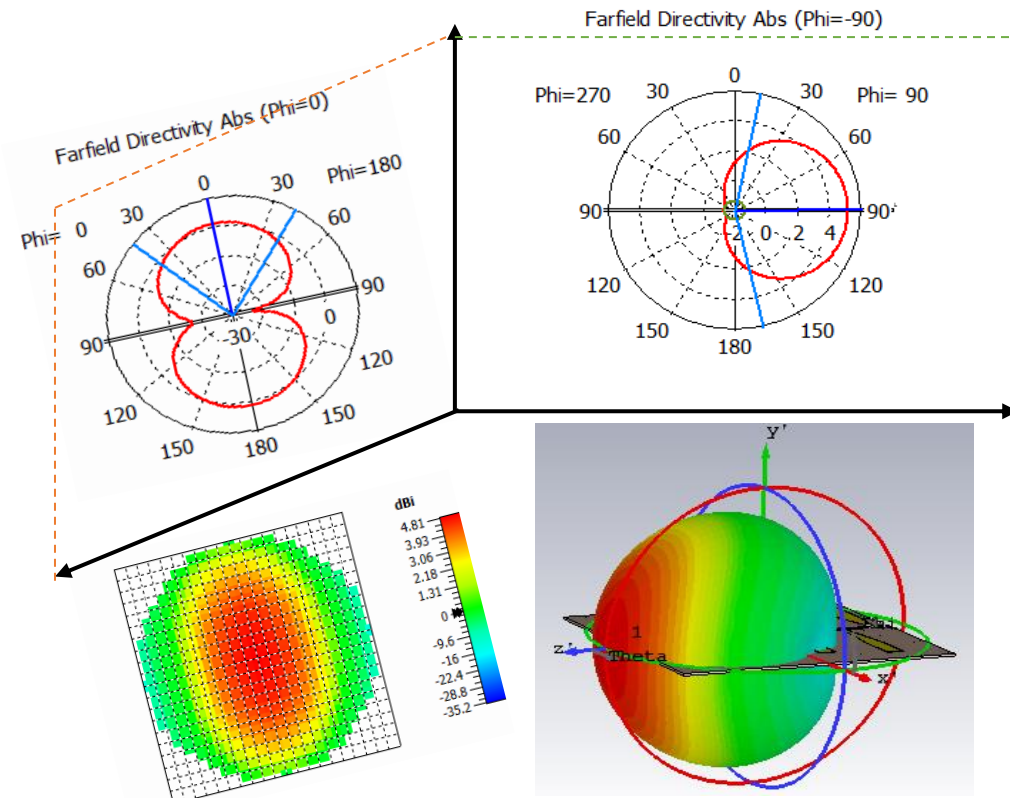


**Figure 43.** The simulated radiation pattern of the PLPBDA antenna

Radiation pattern and gain measurements were performed inside the University of West Bohemia EMC chamber, as shown in Figure 44. The measured results of the E-plane and H-plane have been evaluated by rotating the designed antenna around its axle  $360^\circ$  in vertical and horizontal directions, respectively. Figure 45 and Figure 46 present the simulated and measured radiation pattern results in both the E-plane and H-plane, which have the main lobe at  $90^\circ$ . The measured radiation patterns in both planes agree with the CST Microwave studio's simulated results. Moreover, the H-plane has a high back lobe at low frequencies and diminishes its value gradually with high frequencies.



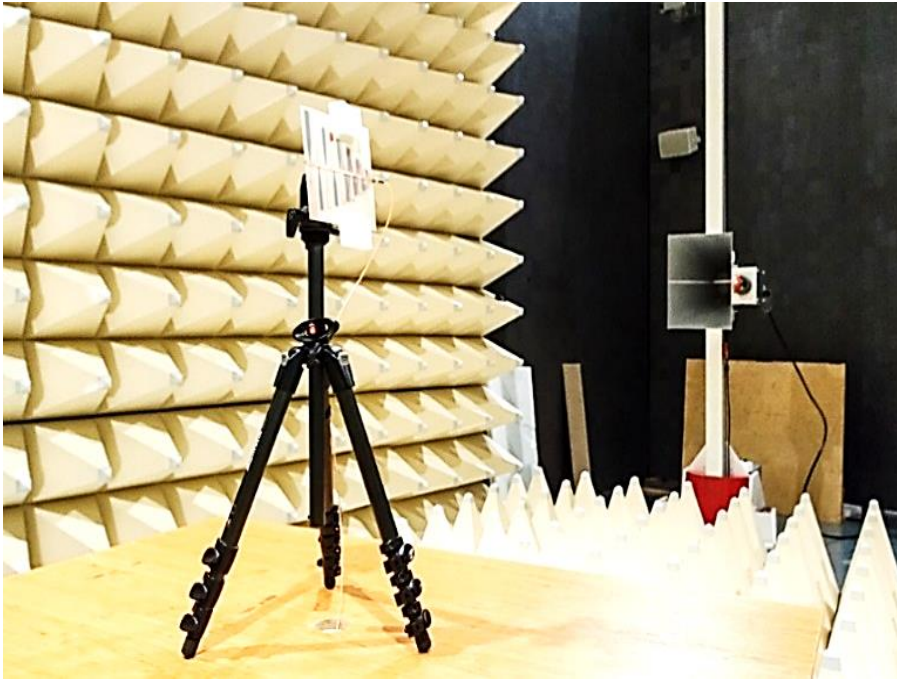


**Figure 44.** Radiation pattern setup for the proposed antenna inside the EMC chamber

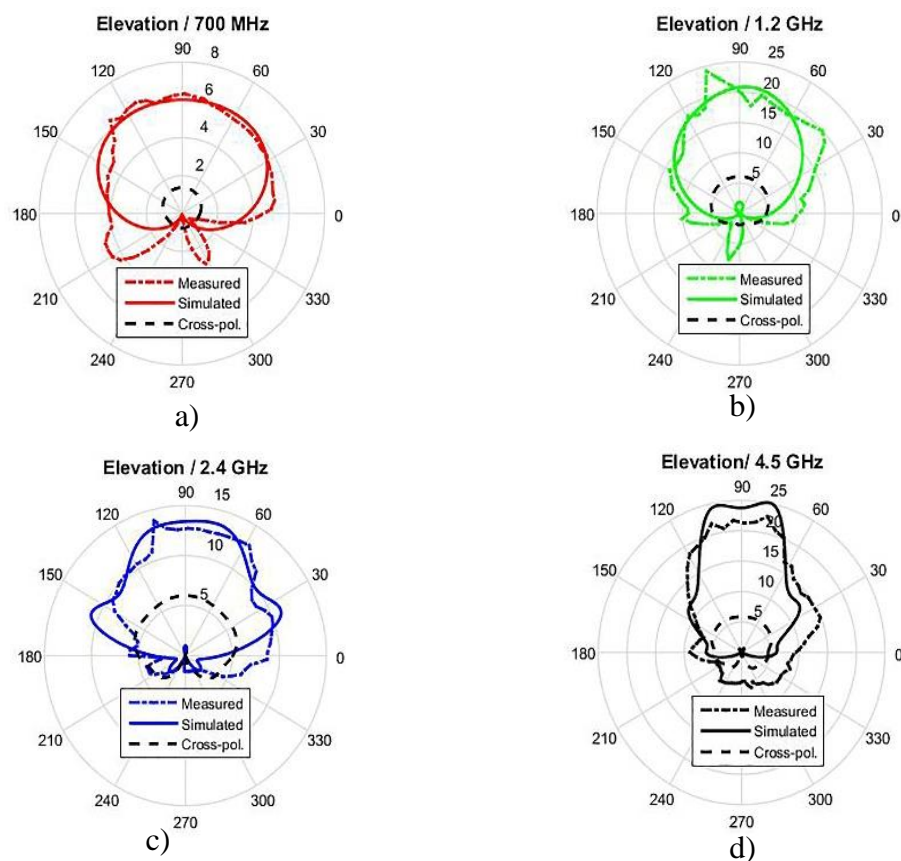


**Figure 45.** E-plane radiation pattern at a) 0.7 GHz, b) 1.2 GHz, c) 2.2 GHz, and d) 4.5 GHz.



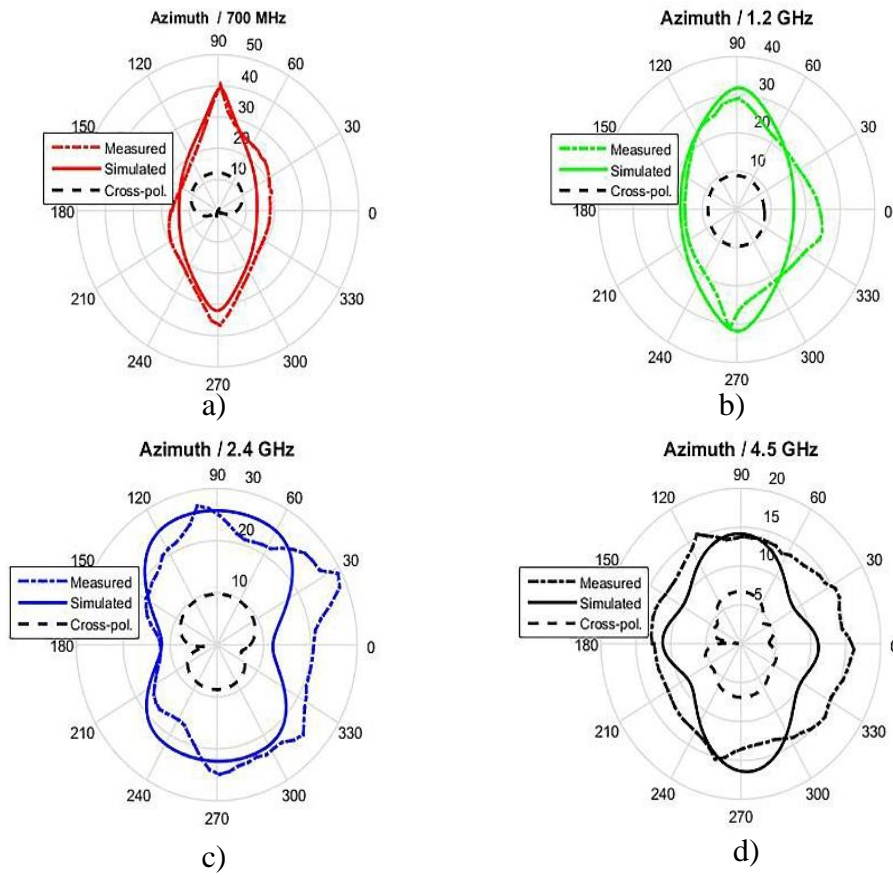


**Figure 46.** H-plane radiation pattern at a) 0.7 GHz, b) 1.2 GHz, c) 2.2 GHz, and d) 4.5 GHz

#### 5.2.4.4 Gain and antenna factor

The antenna factor measures the possibility of using the proposed antenna as a reference inside the EMC chamber. Moreover, it estimates the incident field on the antenna surface by knowing the received voltage across antenna terminals. Equation (2.4) is used to calculate the antenna factor in dB/m from the realized gain of the antenna in dBi [56].

$$AF = 20 \log \left[ \frac{2\pi}{\lambda} \sqrt{\frac{2.4}{10^{(G(dBi)/10)}}} \right]. \quad (2.4)$$

Figure 47 depicts the simulated and measured realized gain dBi. The relatively minor fluctuations in gain values 4.6 – 7 dBi reflect good behaviour in antenna factor values 24 – 41 dBm<sup>-1</sup>. Figure 48 shows the simulated and measured antenna factor versus frequency, while the antenna factor measurement values are presented numerically for each frequency band in Table 7. As can be seen, the realized gain and, consequently, the antenna factor values are agreeable with the typical values of a standard EMC antenna [14].

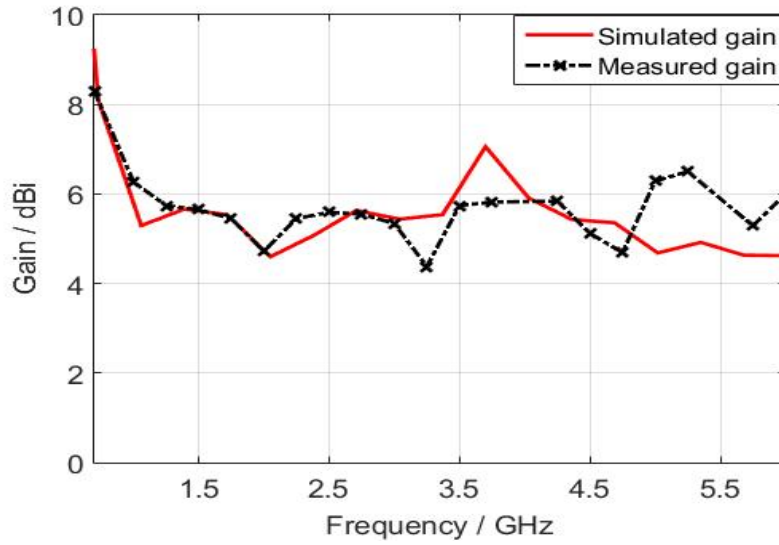


**Figure 47.** Presents the realized gain in dBi versus frequency

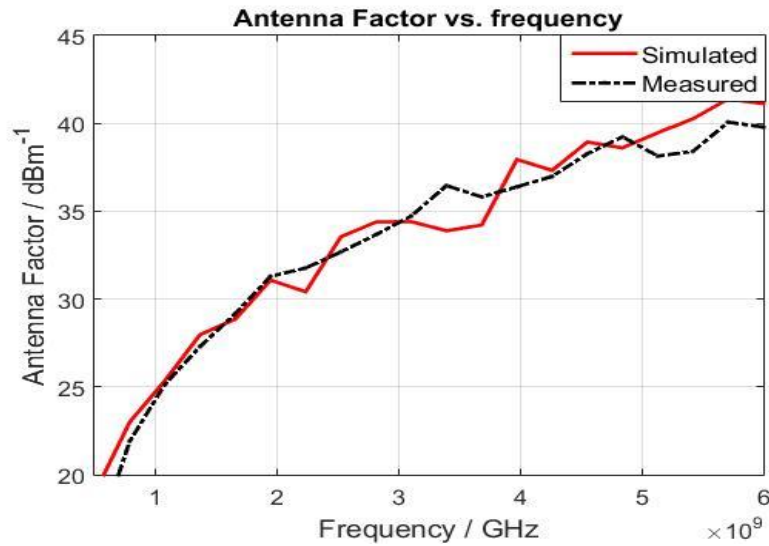


**Figure 48.** Presents the antenna factor in  $\text{dBm}^{-1}$  versus frequency

**Table 7.** Lists realized gain values and corresponding antenna factor versus frequency.

F / GHz	0.7	1	1.5	2	2.5	3	3.5	4	4.5	5	5.5	6
AF / $\text{dBm}^{-1}$	18	24.5	28.1	31.5	32.9	34.3	35.1	36.2	37.7	39.5	39.5	41.1
AG / dBi	7	5.7	5.6	4.7	5.2	5.4	6	6	5.5	4.7	5.4	4.6

### 5.2.5 Comparison of the proposed design with the literature reviewed

Recently, several PLPDA antenna designs were proposed to serve inside the EMC chamber for radiated emission and immunity tests. However, the proposed structures have employed different size reduction and bandwidth enhancement techniques. Table 8 lists the specifications for several proposed designs that have been presented to serve as a reference antenna for EMC measurements inside the chamber [27-32].

**Table 8.** A comprehensive comparison between the proposed design and literature papers

Reference	[27]	[28]	[29]	[30]	[31]	[32]	Our work
f / GHz	0.8 – 2.5	0.5 – 3	0.55 – 9	0.8 – 2.3	0.5 – 10	0.4 – 8	0.5 – 6
FBW / %	103	143	177	96.7	181	180	170
$\epsilon_r$	4.3	4.3	3.5	4.3	3.5	4.3	4.3
$\tau$	0.78	0.86	0.93	0.86	0.91	0.9	0.86
Gain / dBi	6.5	7 – 7.5	2.4 – 7.8	4.5 – 6.3	3 – 6	2.5 – 6.9	4.6 – 7
Dipoles no.	12	12	48	12	25	25	12
Size / $\lambda$	$0.426 \times 0.4$	$0.44 \times 0.25$	$0.49 \times 0.35$	$0.43 \times 0.37$	$0.36 \times 0.43$	$0.36 \times 0.37$	$0.28 \times 0.26$
Feeding	Typical	Balanced	Typical	Optimized	Typical	Typical	Balanced
Application	EMC	EMC	EMC	EMC	EMC	EMC	EMC

The size reduction and bandwidth enhancements are the main goals for all the presented work as they are controlled by the number of dipole elements and the spacing factor  $\tau$ . In particular, Ref. [29] offers wide bandwidth of about 8.5 GHz (FBW = 177%) with a high fluctuating gain of 2.4 – 7.8 dBi, while it requires 48 elements with a size of  $0.49 \times 0.355 \lambda_L$ . Dual-band dipole element technique was utilized in [31] to achieve a wide-bandwidth PLPDA antenna of 9.5 GHz (FBW = 181%), with a realized gain of 3 – 6 dBi, while it occupies a size of  $0.36 \times 0.43 \lambda_L$  using only 25 dipole elements. Consequently, our work aims to tackle size reduction and bandwidth enhancement goals. The proposed design utilizes a biconical shape dipole to achieve wide bandwidth of 5.5 GHz (FBW = 170%) with relatively low fluctuated gain of 4.6 – 7 dBi. Furthermore, it needs only 12 dipole elements based on a small size of  $0.28 \times 0.26 \lambda_L$ . Table 9 presents the miniaturization techniques that have been used in [29], [31] and the size reduction percentage compared to our works.



**Table 9.** Comparison between the miniaturization techniques used in [29], [31] and the proposed work

Reference	Size reduction	Miniaturization technique
[29]	27% and 20%	Using Hat loading and Top loading
[31]	40%	Using Dual-band dipoles
This work	50% and 50%	Using biconical dipoles

### 5.2.6 Comparison of the proposed structure with the commercial LPDA antenna (HyperLOG® 7060)

A comparison between the proposed structure and the HyperLOG® 7060 antenna from the AARONIA AG website is illustrated in Table 10 [57]. The commercial antenna HyperLOG® 7060 offers wide bandwidth (FBW = 158%) with a  $340 \times 200 \times 25$  mm size. In contrast, the proposed antenna has better relative bandwidth (FBW = 170%), with a compact size of  $170 \times 160 \times 1.6$  mm. Furthermore, both designs have acceptable fluctuation gain regarding the EMC applications and reflect good antenna factor values.

**Table 10.** Presents the design specifications of the proposed antenna and commercial antenna

Specifications	HyperLOG® 7060	Proposed design
Dimensions / mm	$340 \times 200 \times 25$	$170 \times 160 \times 1.6$
Design	Logarithmic-periodic	Logarithmic-periodic
Substrate	–	FR-4
Weight / g	250	70
Gain / dBi	3.1 – 5.5	4.6 – 7
Frequency range / MHz	700 – 6000	500 – 6000
Antenna Factor* <sup>1</sup> ) / dBm <sup>-1</sup>	26 – 41	24.5 – 41.18
RF Connector	SMA Female	SMA Female
Picture		

\*<sup>1</sup>) frequency range from 0.7 GHz to 6 GHz.

The antenna factor is mandatory to evaluate the incident electrical field during the radiated emission test. Therefore, it is axiomatic to present this factor of the proposed design and compare it with the standard *AF*. Regrettably, the literature-reviewed papers did not show the antenna factor. To make a fair comparison, the antenna factor of the proposed design and reviewed literature papers whose cover frequency band up to 6 GHz has retrieved from its realized gain in dBi using equation (2.4). The achieved results are also compared with the *AF* results of the commercial Hyperlog® 7060, as shown in Table 11. It is clear that the proposed antenna has an *AF* with lower tolerance than the commercial Hyperlog 7060 design due to the low fluctuations level in the achieved gain.

**Table 11.** Antenna factor comparison of the proposed design, the literature reviewed papers, and commercial design HyperLOG<sup>®</sup> 7060

F / GHz	AF [29]	AF [31]	AF [32]	AF Proposed design	AF HyperLOG 7060 [57]
0.5	20	20	22	18.1	–
1	23	25.5	29.5	24.5	26
1.5	27	28.5	30	28.1	29
2	30	31.5	30.5	31.5	31.5
2.5	32	33.5	32	32.9	33
3	34	36	34	34.3	35
3.5	35	37.5	35	35.1	36.5
4	36	39	36.5	36.2	37.25
4.5	37	40	37	37.78	37.75
5	37.9	41	38	39.5	38.5
5.5	39	41.5	38.5	39.54	40.5
6	40	42	40	41.18	41

It's worth mentioning the minimum 3dB beamwidth results of the proposed antenna are in line with the standard limits of the classical PLPDA antenna in CISPR as shown in Table 12. The minimum dimension of tangent line  $w$  can be calculated using equation (2.5).

**Table 12.** Comparison between the minimum distance  $w$  in both CISPR standard and proposed antenna at a minimum measurement distance  $d_s = 1\text{m}$ .

F / GHz	$\theta_{3dB}$ CISPR / °	$w$ CISPR / m	$\theta_{3dB}$ proposed design / °	$w$ proposed design / m
1	60	1.15	112	2.95
2	55	1.04	141	4.28
4	55	1.04	55	1.04
6	55	1.04	46.4	0.85

### 5.3 Design and Modelling of Stacked Log Periodic Biconical Dipole Array Antenna for Radiated Emission and Radiated Immunity Tests in EMC Measurements

The previously proposed antenna in **Section 5.2**, broadband printed log-periodic biconical dipole array (PLPBDA) antenna, is preferred for use in the radiated emission test rather than the immunity one. The reason behind that is the radiated immunity test requires some specific criteria, i.e., the electrical and magnetic fields propagating in the far-field must have almost the same power values with enough beamwidth to achieve the necessary UFA. This work overcomes this issue by designing, modeling, fabricating, and testing a dual-stacked log-periodic biconical dipole array (DSLBPBDA) antenna. The proposed structure consists of two LPBDA antennas stacked with angles of  $30^\circ$  and  $50^\circ$  respectively for the inner and outer layers.

Furthermore, the proposed design offers wide impedance bandwidth of (0.8 GHz – 6 GHz) and a relatively small size of  $176 \times 157 \times 160$  mm with the help of coaxial cable feeding method and biconical dipole technique, respectively. This antenna showed promising results in serving as a reference antenna for radiated emission and immunity tests by fulfilling the design's EMC requirements. For instance, a wide bandwidth antenna with a small size overcomes the test configuration issue, the stable radiation pattern provides a balanced structure, and wide beamwidth angles for E-and H-fields are mandatory to achieve the required coverage level of the electrical field in the UFA.

This part of work is structured as follows. **Section 5.3.1** presents the design procedure of the dual-stacked antenna, while the feeding method of this structure is described in **Section 5.3.2**. **Section 5.3.3** demonstrates the simulation and measurement results, and finally, **Section 5.3.4** briefly compares the proposed antenna and the classical antenna types SCHWARZBECK STLP9129 and SCHWARZBECK STLP9149. The results of this section have been accepted for publication in the AE conference [A8].

#### 5.3.1 Dual-stacked log periodic biconical dipole array antenna design

The purpose of this antenna is to meet the standards for radiated emission and immunity tests. Instead of creating a new LPDA antenna, this project was built upon the existing previously designed PLPBDA antenna with some modifications to create a dual-stacked antenna. The specifications of the proposed PLPBDA antenna in Section 5.2 are listed in Table 13.

**Table 13.** lists the PLPBDA antenna specifications for EMC measurements.

Specification	Details
Bandwidth / GHz	0.65 – 6.5
Size / $\lambda$	$0.28 \times 0.26$
Gain / dBi	4.6 – 7
Feeding method	Balanced transmission lines with direct feeding
Radiation pattern	Directive in E-plane Omni-directional in H-plane

The antenna specifications presented in Table 13 are suitable for radiated immunity tests except for the radiation pattern, i.e., the radiation pattern should have a directive field in both E and H-planes with almost the same power values. The solution for this issue is executed by using two PLPBDA antennas and stacking them with proper angles in a 3D configuration with some modifications. This 3D configuration will achieve the desired directive radiation pattern in E-plane and H-plane. Figure 49 presents the 3D geometrical shape of the stacked antenna in front and side views.

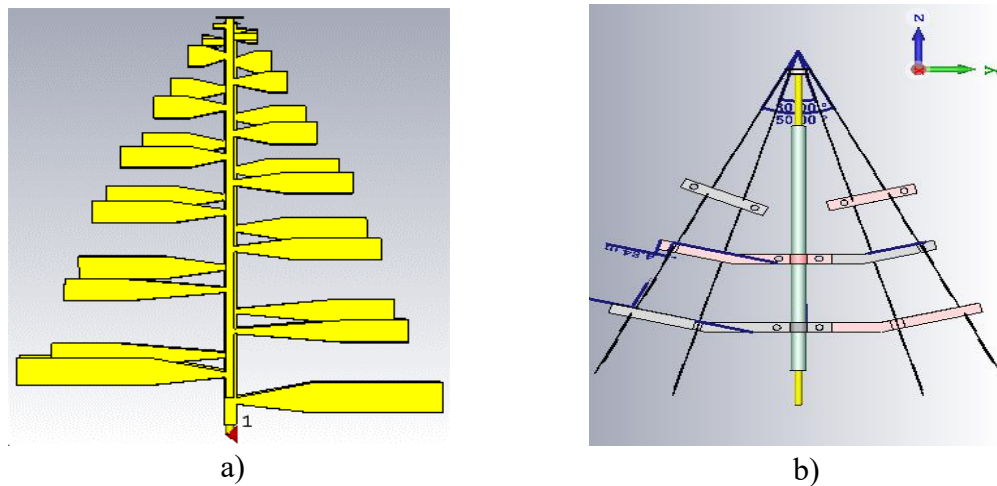


**Figure 49.** The geometrical shape of the stacked antenna, a) front view, and b) side view

### 5.3.2 Feeding method of the stacked antenna

By stacking two PLPBDA antennas at different angles, two parallel antennas of  $100 \Omega$  input impedance can be created instead of  $50 \Omega$ , as shown in Figure 50. This design uses a coaxial feeding method rather than a direct one, where these two feeding methods were well described in [58]. Additionally, the substrate material of the stacked antennas has been replaced with air to achieve an input impedance of  $100 \Omega$  for each antenna according to equation (5.12).

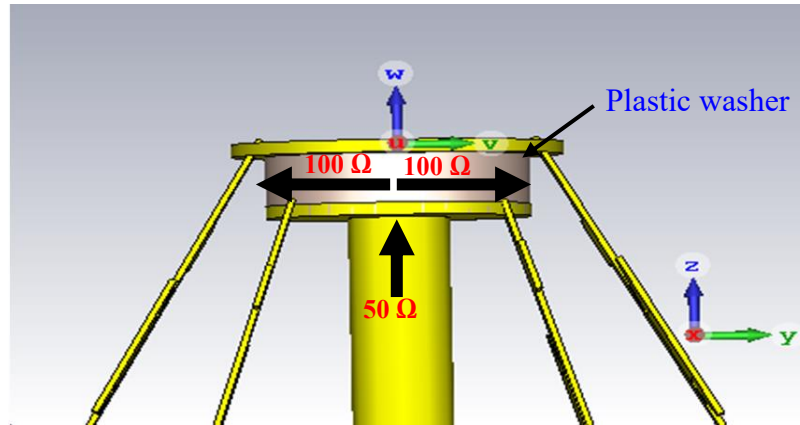


**Figure 50.** The energy transition from 50  $\Omega$  coaxial cable toward two identical antennas of 100  $\Omega$

Case-1: Fr-4 substrate  $\epsilon_r = 4.4$ :

$$z_0 = \frac{87}{\sqrt{4.4 + 1.41}} \ln\left(\frac{5.98 \times 1.6}{0.8 \times 3.01}\right) \Rightarrow z_0 = 50 \Omega,$$

Case-2: Air substrate  $\epsilon_r = \epsilon_0 = 1$ :

$$z_0 = \frac{87}{\sqrt{1 + 1.41}} \ln\left(\frac{5.98 \times 2}{0.8 \times 2.51}\right) \Rightarrow z_0 = 100 \Omega.$$

It is worth mentioning that the 2 mm value of substrate height  $h$  is valid only at the antennas' edges near the feeder. Because the angle between the stacked antennas gets wider when moving from the feeding point towards the radiators' edges, the  $h$  becomes larger than 2 mm. However, this should not cause any matching issues since the satisfied 2 mm height near the feeders matters the most for matching purposes. Accordingly, for achieving wide impedance matching, the widths of the transmission lines have been optimized in CST Microwave Studio.

### 5.3.3 Simulation and measurement results

This antenna was fabricated and tested at the University of West Bohemia, Faculty of Electrical Engineering, where the fabrication process was performed in two stages. Two aluminum plates were engraved with the help of a laser machine (Faculty of Mechanical Engineering) and then folded with angles of 30° and 50° to form the inner and outer parts of the antenna. On the other hand, the 3D printer was utilized to create the modeled plastic holders necessary to hold the antenna parts as designed and make it a robust structure. Moreover, a circular plastic washer with 2 mm thickness has been cut in a specific manner and inserted between the two folded plates to avoid the interconnection of the two layers at the narrow edge and help create a more robust antenna. The coaxial feedline was covered



by a plastic pipe, which is necessary to secure the plastic holders without any radiation effect. Figure 51 presents the prototype of the proposed structure.

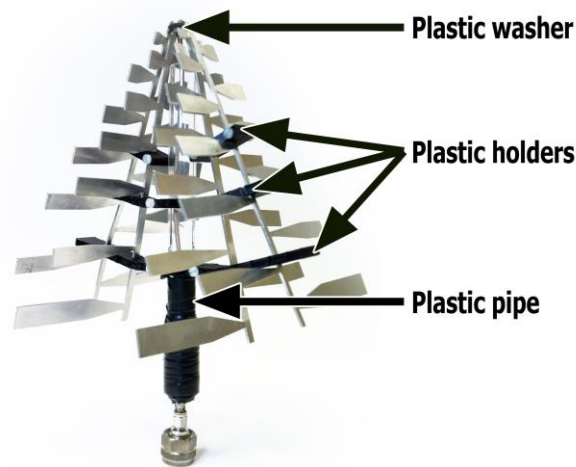


**Figure 51.** The prototype of the Dual-stacked log periodic biconical dipole array antenna (DSLBPBDA)

### 5.3.3.1 Reflection coefficient

The simulated and measured reflection coefficients of the proposed structure are presented in Figure 52. This antenna offers a wide bandwidth starting from 0.8 GHz up to 6 GHz, which makes it suitable for radiated emission and immunity tests.

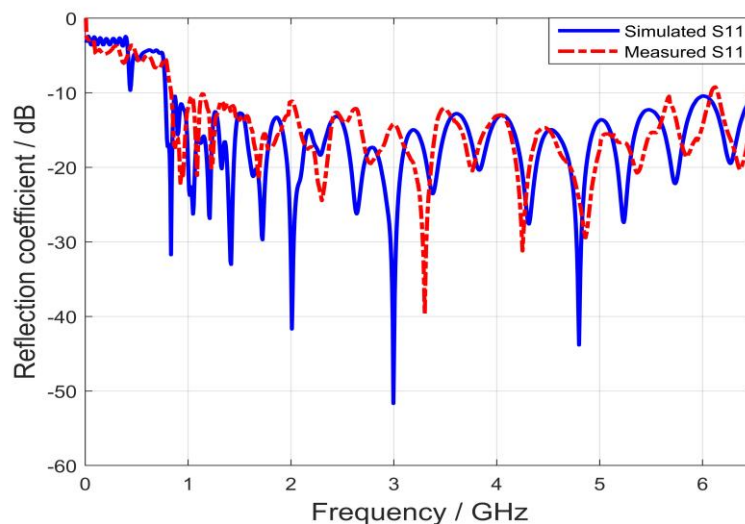


**Figure 52.** The simulated and measured reflection coefficient versus frequency

### 5.3.3.2 Realized gain and antenna factor

The realized gain in dBi represents how much power an antenna collects in one specific direction compared to the collected power by an omnidirectional antenna. In EMC

applications, high amplitude gain with low curve fluctuations are both crucial factors in achieving the preferred smooth and continuous antenna factor. This desired smooth antenna factor decreases the uncertainty and increases the stability of the measured results. Furthermore, the presented design achieved a high gain with an average value of around 8 dBi, as shown in Figure 53 a), while Figure 53 b) presents the calculated antenna factor accordingly. It is noteworthy that there is an improvement in the gain of the stacked antenna of about 2.5 – 3 dB compared to the PLPBDA antenna. The resulting gain enhancement is attributed to the orientation of the H-plane radiation pattern, which tends to be more directional rather than omnidirectional.

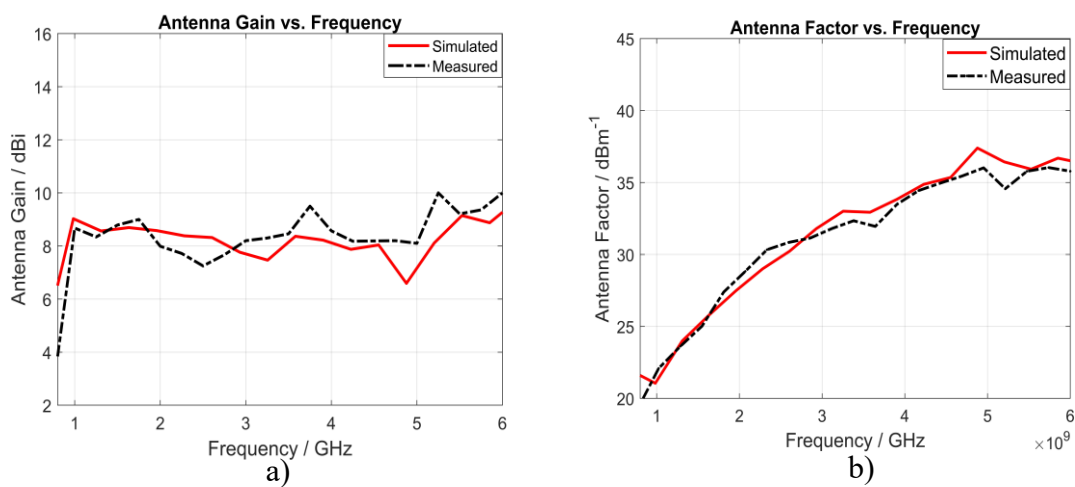


**Figure 53.** Realized gain and the corresponding antenna factor versus frequency

### 5.3.3.3 Radiation pattern

When designing an antenna for EMC measurement applications, the aspects of the radiation pattern are essentially considered. The radiation pattern can be either directive or omnidirectional, depending on the reference antenna type and in which EMC application is being used for. For instance, the omnidirectional antenna is preferred over the directive one when the reference antenna is intended for fast estimation of the background noise in the open test site measurements, as shown previously in Figure 28. It can be seen that both the E-plane and H-plane have an omnidirectional radiation pattern which is obligatory to find the EMI spreading in the background.

On the other hand, the radiated emission test demands a directive radiation pattern at least in one plane, E or H (end-fire radiation), with sufficient beamwidth angle to cover the device under the test during the EMC radiated emission test. The LPDA antenna is suitable

for this type of measurement since it offers a directive radiation pattern toward the E-plane and a directive radiation pattern in the H-plane with less power, as shown previously in Figure 46.

The radiated immunity test requires that the radiation pattern in both the E-plane and H-plane are directive and should have almost the exact maximum gain values (small tolerance) with sufficient beamwidth angles. These requirements are necessary to achieve an equal value of the electrical field level to create a UFA with 16 points, as shown in Figure 54, where the stacked antenna consists of two LPDA antennas.

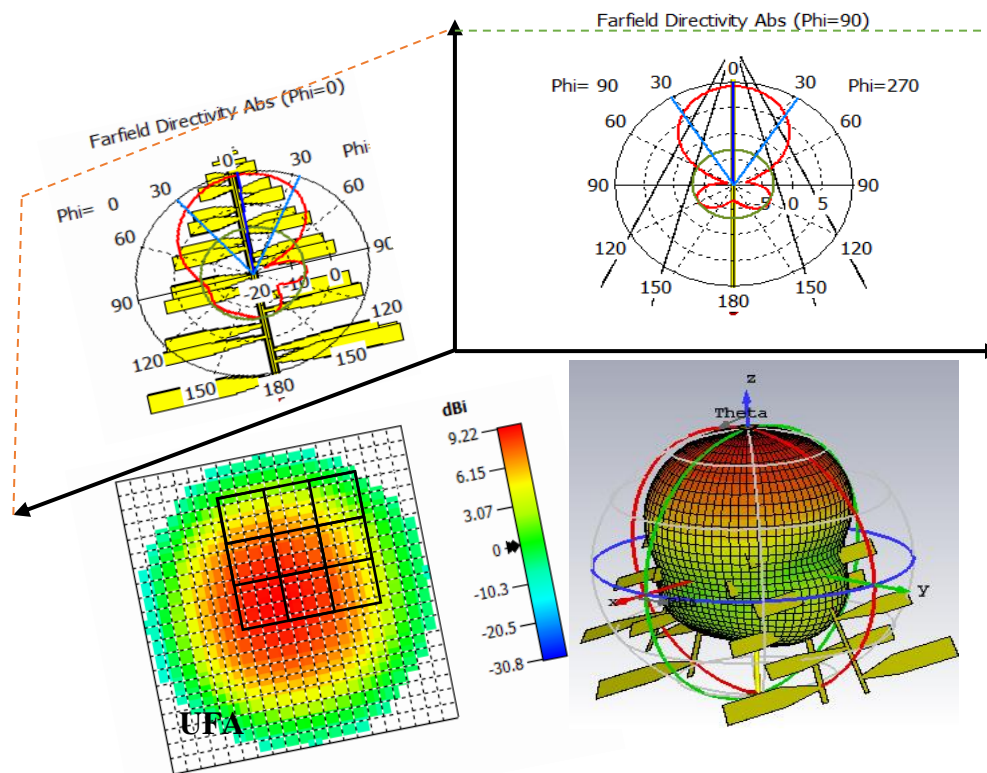


**Figure 54.** 3-D Simulated radiation pattern of the Stacked log periodic biconical dipole array antenna at 3 GHz

The EMC chamber at the University of West Bohemia has been used to measure the radiation pattern for the proposed stacked antenna, as illustrated in Figure 55. Figure 56 demonstrates the simulated and measured radiation pattern in polar form for both elevation and azimuth planes with different frequency bands starting from 1 GHz up to 6 GHz. The magnitude values of both radiation pattern planes are almost equal, as listed in Table 14, while it has suitable beamwidth angles through the whole operation bandwidth.

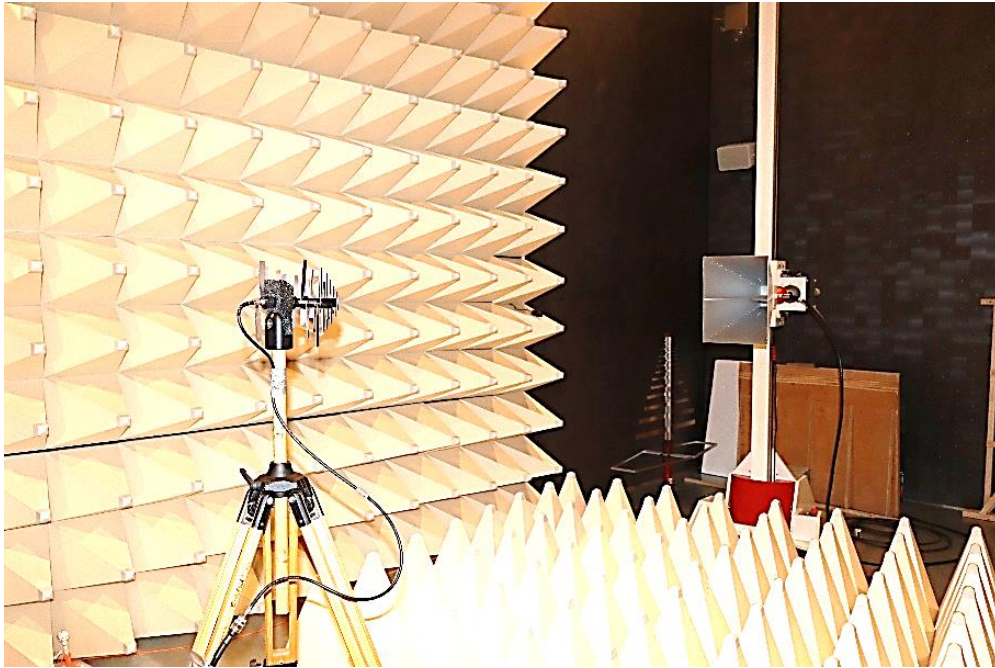
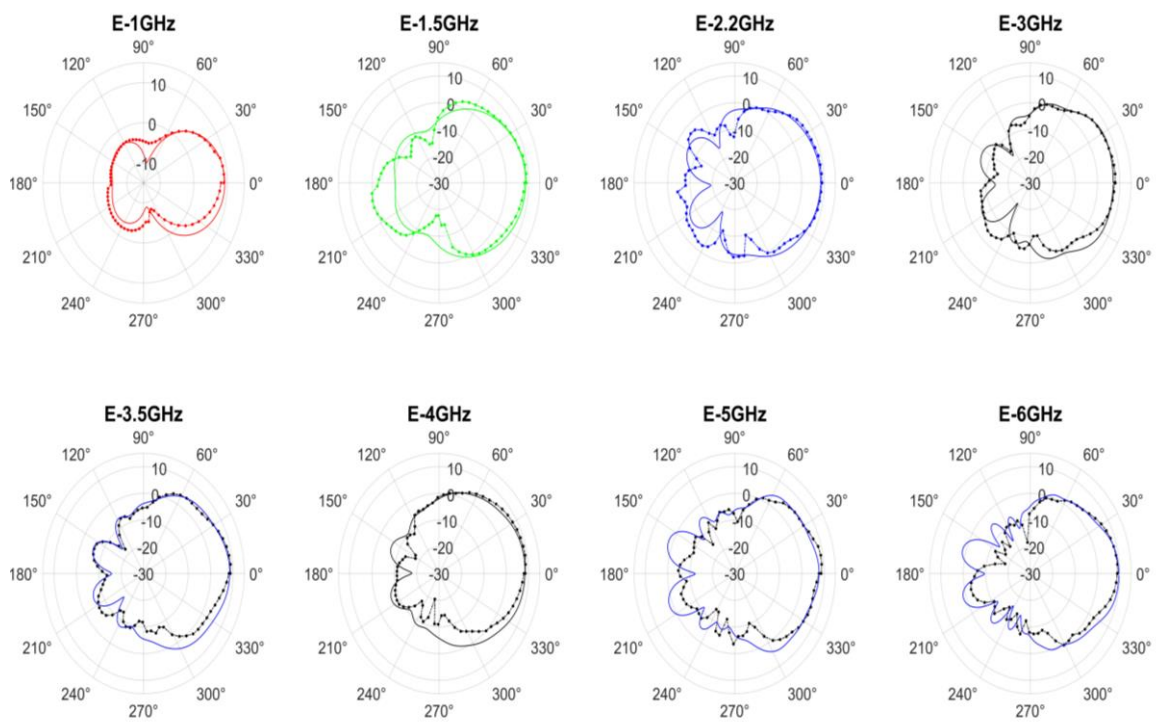
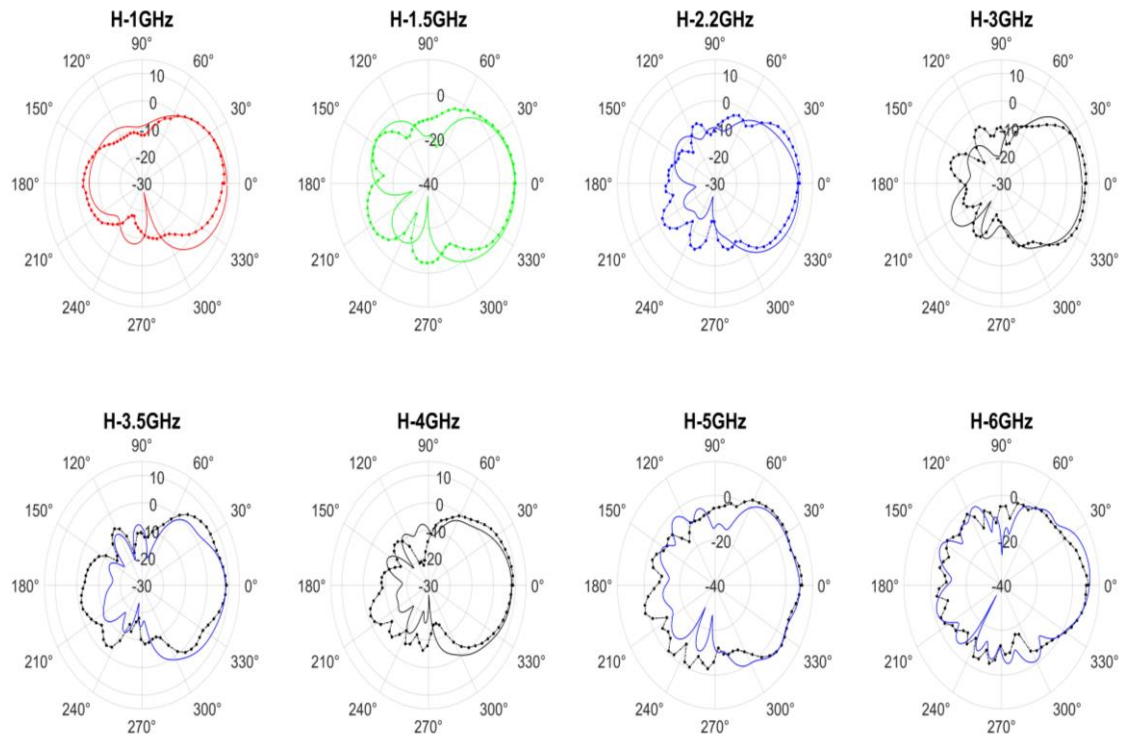


**Figure 55.** Radiation pattern setup for the stacked antenna inside the EMC chamber



a) E-plane



b) H-plane

**Figure 56.** The radiation pattern of the proposed antenna versus frequency: a) E-plane and b) H-plane

**Table 14.** Maximum points of radiation pattern for E and H plane versus frequency

Freq / GHz	1	1.5	2.2	3	3.5	4	5	6
E	9.14	8.68	8.33	7.6	8.5	8.33	7.65	9.49
H	9.197	8.63	8.94	7	8.5	8.33	7.65	9.49

#### 5.3.3.4 Beamwidth angle and uniform field area (UFA)

The half-power beamwidth (HPBW) angle is an essential parameter to investigate in EMC testing. It affects the measurements' accuracy and should be considered when designing an antenna for the EMC test. In the RE test, the HPBW angle determines the antenna's angular coverage and affects the emission measurements' accuracy. For example, in a test where the antenna generates an electromagnetic field to simulate a real-world scenario, a larger HPBW angle may result in a larger area being covered by the antenna, and, therefore, a more accurate representation of the real-world scenario is achieved. In the RI test, the HPBW angle of the transmitting antenna also determines the antenna's angular sensitivity and affects the immunity measurements' accuracy. For example, if the reference



antenna has a narrow HPBW angle, it may be more sensitive to signals from specific angles. Therefore, it may not accurately represent the real-world scenario where signals usually come from multiple angles.

The half-power beamwidth of the proposed antenna can be calculated using equation (2.6). The minimum beamwidth angle that satisfies the 3 m distance between the reference antenna and the DUT with a  $1.5 \times 1.5$  m UFA is  $28^\circ$ [59]. According to the angular beamwidth result of the proposed antenna, the minimum beamwidth angle is  $38^\circ$ . By plugging this value in equation (2.6), the minimum measurement distance is  $d_s = 2.1$  m for  $1.5 \times 1.5$  m UFA, which means this antenna can be moved toward the DUT and reduce the size of the chamber, where the measurement distance is feasible from 2.1 m up to 3 m. It should be highlighted that even with a 2.1 m measurement distance, the DUT is still in the far field area of 800 MHz. Moreover, Figure 57 shows the simulated results of half-power beamwidth angle for both E and H-planes versus frequency. It is obvious that the half-power beam width angles for both planes almost coincide.

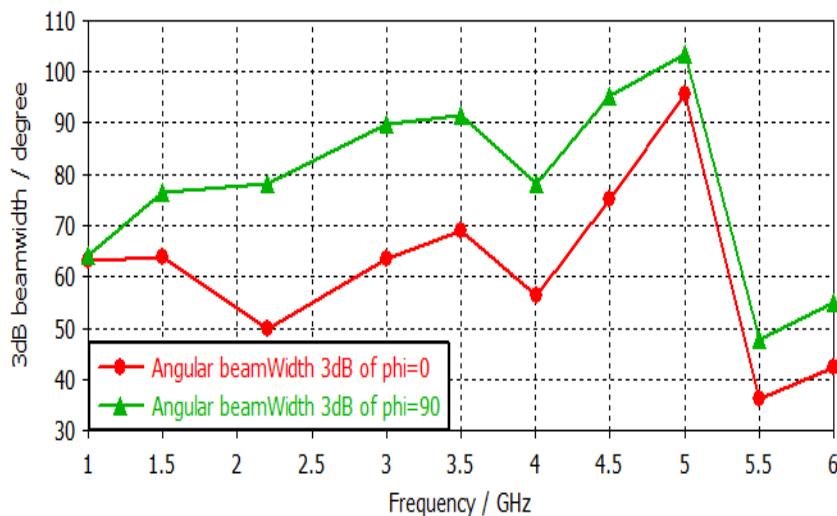


**Figure 57.** The Half power beamwidth angle of the proposed antenna vs. the frequency

On the other hand, the UFA is a square area of  $1.5 \times 1.5$  m with 16 points of 0.5 m separation between every two adjacent points. This UFA is located at a 3 m distance from the reference antenna and mounted on a turntable of 0.8 m height. An electrical probe LSProbe 1.2 (frequency range 10 kHz – 8.2 GHz) is utilized to measure the strength of the electrical field of each point of UFA. The acceptable field strength level at 75% of the estimated points should be within the 0 – 6 dB limit.

### 5.3.3.5 Fast evaluation of UFA for RI test

To accurately evaluate the UFA points, it is crucial to confirm the uniformity of the electromagnetic field at precise locations within the UFA. The electric field strength is measured at different points within the UFA using a calibrated electric field probe. This probe is a small dipole antenna that is specifically designed to measure the electric field strength at a particular frequency. At every UFA point, the probe is positioned, and the electric field strength is measured and recorded.

In the EMC chamber, the electrical probe LSProbe 1.2 (frequency range 10 kHz – 8.2 GHz, maximum measured level up to 30 kV/m) is usually utilized to measure the strength of the electrical field. Two possibilities exist for the calibration process – constant power or constant field methods. However, this process consumes a long time to measure the value at each frequency step. The alternative approach is to use a wideband antenna and a spectrum analyzer with a tracking generator to overcome the time consumption. Figure 58 displays the block diagram of this approach.

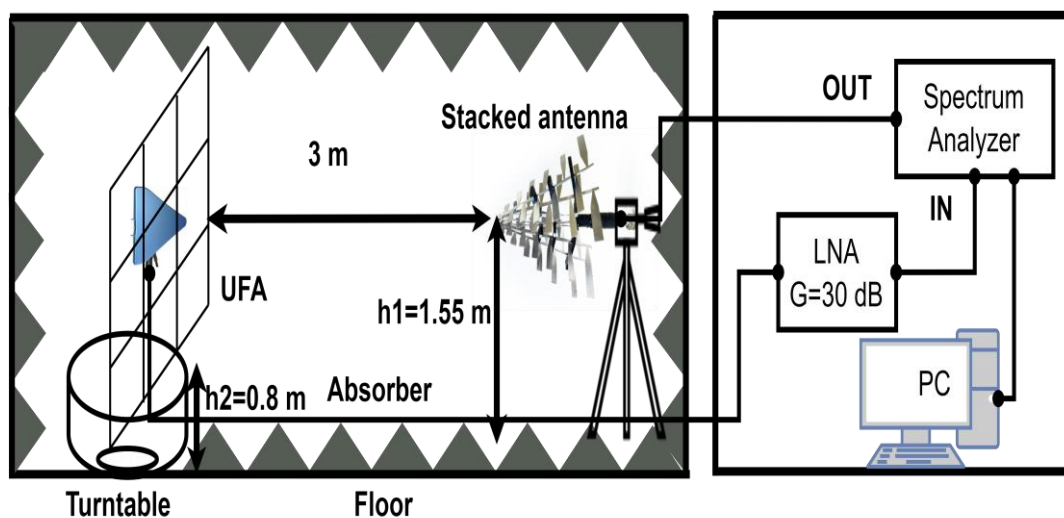


**Figure 58.** The block diagram of the proposed method using PLPDA antenna for evaluating UFA points.

To measure the frequency spectrum across the UFA grid, the spectrum analyzer's tracking generator is connected to the transmitting antenna, and the receiving antenna is gradually moved to each point on the grid. The spectrum analyzer's input is then connected to the receiving antenna to quickly measure the entire frequency spectrum. Once measurements have been taken at all points on the UFA grid, the results can be evaluated. If the level at all points from the maximal one is  $L = L_{\max} - 6$  (dB), there is a high probability

that the final UFA calibration will pass the test according to the standard IEC 61000-4-3:2020 [60].

Figure 59 presents the measurement setup of the electric and magnetic field strength for each point of UFA inside the EMC chamber. The stacked antenna serves as a transmitting antenna, and the PLPDA antenna is utilized to estimate the electric and magnetic field by changing its direction vertically and horizontally, respectively. Figure 60 demonstrates the electrical and magnetic field distribution versus frequency for the 16 points. It is apparent that the E and H fields have small fluctuations within the tolerance limit.

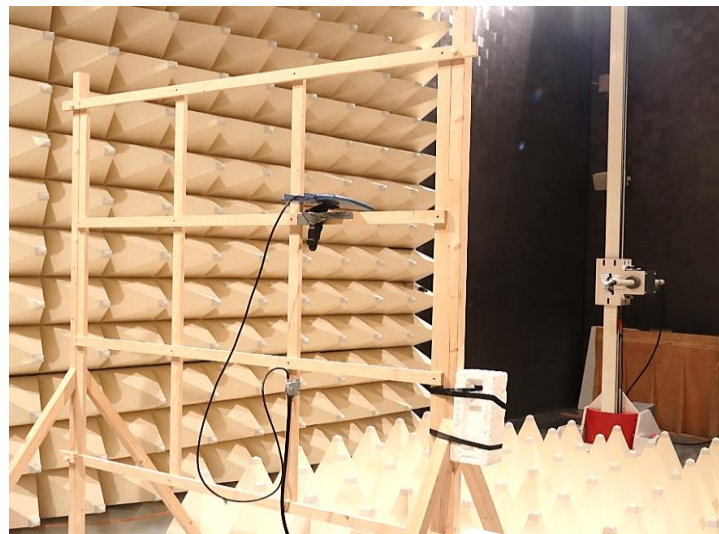


**Figure 59.** Measurements setup of the electric and magnetic field strength of UFA

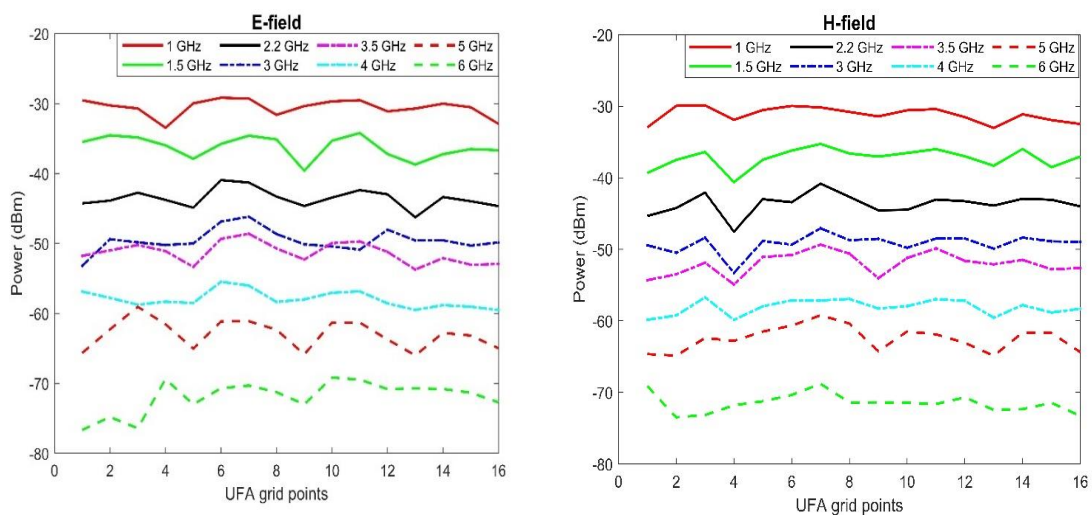


**Figure 60.** Measured results of electrical and magnetic field distribution of UFA

To achieve the acceptable field strength level, the maximum difference ( $\Delta$ ) between the 16 UFA's points has been calculated in MATLAB and presented in Table 15.



**Table 15.** lists the maximum difference between UFA points for electric and magnetic fields

F / GHz	1	1.5	2.2	3	3.5	4	5	6
$\Delta E$ / dB	4.29	5.39	5.32	7.02	5.12	4.06	6.96	4.49
$\Delta H$ / dB	3.15	5.39	6.72	6.24	5.57	3.15	5.65	4.68

To satisfy the condition of UFA where at least 75% of the points should have a difference less than 6 dB. We first calculated the difference between each point and the minimum point at each frequency. It gives us a new vector with 16 elements, representing the differences between the points. We then count the number of elements in this new vector that are less than or equal to 6 dB and divide by the length of the vector to get the percentage as listed in Table 16.

**Table 16.** lists the percentage of UFA points that have less than 6 dB differences.

F / GHz	1	1.5	2.2	3	3.5	4	5	6
E-field / %	100	100	100	87.5	100	100	93.75	75
H-field / %	100	100	93.75	93.75	100	100	100	100

It is clear that the UFA condition (75% points has maximum difference ( $\Delta$ ) < 6 dB) has been satisfied for both E and H fields.

### 5.3.3.6 Polarization and axial ratio

The polarization of an antenna refers to the orientation of the electrical field in the plane of the wave it propagates. Linear polarization is an essential factor in designing reference antennas for EMC measurement applications, where the electrical field is oriented on only one axis, either  $E_x$  or  $E_y$ . The axial ratio ( $AR$ ) is a measure of the ratio between the major (Co-polarized) and minor (Cross-polarized) components of the electrical field. It is used to determine the type of polarization. The antenna exhibits circular polarization when the  $AR$  is less than 3 dB. An  $AR$  with an infinity value reflects linear polarization, and the range between 3 dB and infinity is assigned to elliptical polarization. However, there is an ambiguity in the boundary line between linear and elliptical polarizations since the infinity value of  $AR$  is relative. In other words, linear polarization can be viewed as a particular case of elliptical polarization. In the field of research, there are varying views on the acceptable limit for linear polarization. Some experts believe an  $AR$  of 10 dB is the benchmark [61], while others endorse an  $AR$  of 20 dB [62]. However, the stacked antenna used in this study provides linear polarization with an impressive  $AR$  of 40 dB across the entire frequency range (0.8 – 6 GHz), as depicted in Figure 61.

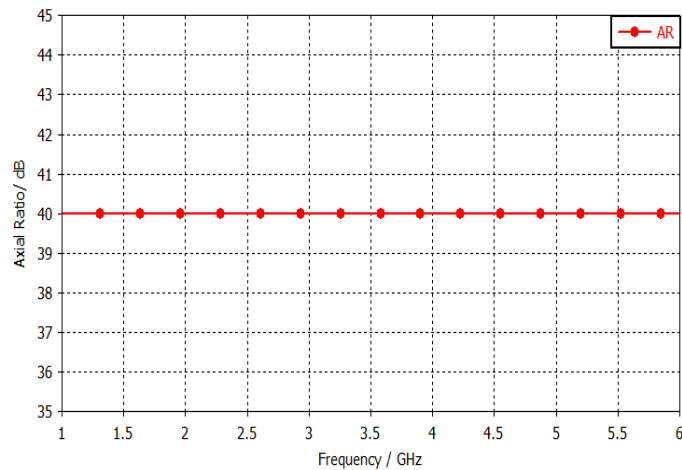


**Figure 61.** The simulated results for axial ratio in dB versus frequency

### 5.3.4 Comparison of the proposed structure with SCHWARZBECK antenna types of STLP9129 and STLP9149

SCHWARZBECK is a well-known brand that produces stacked antennas designed to measure RE and RI tests in EMC measurements. However, the characteristics of the proposed antenna have been compared with the structure SCHWARZBECK STLP9129 [63] and STLP9149[64], as shown in Table 17.

**Table 17.** Illustrates design specifications of the proposed antenna and commercial antennas

Specifications	STLP9129[63]	STLP9149[64]	Proposed design
Size / mm	1.69 × 1.64 × 2.02 m	460 × 270 × 270	160 × 157 × 176
Size / $\lambda_0$	0.394 × 0.382 × 0.471	1.07 × 0.63 × 0.63	0.373 × 0.366 × 0.411
Design	Logarithmic-periodic	Logarithmic-periodic	Logarithmic-Biconical periodic
Polarization	Linear	Linear	Linear
Material	Aluminium	Brass	Aluminium
Weight / g	10.2 Kg	3.7 Kg	0.135 Kg
Gain / dBi	8.6 with a ripple < +/− 2.3 dB	10.3 with a ripple +/-1.5 dB	8.6 with a ripple < +/− 1.5 dB
Pattern type	Directional	Directional	Directional
Frequency range / MHz	70 – 1000	700 – 9000	800 – 6000
Antenna Factor <sup>*1)</sup> / dBm <sup>-1</sup>	21.5 – 35	18 – 40	20 – 37
RF Connector	SMA Female	SMA Female	SMA Female

Picture



\*1) frequency range from 0.8 GHz to 6 GHz.

To ensure a fair comparison between the proposed and commercial designs, the size of the antennas has been expressed in terms of wavelength. The proposed antenna has been created by taking advantage of the size reduction of the PLPBDA antenna. The lightweight of the proposed antenna is a significant advantage over commercial structures. This is particularly important for EMC measurements, where the antenna needs to be conveniently moved and replaced within the chamber. The proposed design adds more credit since other parameters, such as gain ripple and antenna factor, are consistent across all structures.

Table 18 lists the antenna factor numerical values for all designs across different frequency bands. It's evident that the maximum difference ( $\Delta$ ) between them is approximately 3 dB, which is an acceptable level in terms of stability and low uncertainty. Meanwhile, Table 19 shows a comparison of the numerical values for the half-power beamwidth. Our proposed antenna meets the minimum angle requirement of  $28^\circ$  for both the vertical and horizontal directions.

**Table 18.** Comparison between the numerical values of  $AF$  for both proposed and commercial antennas.

F / GHz	AF STLP9129 / dBm <sup>-1</sup>	AF STLP9149 / dBm <sup>-1</sup>	AF Proposed antenna / dBm <sup>-1</sup>	$\Delta$ /dB (pro.,STLP9129)	$\Delta$ /dB (pro.,STLP9149)
0.7	18.5	17.63	20	1.5	2.37
1	20	20.16	21.5	1.5	1.34
1.5	22.5	23.54	25	2.5	1.46
2	25.5	25.54	27	2.5	1.46
2.5	28.5	27.32	30	1.5	2.68
3	30	29.38	31.5	1.5	2.12
3.5	32	30.23	33	1	2.77
4	32.5	30.81	34	1.5	3.19
4.5	33.5	32	35	1.5	3
5	34	33.7	36	2	2.3
5.5	35	34.51	34	-1	-0.5
6	37	36.09	35.1	-1.9	-0.99

**Table 19.** Comparison between the numerical values of half-power beamwidth for both proposed and commercial antennas.

F / GHz	STLP 9129 E-plane /	STLP 9129 H-plane /	STLP 9149 E-plane /	STLP 9149 H-plane /	Proposed E-plane/	Proposed H-plane /
1	45	54	55	58	66.5	62.4
2	47	49	47	52	79.5	55.3
3	52	50	54	52	89	68.4
4	40	40	41	41	80.7	56.6
5	41	42	41	43	104	95.7
6	41	43	43	45	56.8	44.6

## 5.4 Design and Modelling of Spiral Circular Magnetic Probe for Near Field Measurements

Far-field measurements provide us details about a device's radiated emission and immunity at a specific distance. However, it cannot accurately determine the location of the potential EMI source. On the other hand, near-field measurements can precisely provide information about the EMI source location as it is conducted in the proximity area of the DUT. This study uses CST Microwave Studio to examine the development of a circular magnetic probe for measuring near-field signals in the frequency range of 1 MHz to 1 GHz. The investigation includes a comparison of conventional and microstrip reference boards and an analysis of different loop configurations such as one-face three-loop, two-face three-loop, and one-face one-loop. The goal is to comprehensively understand magnetic probe design using software like CST Microwave Studio. In order to present our ideas coherently, this work is divided into the following sections: **Section 5.4.1** describes the design and analysis of the reference board. The magnetic probe design method is presented in **Section 5.4.2**, while **Section 5.4.3** shows the simulation results like magnetic field distribution, reflection coefficient, and isolation. The results of this section have been published in the AE conference [A3] and EI conference [A1].

### 5.4.1 Reference board design

In order to model the designed magnetic probe accurately in simulations and measurements, a reference board is required. This board generates a plane wave of the electromagnetic field, providing us with the magnetic field's reference values (without the probe). These reference values are then compared against the magnetic field results of the proposed probe. The conventional reference board comprises a cylindrical line of diameter  $d_o = 1.2$  mm located at the height of  $h = 2.05$  mm above the ground plane and terminated with  $50 \Omega$ . There is an air layer in between the cylindrical line and the ground plane, and this type is well-known due to the easy realization and calculation of the electromagnetic fields around the structure using image theory as described in Diagram 2 and Diagram 3:

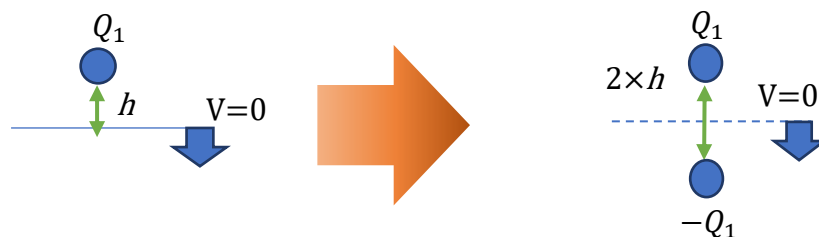


**Diagram 2.** Using image theory for conventional reference board



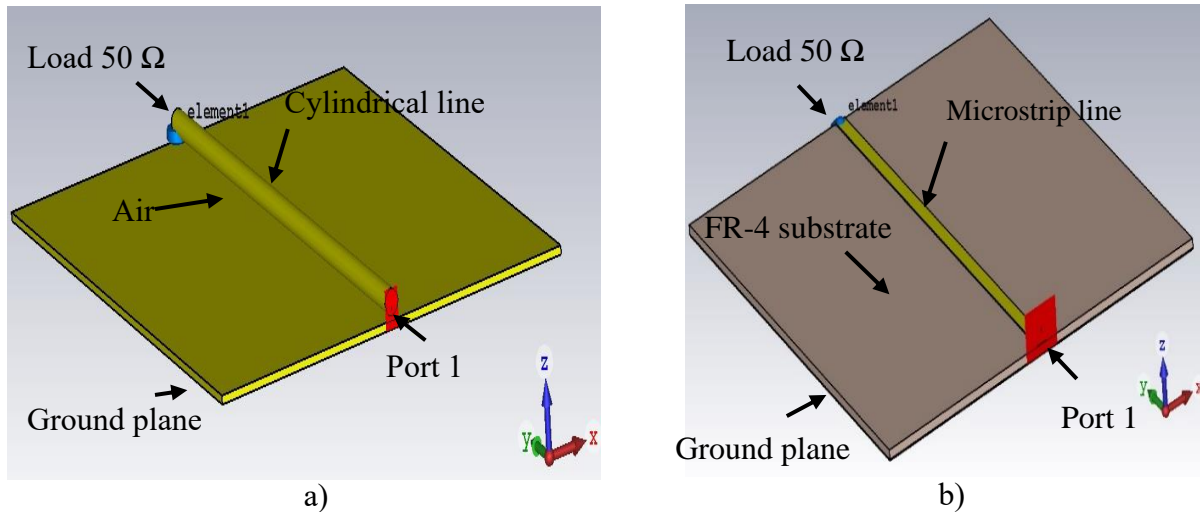


**Figure 63.** The conventional and proposed reference plane for the test: a) conventional reference plane, and b) microstrip reference board

Figure 64 illustrates the tangent components of the magnetic field ( $H_y$ ) at low and high frequencies for both conventional and microstrip reference boards. The achieved accuracy of such component with a microstrip reference board is superior to that of a conventional one, as evidenced by the two minimum points on the solid red curve compared to the solid blue curve. This advantage can be attributed to the fact that the microstrip reference plane and the DUT are both based on PCB technology and have nearly identical material properties.

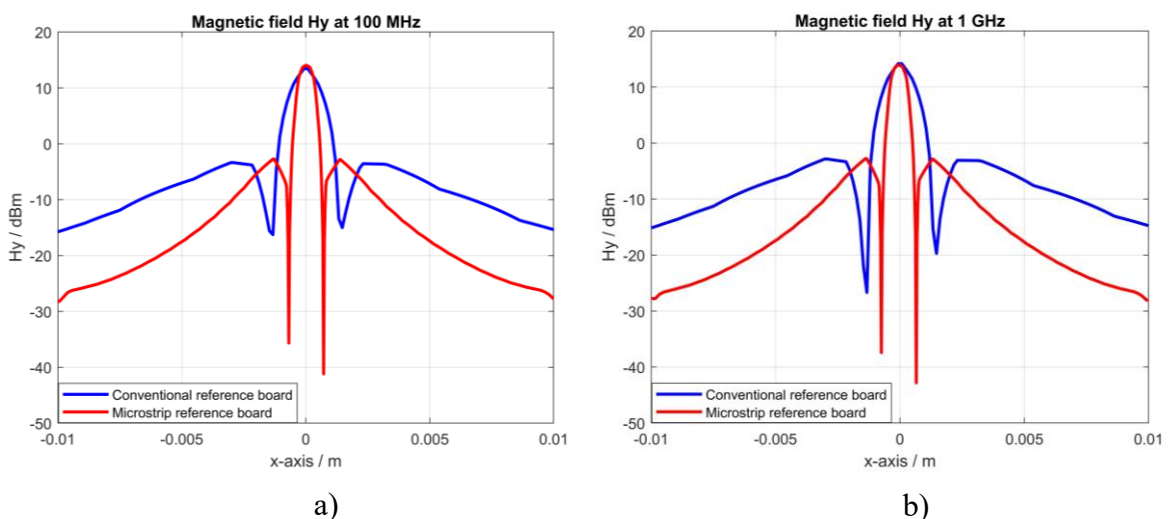


**Figure 64.** The magnetic field results of conventional and microstrip reference board  
a) 100 MHz and b) 1 GHz

### 5.4.2 Spiral circular magnetic probe design

To proceed, we need to assess the magnetic field generated by the proposed probe and compare it with the estimated magnetic field above the reference board (known as the reference field). The reference magnetic field value at different distances can be computed in CST Microwave Studio by modeling a line across the reference board and calculating the magnetic field at each point on this line. However, evaluating the magnetic field induced by the probe directly through CST Microwave Studio Software is not feasible. Instead, we can estimate the voltage induced across the probes' terminals at each point.

The induced voltage can be obtained by sweeping the proposed magnetic probe from the negative x-axis to the positive x-axis across the reference board. There are various geometrical shapes that can be utilized for the microstrip magnetic probe. In this study, a spiral circular magnetic probe has been designed and modeled in CST Microwave Studio with two different configurations. Figure 65 shows the geometrical shape of the proposed probe and its modeling in the CST Microwave Studio, while the optimum dimensions of the proposed probe are illustrated in Table 20.

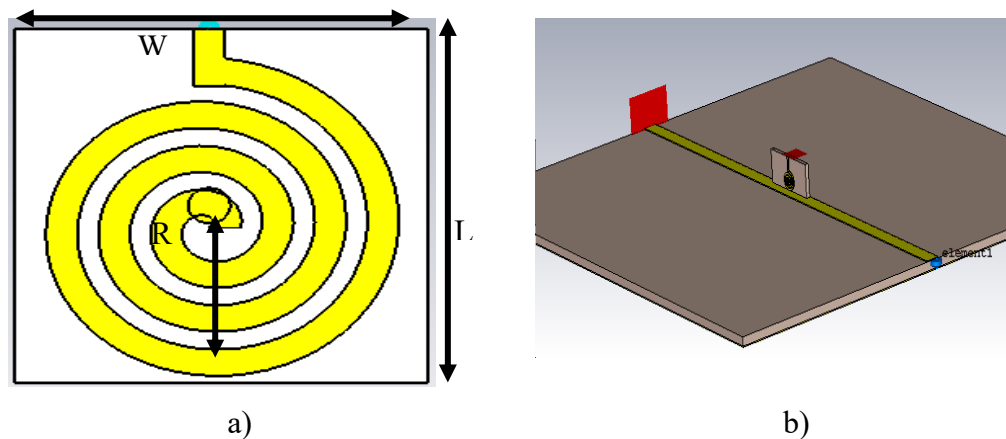


**Figure 65.** The proposed magnetic probe a) the geometrical shape and b) modeling in CST Microwave studio

**Table 20.** Illustrates the dimensions of the proposed probe

Parameter	Value / mm	Parameter	Value / mm
Height ( $h$ )	1.6	Width ( $W$ )	4
Length ( $L$ )	5	$R1$	1.5
Loop width	0.3	Number/turns	3
Gap	0.2		

Regarding Table 20, the loop dimensions are selected based on equation (5.13) for a single loop (outer loop) as a Loop Gap Resonator, then extra loops are loaded to increase the electrical length and hence, get the desired results like resonance frequency and bandwidth.



$$f_0 = \frac{v_0}{2\pi r} \sqrt{\frac{t}{\pi w}}. \quad (5.13)$$

Equation (5.13) demonstrates that the antenna factor is inversely proportional to the cross-section area  $S$ . The cross-section area can be calculated using equation (5.14), which utilizes the circular area formula as the probe's spiral circular shape. The antenna factor for this shape has been evaluated and implemented using MATLAB software. The calculation of the antenna factor using MATLAB is shown in Figure 66.

$$S = 2\pi r^2. \quad (5.14)$$

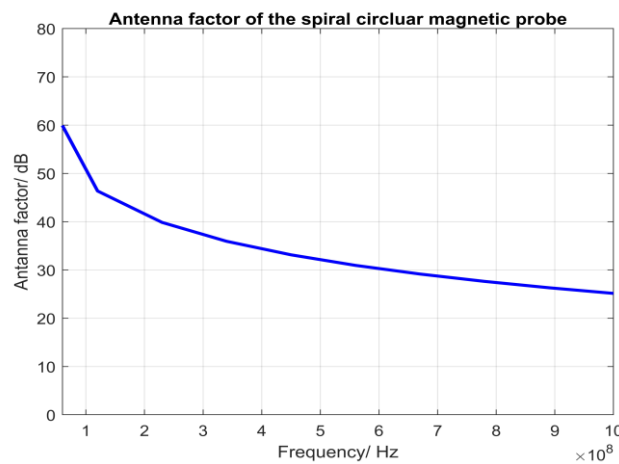


**Figure 66.** Antenna factor vs. frequency for the proposed magnetic probe

#### 5.4.3 The Simulation results

Two configurations of the printed magnetic probe have been designed and modeled using CST Microwave Studio, a One-face three-loops (1F3L) probe and a Two-face three-loops (2F3L) probe. Figure 67 presents the geometrical shape of these configurations.

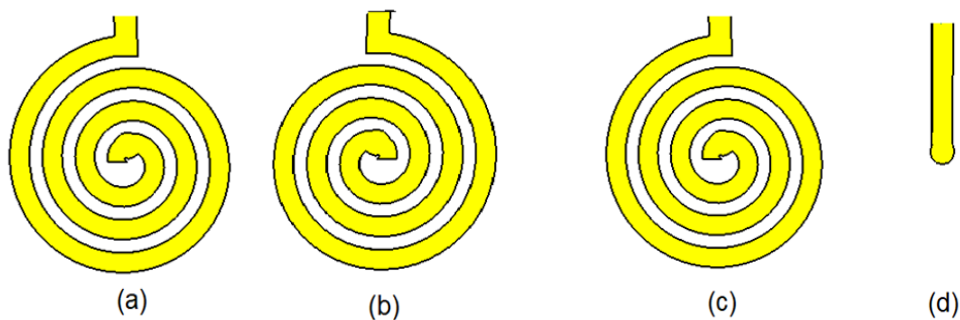


**Figure 67.** Two faces (2F) probe versus one face (1F), a) front view (2F), b) back view (2F), c) front view (1F), and d) back view (1F)



The distribution of magnetic field results versus x-distance for both structures at different frequencies are shown in Figure 68.

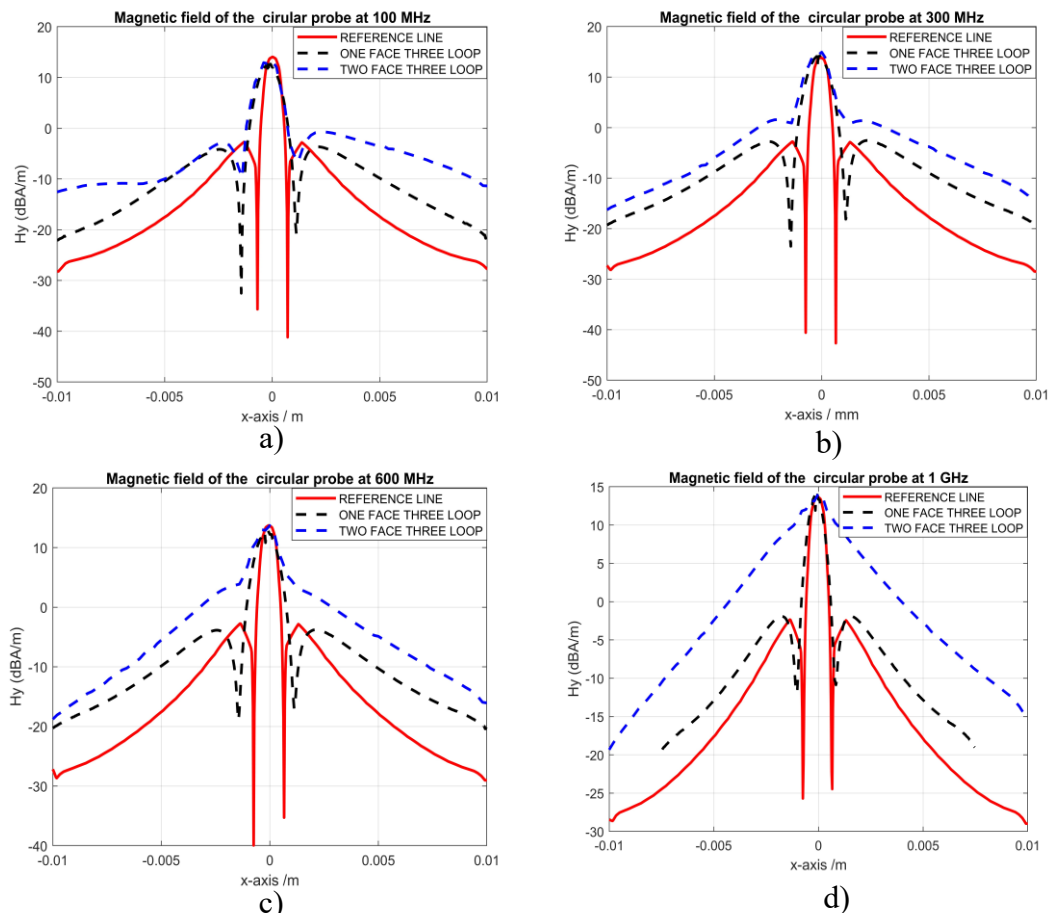


**Figure 68.** Magnetic field estimation for both probe configurations at low and high frequencies, a) 100 MHz, b) 300 MHz, c) 600 MHz and d) 1 GHz

The two proposed structures can detect the magnetic field above the reference board at low frequencies (100 MHz). However, the 1F3L configuration has higher accuracy rather than the 2F3L design. I.e., the two minimum points of the black-dashed curve show better performance than the two minimum points of the blue-dashed curve compared to the reference field (red curve). This advantage of the 1F3L probe is due to its more selective estimation area than the (2F3L) probe. When the frequency goes up from 100 MHz, the accuracy of the (2F3L) probe decreases, while the (1F3L) probe maintains the same level of precision. This is clearly demonstrated in Figure 68 b) & c), where the accuracy of the (2F3L) probe drops at 300 and 500 MHz, respectively. Finally, at high frequencies, particularly (1 GHz), the (2F3L) probe cannot detect the magnetic field due to the absence of minimum points. However, the (1F3L) probe can detect the magnetic field as it has two minimum shaping points of  $-30$  dBA/m and  $-20$  dBA/m, as illustrated in Figure 68 d).

The behaviours of detecting the magnetic field distribution demonstrated in Figure 68 a) – d) can be verified with the S11 parameter. Figure 69 shows the S11 parameter of the proposed antenna for both configurations (2F3L and 1F3L). Unlike the antenna, the bandwidth of this magnetic probe will account for below  $-3$  dB. The intersection line of  $-3$  dB with a blue-dashed curve will get the point with a projection at 0.6 GHz, precisely where the 1F3L probe is starting to lose its sensitivity.

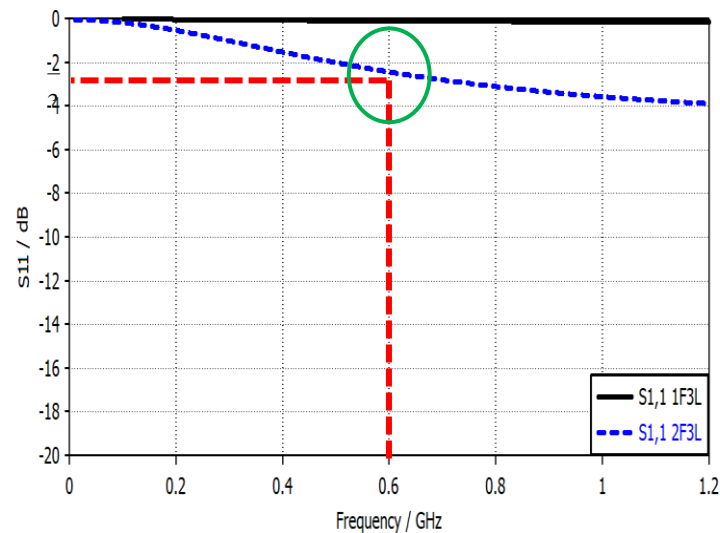


**Figure 69.** S11 parameters of the proposed probes (1F3L and 2F3L) vs. frequency

When designing a magnetic probe, it is essential to consider its isolation, which refers to its ability to reduce unwanted electrical fields. The magnetic probe can detect both electrical and magnetic fields in the nearby area. The S12 parameter measures the magnetic and electrical fields when the probe is parallel and perpendicular to the microstrip line of the reference board test, respectively. As seen in Figure 70, the isolation between the electrical and magnetic fields is approximately 12 dB.

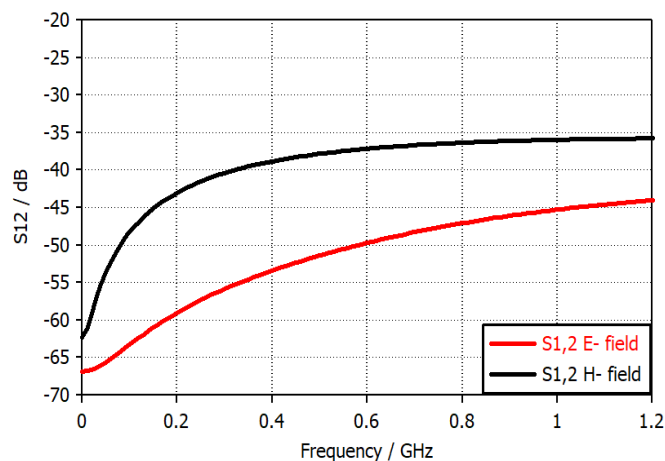


**Figure 70.** S12 parameters of the proposed probes (1F3L)

To effectively carry out our investigations, it is crucial that we conduct a comparison between the 1F1L and 1F3L configurations. A visual representation of these configurations can be found in Figure 71.

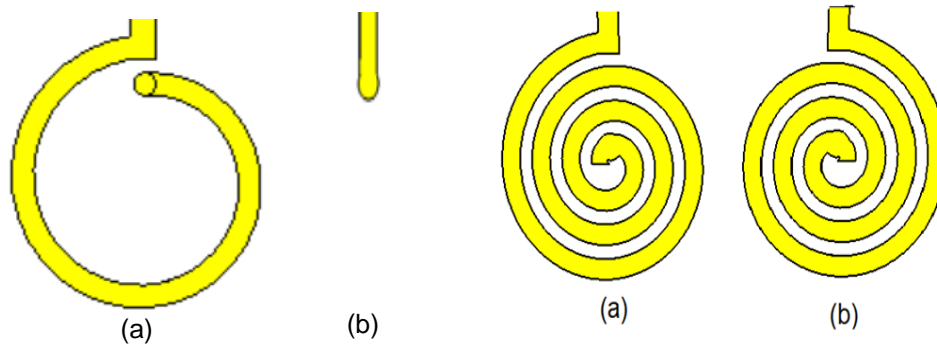


**Figure 71.** One face one-loop (1F1L) probe versus one face three-loop (1F3L), a) front view (1F1L), b) back view (1F1L), c) front view (1F3L), and d) back view (1F3L)

Figure 72 displays the S11 parameter for two configurations: 1F3L and 1F1L. The configuration with 1F1L exhibits a broader frequency bandwidth compared to the 1F3L design because decreasing the number of turns or loops results in a higher frequency range by reducing the parasitic capacitance.

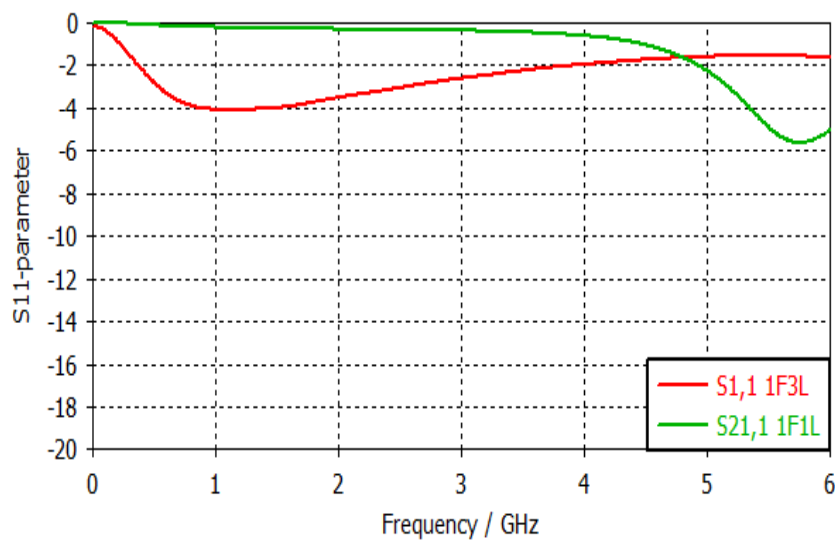


**Figure 72.** S11 parameters of the proposed probes (1F1L and 1F3L)

It's important to note that the previous investigation's (1F1L) findings are only laying the groundwork for the initial design of the upcoming switchable magnetic probe in the next section.

## 5.5 Switchable Broadband to Tuneable Narrowband Magnetic Probe for Near Field Measurements

The noise source may spread across multiple frequency bands over the DUT. Low-sensitivity broadband probes or high-sensitivity magnetic probes with multiple narrow bands can be used to estimate the EMI at multiple frequency bands. This study introduces a switchable broadband magnetic probe that can be tuned to a narrowband mode for near-field measurement. Based on our investigation results in Section 5.4, a compact wideband magnetic probe has been introduced as a reference sensor for the pre-compliance EMC test in a band up to 6 GHz. Additionally, high sensitivity can be achieved through either an active probe (by connecting a pre-amplifier to the output of a passive magnetic probe) or using the narrowband passive magnetic probe with high sensitivity.

The switching from broadband state to narrowband one is achieved with a PIN diode by interchanging the dimensions of the loop gap resonator (LGR). At the same time, a varactor diode is also employed to fine-tune the narrowband frequency within the 3 – 6 GHz range by reducing the resonator loop's parasitic capacitor. The organization of this work is as follows; **Section 5.5.1** explains the design of the magnetic probe. **Section 5.5.2** presents the parametric study on the LGR dimensions. The biasing circuit of the PIN and varactor diodes is presented in **Section 5.5.3**. **Section 5.5.4** shows the equivalent circuit of the magnetic probe designed in AWR Microwave Studio. Finally, the isolation and sensitivity results of the proposed probe, which are compared with those in the reviewed literature, are demonstrated in **Section 5.5.5**. This section's findings have been published in a journal with a high impact factor [A7].

### 5.5.1 Design of switchable magnetic probe

The proposed magnetic probe is made up of four layers that stick up; 1<sup>st</sup> and 4<sup>th</sup> layers are devoted to working as shielded ground layers to ensure isolation, the 2<sup>nd</sup> layer contains both strip and transmission lines, and the 3<sup>rd</sup> layer is meant to preserve the symmetry of the structure. This probe is constructed using an FR-4 substrate with a relative permittivity of 4.3 and a loss tangent of 0.025. Moreover, Figure 73 provides a detailed view of each layer, while Figure 74 displays the probe dimensions.

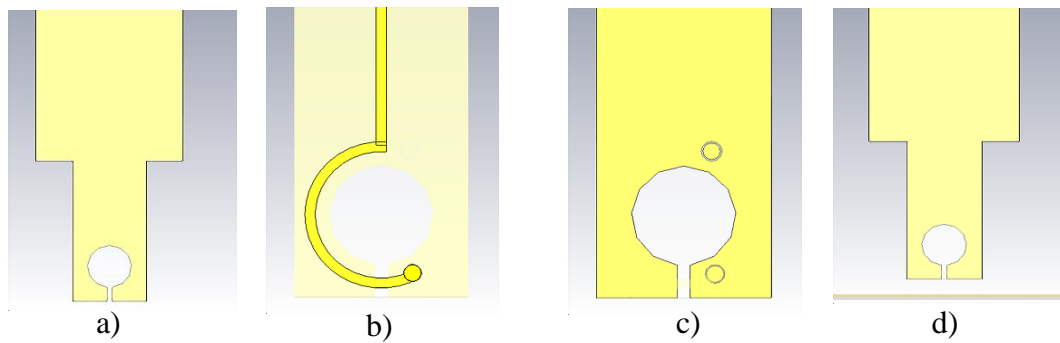


**Figure 73.** Magnetic probe layers: a) Top layer (ground); b) detailed view of the stripline layer; c) detailed view of the symmetry-maintaining layer and d) bottom layer (ground)

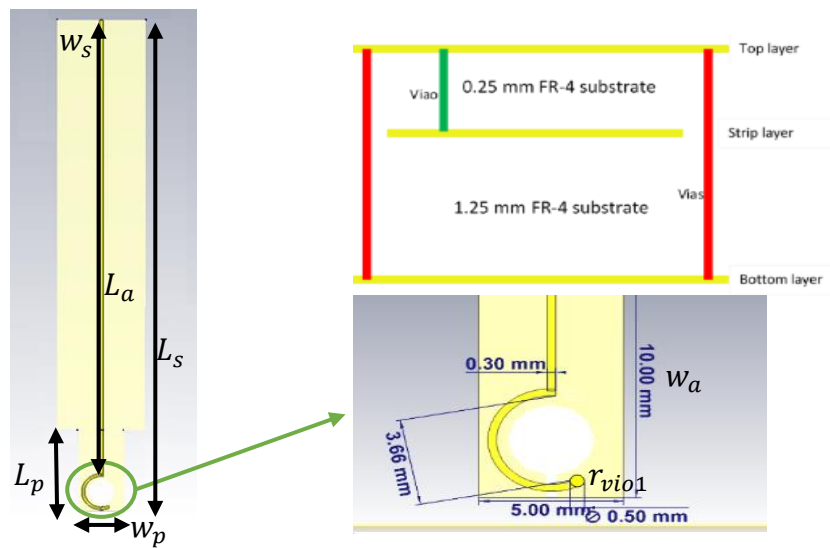


**Figure 74.** Front view of the magnetic probe with all dimensions.

In a typical case with a broadband response, the proposed probe's structure is represented by a LGR, as illustrated in Figure 75. The resonance frequency of the LGR depends on the capacitor of the gap and the inductor of the loop, which can be calculated mathematically using equations (5.15), (5.16) and (5.17) [65].

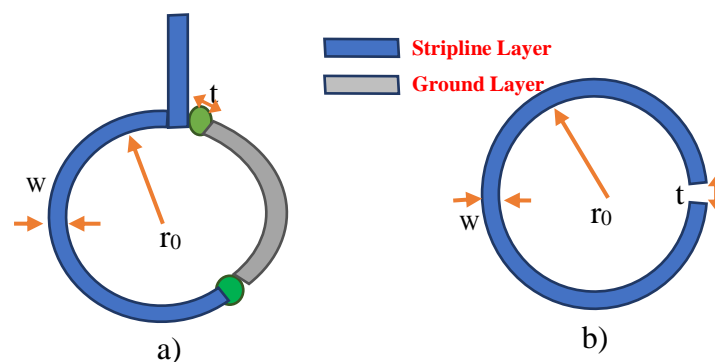


**Figure 75.** Magnetic probe layers: a) proposed probe and b) loop gap resonator (LGR)

$$C = \varepsilon_0 \frac{w l}{n t}, \quad (5.15)$$

$$L = \mu_0 \frac{\pi r^2}{l}. \quad (5.16)$$

Since,

$$f_0 = \frac{1}{2\pi\sqrt{LC}} \quad (5.17)$$

Substituting (1) and (2) in (3) yields:

$$f_0 = \frac{v_0}{2\pi r} \sqrt{\frac{n t}{\pi w}}, \quad (5.18)$$

where  $n$  is the number of gaps in the loop,  $w$  is the strip width in mm,  $r$  represents the probe's radius in mm and  $t$  is the gap width in mm and equal to  $(2 \times r_{via2})$ .

The theoretical resonance frequency  $f_0$  of the LGR is calculated by substituting the probe's parameter values in equation (5.18), where  $w = 0.56$  mm,  $r = 1.7$  mm, and  $t = 0.5$  mm. The resulting  $f_0$  is aligned with the simulated S11 parameter obtained from the

CST Microwave Studio [21], where  $f_0 = \frac{3 \times 10^8}{2\pi \times 1.7 \times 10^{-3}} \sqrt{\frac{0.5 \times 10^{-3}}{\pi \times 0.56 \times 10^{-3}}} = 14.9$  GHz. Figure 76 presents the simulated result of the reflection coefficient versus frequency, while the overall dimensions of the proposed probe are listed in Table 21.

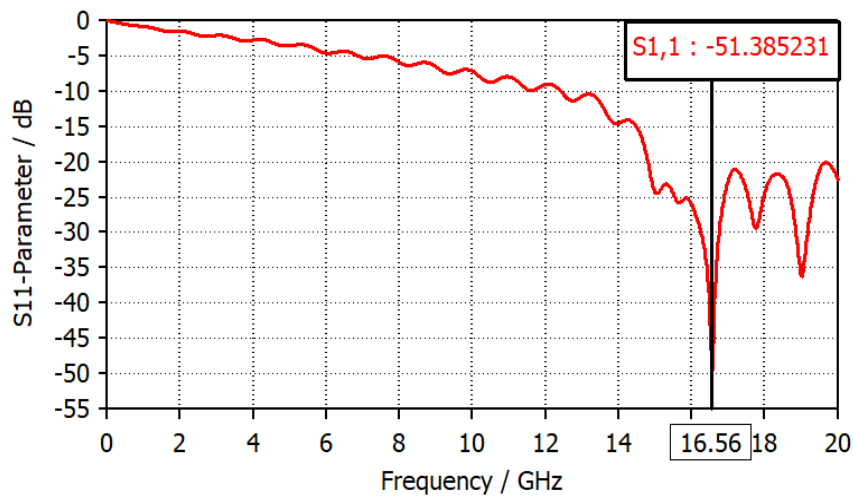


**Figure 76.** Reflection coefficient versus frequency of the LGR

**Table 21.** The overall dimensions of the proposed structure

No.	1	2	3	4	5	6
Parameter	$L_s$	$L_p$	$L_a$	$r$	$r_{via1}$	$r_{via2}$
Value/mm	50	10	48.32	1.5	0.5	0.4
Parameter	$W_s$	$W_p$	$W_a$	$t$	$S$	$d_{via1}$
Value/mm	10	5	0.3	0.8	1.5	2

The best way to look deeply into the probe resonance behavior is by observing the movement of its surface current distribution. Consequently, the surface current distribution of the proposed LGR probe is presented in Figure 77 in both 2D and 3D views. It can be seen that the power flows from the port toward the loop through the transmission line, then moves to the other side through via-1 and back to complete the open circle, as evidenced by the black arrows.

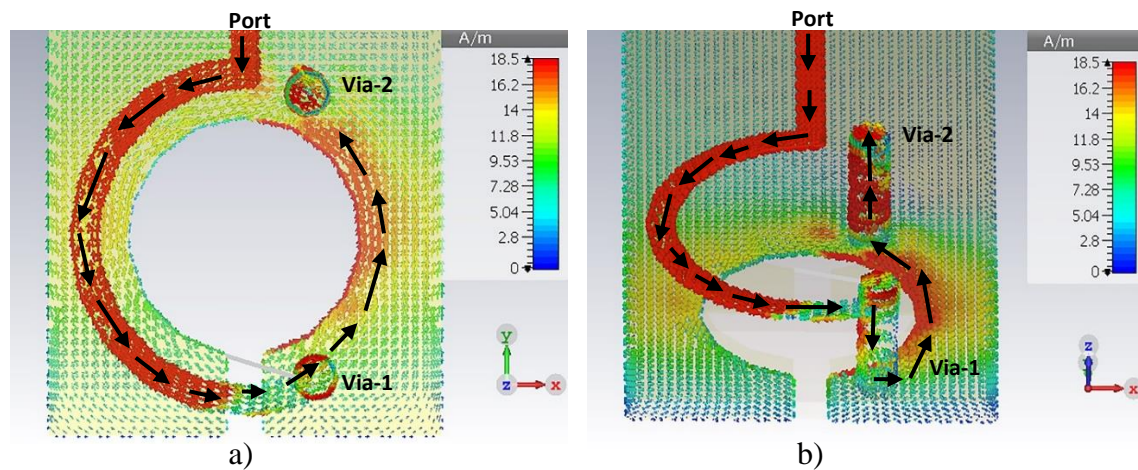


**Figure 77.** The surface current distribution of the broadband magnetic probe: a) top view and b) perspective view

The S11 parameter describes the electrical characteristic of the antenna and determines its usable bandwidth. Furthermore, both the S11 parameter and S21 parameter are critical factors in evaluating the magnetic probe characteristics; the S21 parameter measures the strengths of the magnetic field and the electrical field in the vertical and horizontal directions, respectively. At the same time, the S11 parameter describes the resonance characteristics of the magnetic probe. Unlike the antenna, the magnetic probe operation bandwidth is computed by taking into account several parameters such as sensitivity, accuracy, and resonance characteristics. In this work,  $-3$  dB value of S11 parameter has been taken to determine the operation bandwidth of the proposed broadband magnetic probe [66]. Figure 78 shows the simulated S-parameters of the proposed magnetic probe with a



2 mm height above the trace of the microstrip reference board. It can be seen that this probe has high sensitivity (as  $S_{21} > -27$  dB) in the frequency range from 1 GHz to 3.4 GHz band and starts losing its sensitivity (as  $S_{11} < -3$  dB) beginning at 3.5 GHz and beyond. The proposed magnetic probe has been fabricated based on an FR-4 substrate with the help of the Pragoboard company [67]. Traditional laboratory (EMC lab) with elementary measurement tools like network analyzer, directional coupler and microstrip reference board is utilized to test this probe, as shown in Figure 79 b). Furthermore, the validity of this probe has been performed by comparing its results with the achieved results of the commercial probe (XF-R3-1) offered for sale [68], as presented in Figure 80.

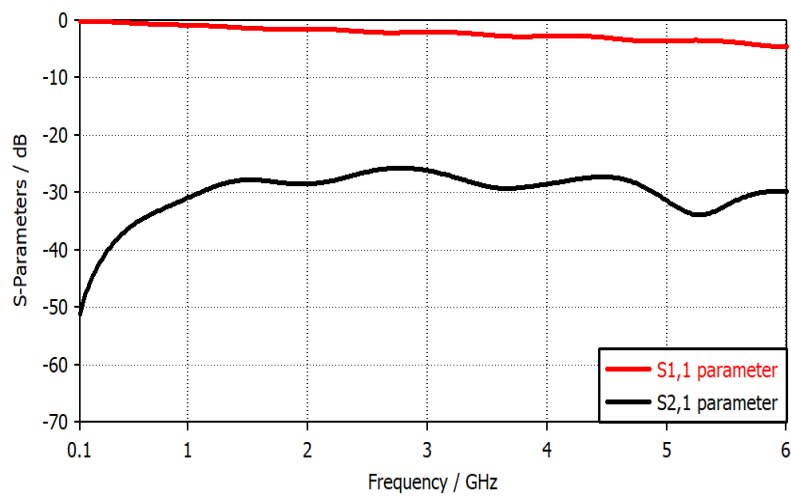


**Figure 78.** S-parameters result of the broadband magnetic probe

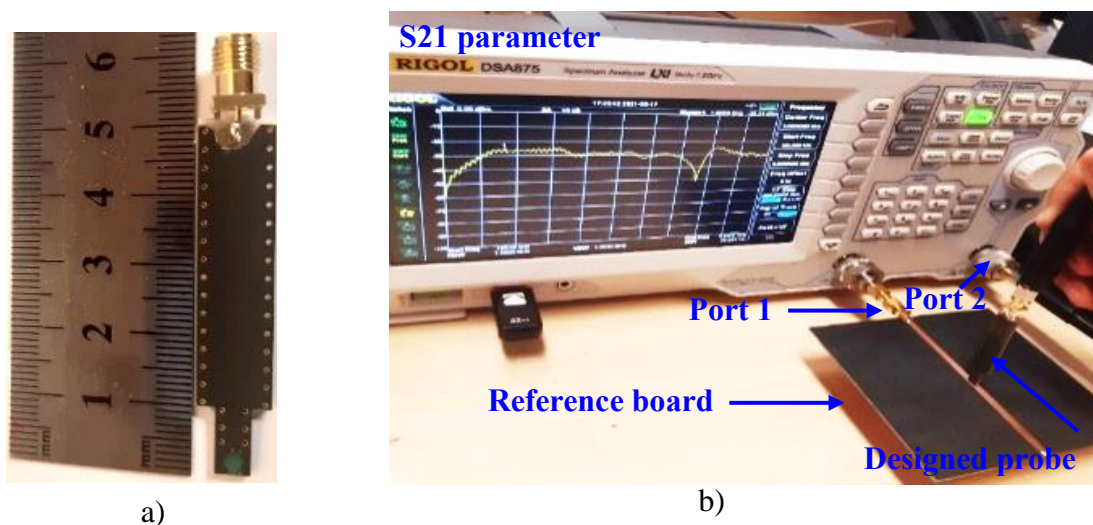


**Figure 79.** Prototype of the magnetic probe: a) dimensions of the probe and b) S21 parameter measurement setup



Figure 80 shows the frequency characteristics of both structures (proposed and commercial designs) regarding  $S_{11}$  and  $S_{21}$  parameters. It can be seen that the proposed broadband magnetic probe exhibits better sensitivity than the commercial XF-R 3-1 magnetic probe. And that makes sense because of the high spatial resolution of the proposed structure (1.6 mm) compared to that of the commercial probe XF-R 3-1 (1 mm).

The band (3.5 – 6 GHz) has relatively low sensitivity and covers several radio frequency applications like WiMAX at 3.5 GHz, 6G mid-band 3.6 – 3.8 GHz, PAN at 4.8, and WLAN at 5.2 GHz. Therefore, enhancing the sensitivity of the magnetic probe in this band will increase its ability to estimate the magnetic field interference with these applications accurately. This issue can be solved using the switchable narrowband magnetic probe with the help of switching techniques listed in [69-71].

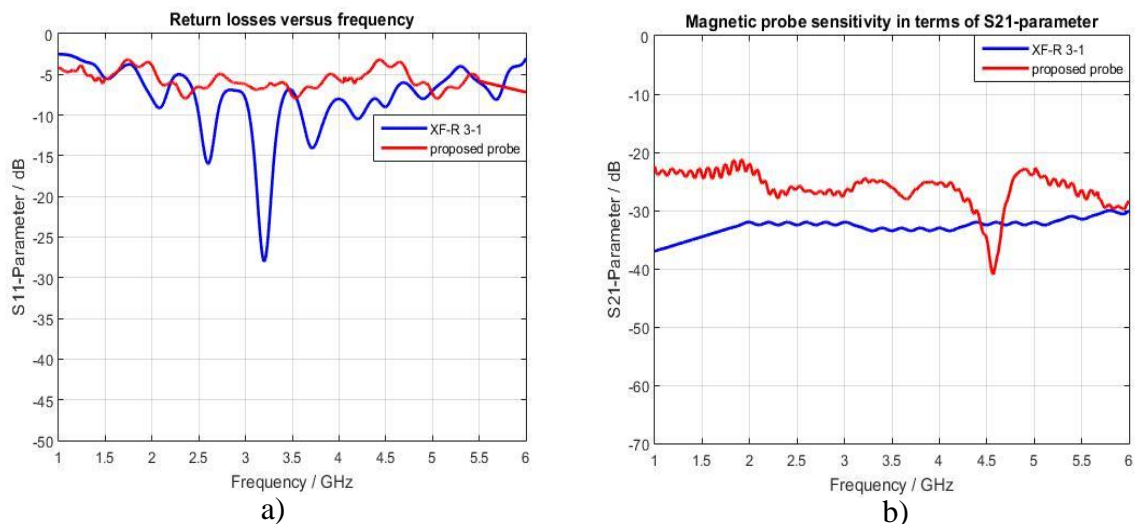


**Figure 80.** S-parameters vs. frequency of the proposed magnetic probe compared with the commercial XF- R3-1: a)  $S_{11}$  parameter and b)  $S_{21}$  parameter

The proposed magnetic probe switches its status from broadband to high-sensitivity narrowband via a PIN-diode type SMP1320-079LF. Moreover, the achieved high-sensitivity narrowband state can also be tuned across the most critical applications with the help of the varactor diode. The PIN diode is inserted between the beginning point of LGR and via-2. Thus, it is responsible for opening and closing the LGR by connecting the other side of the circular arc with the ground layers, as shown in Figure 81.

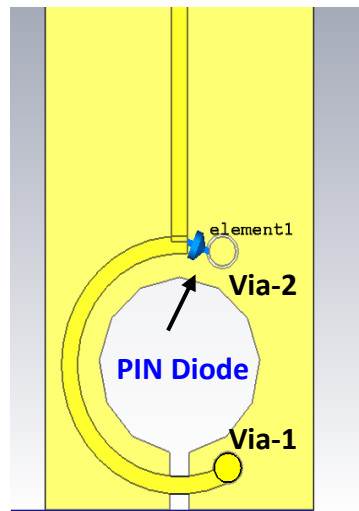


**Figure 81.** Introducing the PIN diode in the broadband magnetic probe

Using the PIN diode will create another surface current direction; the first surface current has a direction from the  $50\ \Omega$  port toward the circular arc and then moves to the other side through via-1, as indicated in the yellow arrows in Figure 82. At the same time, the second current will have the same starting point as the first current and move through via-2 toward via-1 in the opposite direction, forming a circle of surface currents as denoted in the black arrows in Figure 82. As the vias connect the top and bottom layers, there will be two slotted patch gap resonators, one at the top and the other at the bottom. After adding a PIN diode, the LGR was changed to two patch-slotted gap resonators (one on the top and the other on the bottom layers). Figure 82 b) depicts only the bottom layer to provide a clear view.

It is worth mentioning that equations (5.15)-(5.18) are still valid to calculate the resonance frequency of the new structure (two slotted patch gap resonators). The computed operation frequency for only one slotted patch resonator is 13 GHz which is agreeable with the simulated results presented in Figure 83, which also shows another resonance frequency at 5.8 GHz since we have two resonators. More than 6 dB sensitivity enhancement in terms of the  $S_{21}$  parameter has been achieved with the narrowband magnetic probe compared to the broadband structure.

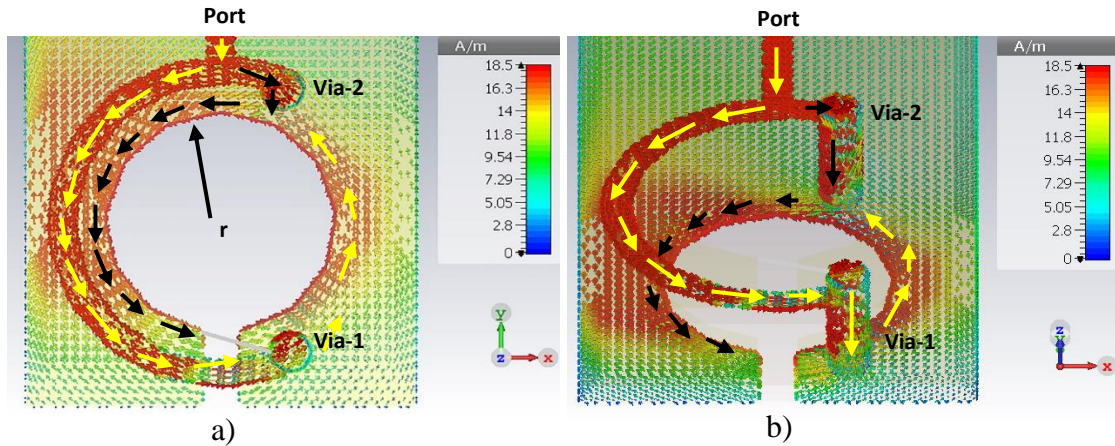


**Figure 82.** The surface current distribution of the narrowband magnetic probe: a) top view and b) perspective view

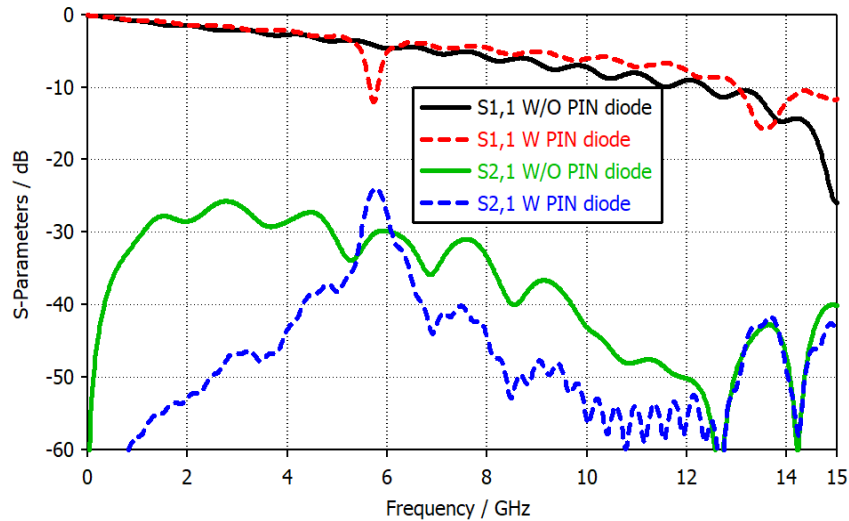


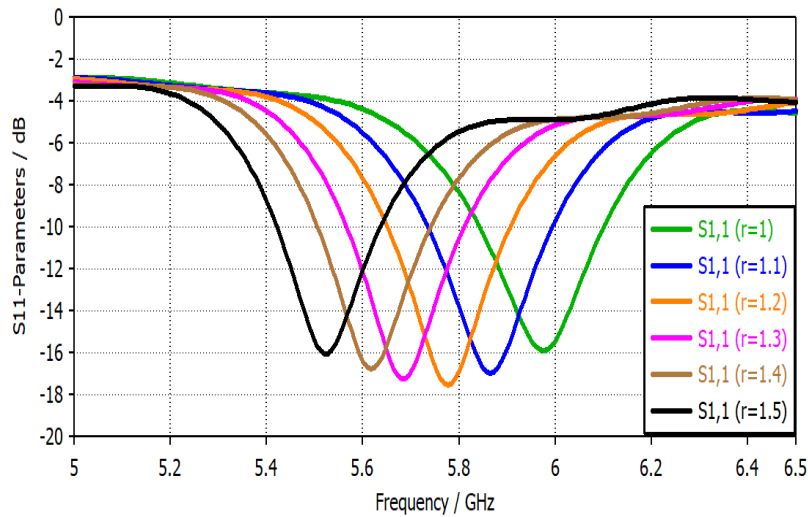
**Figure 83.** S-parameters of the proposed magnetic probe with and without using a PIN diode

### 5.5.2 Parametric study

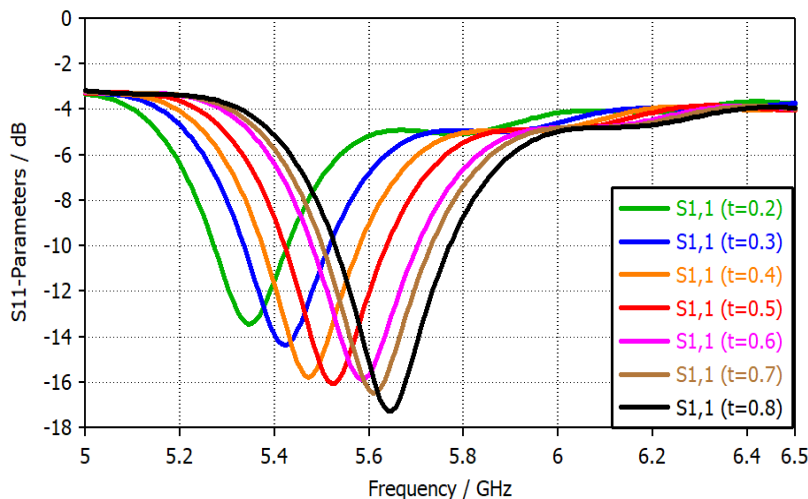
This section will focus on finding the resonance frequency location of the slotted patch gap resonators. Two parameters have been investigated as follows.

The resonance frequency can be adjusted by the slotted circular gap radius  $r$  according to equation (5.18). Figure 84 shows the S11 parameter versus frequency for different values of  $r$ . It can be seen that increasing the radius  $r$  will shift the resonance frequency toward lower bands and vice versa since both the slotted gap radius  $r$  and the frequency  $f$  are inversely proportional to each other.

On the other hand, the slotted gap width  $t$  controls the resonance frequency locations. For instance, increasing the gap width  $t$  will shift the resonance frequency toward higher bands, as shown in Figure 85. However, turning the resonance frequency among the spectrum with the help of  $t$  and  $r$  parameters has inspired the authors to use this advantage and tune the high sensitivity narrowband probe among the critical frequency bands, i.e., WiMAX, PAN, WLAN, etc.



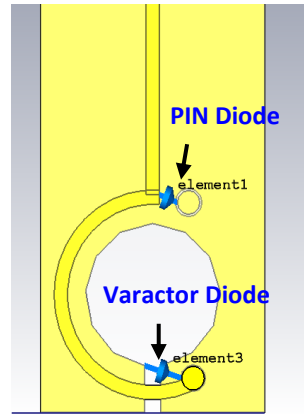
**Figure 84.** S11 parameters of the narrowband magnetic probe for different values of a slotted circle gap radius  $r$



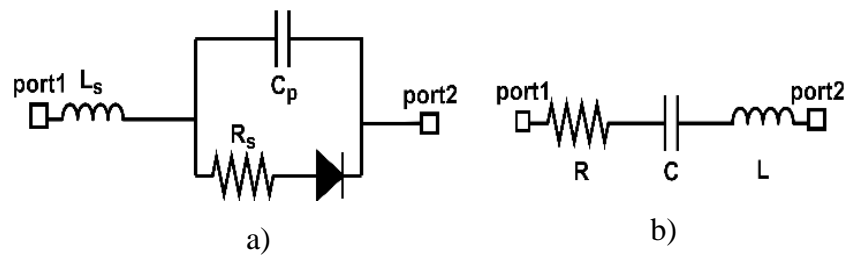
**Figure 85.** S11 parameters of the narrowband magnetic probe for different values of slotted gap width  $t$

Figure 86 presents the geometrical shape upon inserting the varactor diode type SMV2201-040LF between the via-1 and the far side of the slotted patch gap. The varactor

diode will play the same role of changing the width of the opening gap  $t$  by changing the value of the parasitic capacitor. The equivalent circuit of the varactor diode type SMV2201-040LF is presented in Figure 87 in both spice and lumped elements models where  $L_s = 0.45$  nH,  $C_p = 0.075$  pF and  $R_s = 5.41$   $\Omega$ .



**Figure 86.** Use of the PIN diode and varactor diode in the magnetic probe



**Figure 87.** Varactor diode model: a) spice model and b) equivalent circuit

Based on the datasheet of SMV2201-040LF downloaded from the Skyworks website, the parasitic capacitance value will decrease as the reverse biasing voltage increases, as shown in Figure 88.

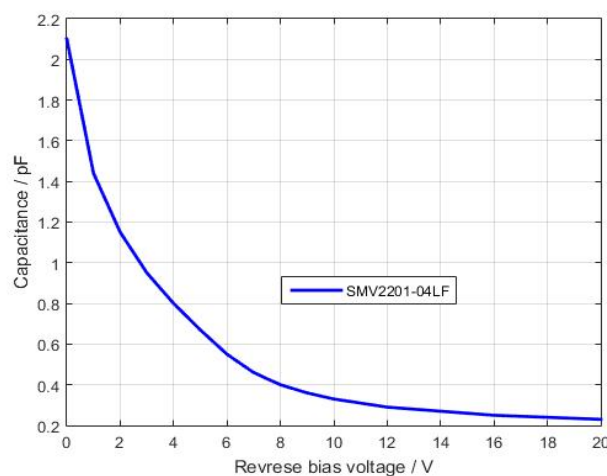


**Figure 88.** Capacitance vs. reverse biasing voltage of SMV2201-040LF

The simulated results of the S-parameters for both broadband and tuned narrowband modes are presented in Figure 89. The sensitivity enhancement of the tuned narrowband mode is about 10 dB compared to the broadband mode through all frequency bands. The prototype of the proposed switchable magnetic probe is shown in Figure 90.

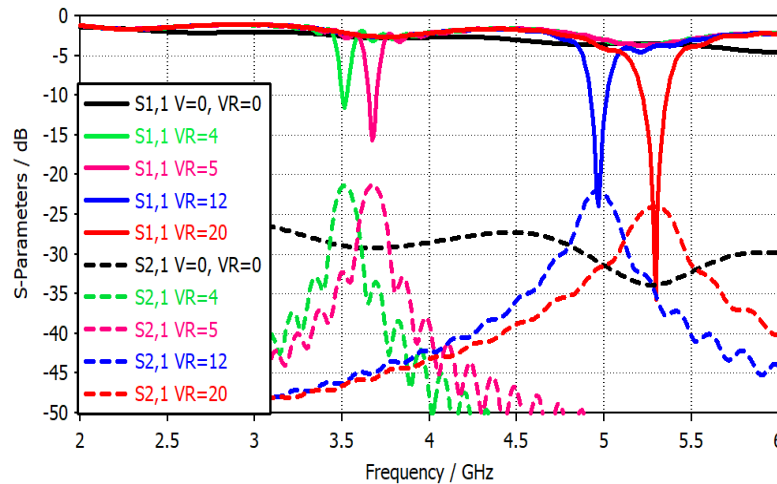


**Figure 89.** S-parameters results for PIN diode and varactor diode switching modes

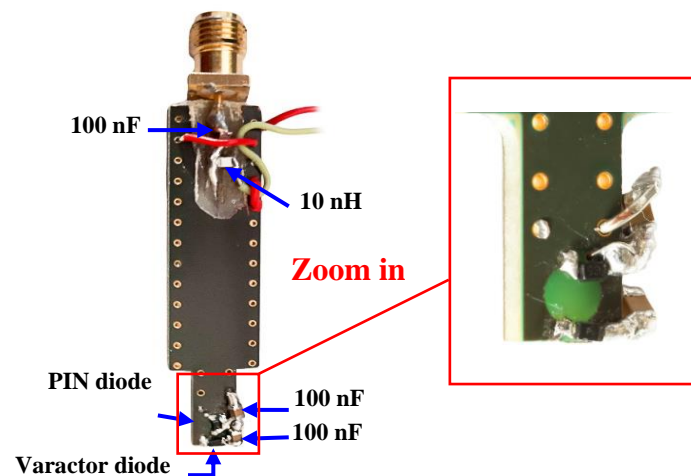


**Figure 90.** Fabricated magnetic probe from the Pragoboard company

### 5.5.3 Biasing circuit and measurement results

This work has two active elements that need biasing; the PIN diode and the varactor diode. The selected PIN diode SMP1320-079LF has a slight forward resistance  $R_f = 0.9 \Omega$  at 10 mA and a reverse biasing capacitance  $C_r = 0.3 \text{ pF}$ . On the other hand, the varactor diode type SMV2201-040LF we utilized has a capacitance range  $C = 0.23 - 2.22 \text{ pF}$ . Figure 91 a) presents the biasing circuit for both the PIN and varactor diodes. Both DC current and RF currents will share the same feeding line. Therefore, three essential passive elements are

involved to ensure the compatibility of these two sources. The choking inductor of  $L_c = 10 \text{ nH}$  prevents radiation leakage from passing through the biasing circuit since it works as a low-pass filter. A  $100 \text{ nF}$  blocking capacitor C1 is necessary to protect the network analyzer from the biasing current. Finally, other  $100 \text{ nF}$  blocking capacitors C2 and C3 are mandatory to prevent the diodes' reverse biasing and protect them from the short circuit since they work as a high pass filter.

The path connecting via-1 and via-2 is part of the ground plane layers and carries DC current. However, this part is involved in the magnetic resonance process as radiated path (part of slotted patch gap resonators), which is why it is connected to the vias. Therefore, two  $100 \text{ pF}$  capacitors are employed to prevent the back DC current for each diode from passing through this radiated path and to protect the diodes from the short circuit by the DC current.

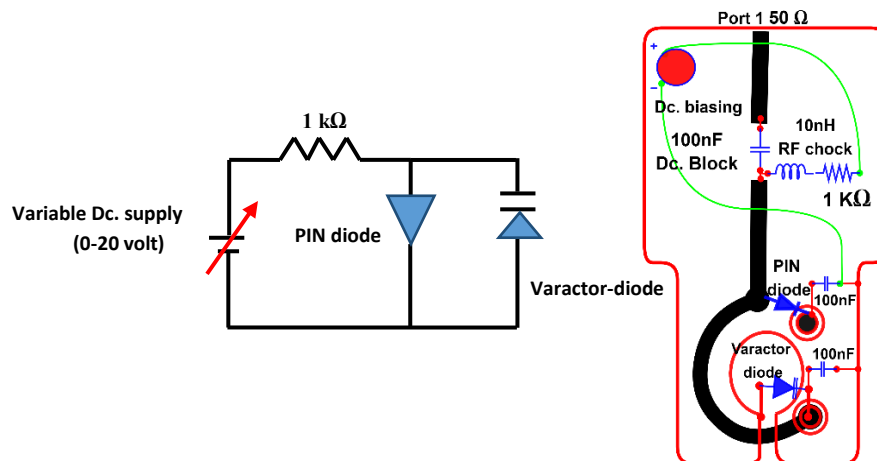


**Figure 91.** The biasing circuit for PIN and varactor diodes

The PIN diode has two states, ON and OFF, to switch between the narrowband and broadband states. At the same time, the varactor diode has a tunable mode to shift the resonance frequency when the PIN diode is in the ON status. Table 22 lists the diode modes with a variable DC voltage supply.

**Table 22.** Lists the diode modes by applying a variable DC supply

No.	1	2	3	4	5
VR / V	0	4	5	12	20
Capacitance / pF	–	0.8	0.7	0.3	0.23
PIN Mode	OFF	ON	ON	ON	ON
Varactor mode	OFF	M1	M2	M3	M4
state / GHz	1 – 6	3.5	3.75	4.8	5.2



An ordinary laboratory with the necessary tools is enough to perform the near-field measurements, which is an advantage compared to the far-field measurements that need chambers. Figure 92 shows the setup of measuring the S11 parameter with the help of the RIGOL DSA875 spectrum analyzer, RIGOL VB 1032 directional coupler, and DC voltage supply for biasing. Moreover, the sensitivity represented by S21 parameter is measured with the help of a microstrip reference board, as depicted previously in Figure 79 b).

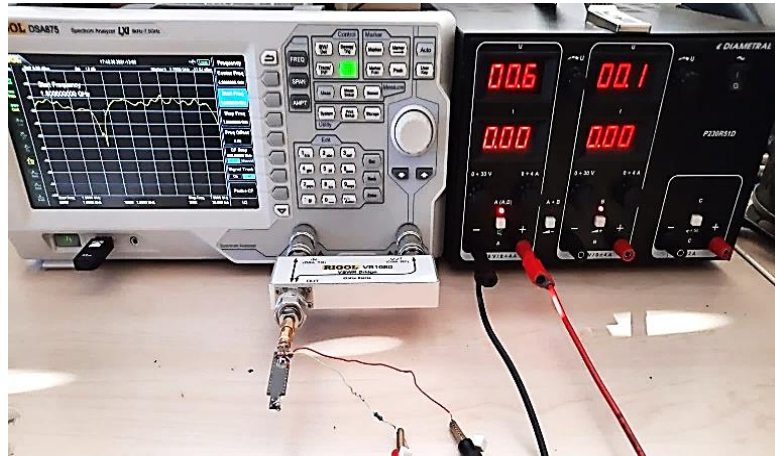


**Figure 92.** S11 parameter measurement with different biasing voltages

Figure 93 presents the measured S-parameters for different switching modes. The achieved resonance frequency bands are three bands instead of four (missing a band at 3.75 GHz), which is due to the biasing voltage value 5 V of band 3.75 GHz being close to that of band 3.5 GHz (4 V). However, the achieved measured band of 3.5 GHz has wider bandwidth than the simulation one due to the merging of these two adjacent bands, as demonstrated in Figure 93 a).

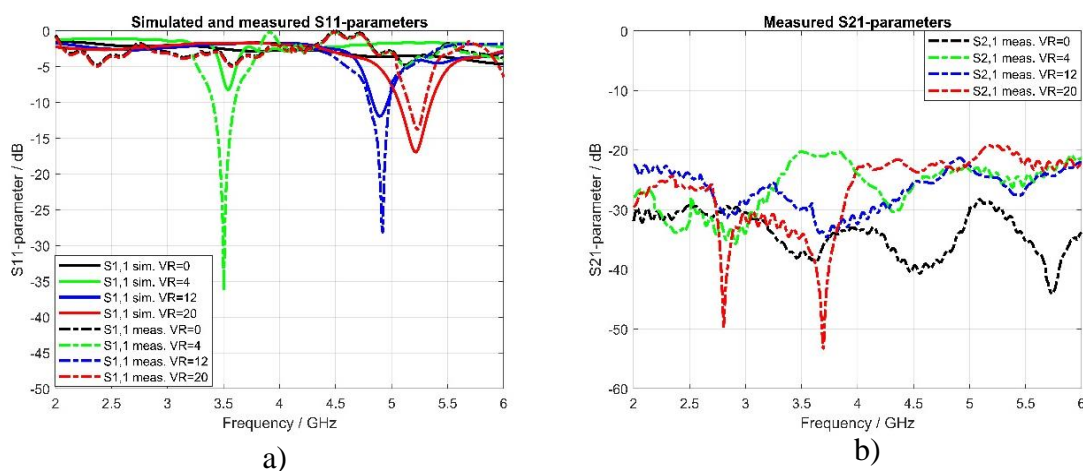


**Figure 93.** The simulated and measured S-parameters vs. frequency with different biasing voltage: a) S11 parameters and b) S21 parameters



The losses of using active elements are noticed by observing the measured sensitivity at the broadband state when the PIN diode is OFF. The estimated sensitivity in measurements is lower than the simulated one obtained in Figure 83 due to adding some losses. Moreover, they must have the same value theoretically, not practically, because one has been performed without active elements, as shown in Figure 83, and the other has been executed with these diodes, as illustrated in Figure 93 b) at  $V_R = 0$  V. Finally, it's worth mentioning that the S11 parameter response has a slight disturbance rather than the particular bands, which has no noticeable effect on the probe function. Moreover, one of the solutions is to use either a quad-band filter or a tunable filter to smooth the response.

#### 5.5.4 Equivalent circuit of the proposed magnetic probe

Lumped-element equivalent circuits are used identically with 3D magnetic probe simulations to observe the corresponding resonance behavior of the studied probe. The equivalent circuit of the proposed magnetic probe has been modeled and simulated using AWR Software [72], as shown in Figure 94 a). While Figure 94 b) presents the S-parameters versus the frequency of this equivalent circuit with different biasing values.

The author starts by modeling the microstrip reference board with an input port of  $50 \Omega$  connected to parallel inductors. On the other hand, the parasitic elements (series inductor, radiation resistance, and parallel capacitor) represent the shielded loop. The first inductor is responsible for controlling the level of the mutual coupling between the microstrip reference board and the tip of the proposed probe, and it has a value of  $L_1 = 0.5$  nH. In contrast, the values of the second inductor (self-inductor) and the self-capacitor are calculated using equations (5.19) and (5.20), respectively. Furthermore, the value of self-capacitance will be affected by the varactor diode's weight of capacitance  $0.23 - 2.22$  pF to control the resonance frequency.

$$L = \mu_r \mu_o r \left( \ln \left( \frac{8 \times r}{w} \right) - 2 \right), \quad (5.19)$$

$$C = \varepsilon_r \varepsilon_o r \left( \ln \left( \frac{8 \times r}{w} \right) - 2 \right). \quad (5.20)$$

where  $\mu_r$  &  $\mu_o$  are the relative and absolute permeabilities,  $\varepsilon_r$  &  $\varepsilon_o$  are the relative and absolute permittivities and  $r$  &  $w$  are the radius and width of the loop with values of  $r = 1.7 \times 10^{-3}$  mm and  $w = 0.56 \times 10^{-3}$  mm.

The calculated self-inductor and self-capacitor using equations (5.19) and (5.20) are  $L = 2.45$  nH and  $C = 0.07$  pF. A blocking capacitor of 100 pF value is connected to one end of the varactor diode, while the second end is connected to the ground layer to isolate the high-frequency currents from the DC currents. An inductor with  $L = 0.5$  nH and  $R = 55 \Omega$  represents the part of the via-1 connecting the varactor diode to the stripline and the 5.35 mm transmission line. Similarly, an inductor with  $L = 0.23$  nH and  $R = 55 \Omega$  represents the via-2 and the small piece of the transmission line connecting the PIN diode to the via-2. Another blocking capacitor of 100 pF connects the PIN diode to the ground plane to protect the magnetic probe from the direct current of the PIN diode. A transmission line with 50  $\Omega$  impedance represents the part of the ground plane connecting via 1 and via 2.

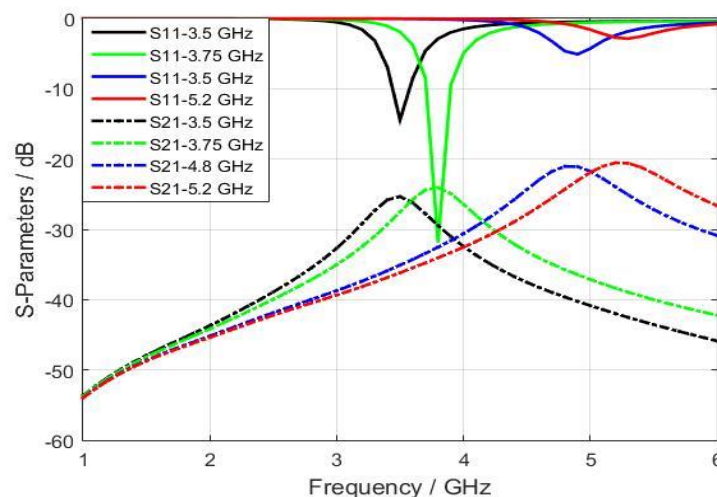
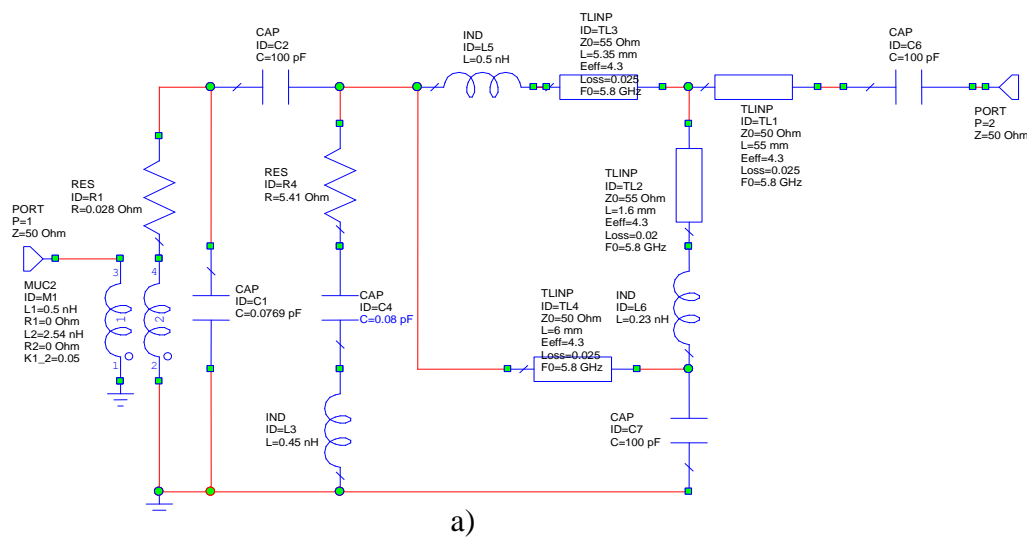


**Figure 94.** Modeling of the magnetic probe in AWR: a) Equivalent circuit of the probe and b) S-parameters vs. frequency with different switching modes

### 5.5.5 Isolation and sensitivity

One of the critical steps in magnetic probe design is to measure the ability of the probe to suppress an undesirable electrical field. The transmission coefficient  $S_{21}$  parameter is utilized to represent the electrical or magnetic fields based on the direction of the sensor related to the reference microstrip trace. Thus, the magnetic field can be estimated when the sensor and the reference trace are in a parallel orientation. On the other hand, the orthogonality case offers the electrical field.

The author utilized the via and fence technology to increase the isolation of the probe against the electrical field. Equal radius vias are distributed at equal distances like a fence around the printed magnetic probe, connecting the top and bottom ground layers. This arrangement will impact the isolation and make the strip line equipotential surface [70].

The center gap of the slotted patch loop in both the top and bottom ground layers has a vital role in isolation due to its location. It creates an open circuit to eliminate the electrical field's tangent component flowing on the surface due to the symmetric distribution. I.e., an unsymmetrical gap will make the magnetic probe more sensitive to the tangential electrical field component due to it not canceling the electrical currents flowing on the outer surface. Figure 95 a) presents the final geometrical shape of the switchable magnetic probe, while Figure 95 b) shows the simulated result of isolation for different switching states. More than 13 dB isolation has been achieved using the via and fence technology.

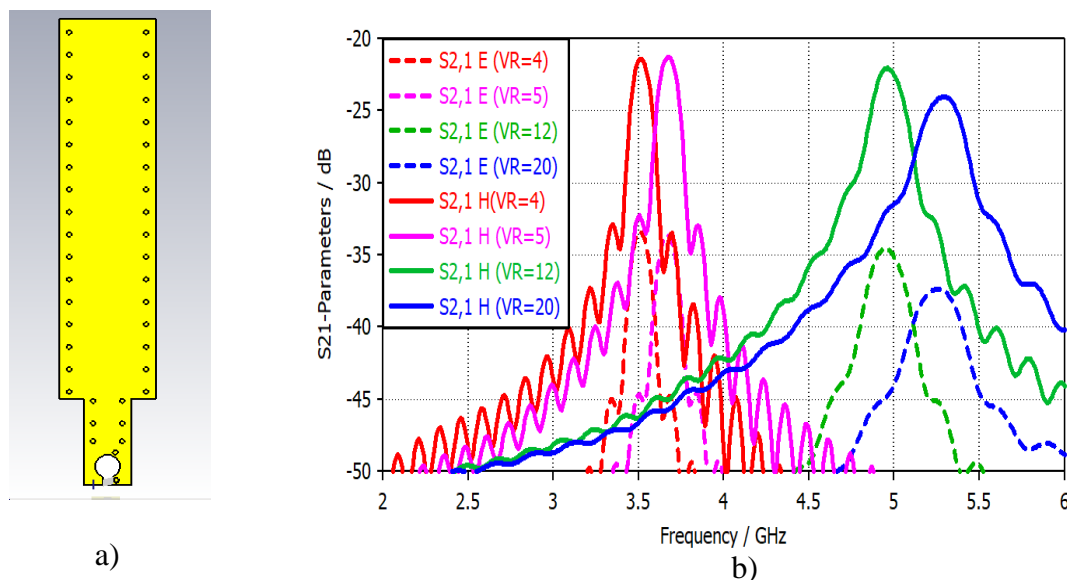


**Figure 95.** Modeling and simulation results of the via fence isolation technique: a) The final geometrical shape of the proposed probe and b) isolation for the multi-narrow bands

To emphasize the role of via-fence technology in sensitivity and isolation enhancements, Figure 96 a) and b) present the simulated results of the sensitivity and isolation with and without using Via-fence technology for different biasing voltage values. It is evident that the via-fence technique considerably impacts isolation and sensitivity. For instance, the via-fence technique has achieved a 5 dB isolation enhancement when comparing the results of Figure 95 b) and Figure 96 a). On the other hand, a sensitivity enhancement of about 5 dB is obtained through critical applications.

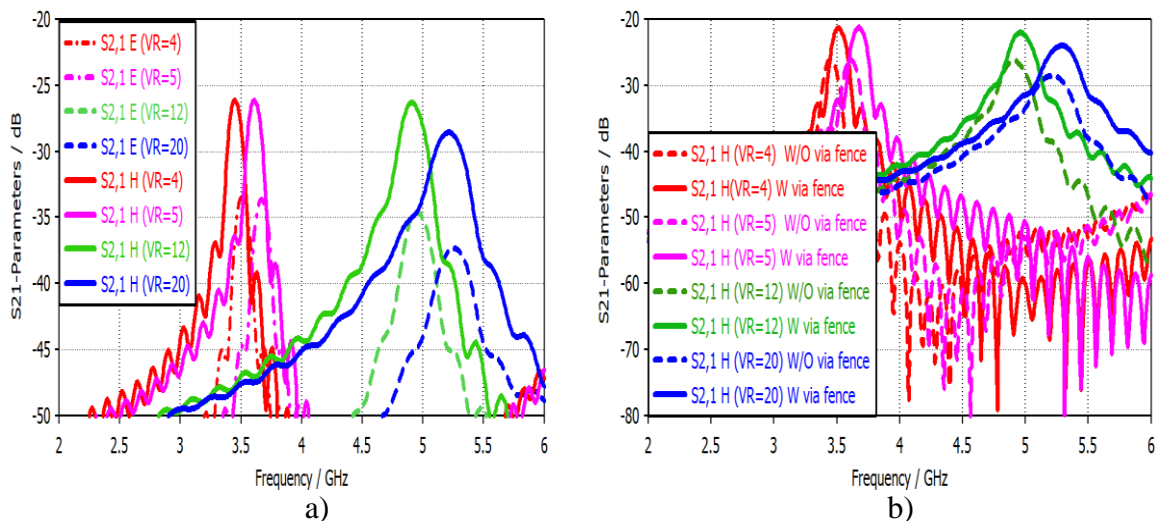


**Figure 96.** S21 parameter simulation results for different biasing voltages: a) isolation in terms of the S21 parameter without using the via fence technique and b) sensitivity enhancement resulting with / without using the via fence technique.

The sensitivity measures the level of the magnetic field distribution above the device under test. Comparing the achieved sensitivity with the previous results in [42], [37], [38], and [39] shows the main contribution of this work. The proposed probe has summed up the benefits of a large bandwidth with high sensitivity compared to the probes described in the literature reviewed, as illustrated in Table 23

**Table 23.** Comparison of the sensitivity enhancement achieved in the proposed work and the literature reviewed

Ref.	Bands / GHz	Design technology	Improvement / dB
[42]	Up to 6	Inverted G-shape inductive line	5
[37]	1.57	LC resonator with Marchand Balun	8.68
[38]	1.57	LC resonators with $\lambda/4$ transformer	6.6
[39]	0.89, 1.7 and 2.2	Reconfigurable rectangular resonator	7 – 9
<b>This work</b>	<b>1 – 3, 3.5, 4.8 and 5.2</b>	<b>Switchable circular resonator</b>	<b>10</b>

## 6 Conclusions

### 6.1 Benefits of the dissertation

This dissertation shows the possibility of using a printed electromagnetic sensor for EMC/EMI measurements instead of the classical ones by considering the EMC specifications. As a result, many problems have been solved. The wide bandwidth increases the possibility of the sensor estimating the possible EMI for a wide range of applications. Conversely, a smaller sensor will have a shorter measurement distance, serving two primary purposes. Firstly, it can decrease the required input power due to the reduced measurement distance, which can also minimize chamber size. Secondly, the small size can help overcome test configuration issues, particularly when the antenna is vertically oriented.

### 6.2 Summary of the achieved results

Five structures of printed electromagnetic sensors for EMC measurements have been designed, fabricated and tested. Three of them are dedicated to the far-field measurement, while the rest are used for the near-field measurement.

In the far-field measurement, the proposed antennas consist of printed structures that mimic classical reference antennas (3D), like biconical, log periodic dipole array, and double ridge horn antennas. These sensors offer wide bandwidth starting from 0.5 GHz to 6.5 GHz with the help of different techniques of bandwidth enhancement and size reduction. Therefore, it has a high probability of collecting the electromagnetic waves emitted from the DUT working in several applications.

Based on the achieved results of the proposed antennas printed biconical dipole (PBD) and printed log-periodic biconical dipole array (PLPBDA), we concluded that the printed antennas design could be a good candidate for EMC measurement instead of the classical antenna if it satisfies the following conditions:

1. It should have wide bandwidth to detect interference with the other devices that operate in the same frequency bands. In particular, the PBD antenna offers bandwidth from 700 MHz to 2.3 GHz with reconfigured high frequencies up to 10 GHz. On the other hand, the PLPBDA antenna presents a bandwidth from 0.6 GHz to 6.5 GHz, covering most microwave frequency bands with a size reduction of 50%.
2. Based on the test type, whether emission or immunity, the antenna should have a directive or omnidirectional radiation pattern to be compatible with the radiation pattern offered by the device under the test. Furthermore, the beamwidth angles of both proposed structures have been compared with the CISPR standards and showed good agreement.

3. It should have a stable and smooth transition from low to high frequencies in both gain and radiation patterns, as shown in the proposed structures' current surface transition versus frequency.
4. It should have a good antenna factor in both value and shape compared to the antenna factor of the classical antenna. The PBD antenna offers a  $24 - 36 \text{ dBm}^{-1}$  antenna factor compared to  $22 - 44 \text{ dBm}^{-1}$  for the commercial biconical antenna BicoLOG® 20300. On the other hand, the PLPBDA antenna exhibits an antenna factor of  $24 - 41 \text{ dBm}^{-1}$  compared to  $26 - 41 \text{ dBm}^{-1}$  for the commercial log periodic antenna HyperLOG® 7060.

The above two structures (PBD and PLPBDA antennas) showed promising results to be a measuring antenna for the radiated emission test. On the other hand, the radiated immunity test requires a directive radiation pattern in both E and H fields. Therefore, a dual-stacked log periodic biconical dipole array (DSL PBDA) antenna has been designed, simulated, fabricated and tested. The proposed 3D structure is derived from the PLPBDA antenna with some modifications of replacing the substrate with air and using two PLPBDA antennas to satisfy the radiation pattern's condition. Consequently, this antenna has taken advantage of the size reduction and bandwidth enhancement offered by PLPBDA, reflecting impedance bandwidth up to 6 GHz and a size of  $160 \times 157 \times 176 \text{ mm}$ . Moreover, this antenna was tested as a transmitting antenna for evaluating UFA points inside the EMC chamber, and the results coincided with the simulation. In particular, the maximum difference from the highest value of the electrical field at a 3 m distance has satisfied the UFA condition (more than 75% of maximum difference in UFA points are in the interval  $\langle 0; -6 \rangle \text{ dB}$ ).

The near-field measurements are necessary to locate the source of the EMI precisely. Therefore, several investigations have been performed on the printed broadband magnetic probes to estimate the EMI in the proximity area of the electronic devices. These investigations have been made to get a comprehensive idea of the procedure to design a suitable printed magnetic probe by considering the challenges in probe parameters like sensitivity, size, bandwidth, antenna factor and isolation of magnetic field. Two spiral circular magnetic probe configurations – two faces three-loops (2F3L) and one face three-loop (1F3L) – are designed and simulated to serve EMI measurements. The microstrip board is used as a reference board with features close to the DUT to validate the results collected from the proposed probe. The (1F3L) probe performs better than (2F3L) because

it has a more selective area. The proposed broadband magnetic probe presents about  $-30$  dB sensitivity with more than 12 dB isolation for the frequency band from 100 MHz to 1 GHz.

A novel high-sensitivity switchable magnetic probe has been designed, simulated, and tested. The proposed magnetic sensor is assigned as a reference probe for EMI measurement. Additionally, this probe boasts two different modes of operation. The first is a broadband mode, which offers good sensitivity across frequencies up to 3.4 GHz. The second mode is a high-tuneable sensitivity mode specifically designed for use with WiMAX, Mid-band 5G, PAN, and WLAN applications up to 6 GHz. The device's switching process relies on a PIN diode to seamlessly transition between the broadband and narrowband modes.

Meanwhile, a varactor diode with reverse biasing is used to sweep the operating point between the four bands 3.5 GHz, 3.75 GHz, 4.8 GHz and 5.2 GHz. Compared to broadband, more than 10 dB has been improved across all these wireless bands. Furthermore, the proposed structure's isolation between the electrical and magnetic fields is about 13 dB. The device's equivalent circuit has been modeled using AWR Microsoft Studio and has demonstrated S- parameter results consistent with the CST EM simulation results.

### 6.3 Recommendations for possible further progress in resresearch (Future work suggestions)

During the evaluation of generations of wireless communications, there is a symmetry between the evolving techniques utilized for far and near-field sensors. i.e., techniques used in one field can apply to the other by considering the field circumstances. Table 24 shows the analogy between the far-field and near-field sensors according to the techniques used.

**Table 24.** Evolution of techniques used for far-field and near-field sensors.

Technology	Far-field sensor	Near-field sensor
Single band	Single band antenna	Single band probe
Dual-band	Dual-band antenna	Dual-band probe
Wideband	Wideband antenna	Wideband probe
Reconfigurability	Reconfigurable antenna	Reconfigurable probe
MIMO	Far-field MIMO systems	Near field MIMO systems
Cognitive radio	Switchable antenna	<b>Novel "Switchable probe."</b>
Filter + antenna	<b>Filtenna</b>	<b>"Future work" is called Filtobe*</b>

One example of that. In Section 5.5, the novel switchable magnetic probe can be considered a reflection of the underlay cognitive radio antenna of sensing and communication. It senses the coupling in the broadband range and switches to a single band for high sensitivity. Another recent trend is to use the filter with an antenna called Filtenna. The Filtenna enlightens us about the possibility of performing the probe with a filter and

creating a new term like” Filtrobe”. This structure has the advantages of smoothing the received coupling power collected from the switchable probe and increasing the sensitivity since we already have a biasing circuit for the probe.

The proposed electromagnetic sensors for far-field and near-field measurements work up to 6 GHz by considering the EMC specifications. However, investigating the EMC measurement for 5G and 6G would be a dessertable topic since all EMC considerations will change accordingly. However, the measurement distance at high frequencies and small radiator size requires a big EMC chamber and is sometimes unrealistic. For instance, a 30 cm radiator element at a millimeter wave (26 GHz) needs a 15.6 m measurement distance.



## References

- [1] X. Wang, X. Chen, X. Shi, Y. Bai, F. Wei, and P. Li, "EMC design for an anti-jamming smart antenna system," in *2009 5th Asia-Pacific Conference on Environmental Electromagnetics*, 2009, pp. 196-199: IEEE.
- [2] C. R. Paul, *Introduction to electromagnetic compatibility*. John Wiley & Sons, 2006.
- [3] K. Zdeněk, N. Denys, K. Pavel, S. Jiří, and H. Miroslav, "Optimization of electrical properties of parallel plate antenna for EMC testing," *Journal of Computational Applied Mathematics*, vol. 270, pp. 283-293, 2014.
- [4] Z. Kubík and J. Skála, "Shielding Effectiveness Simulation of Small Perforated Shielding Enclosures Using FEM," *Energies*, vol. 9, no. 3, p. 129, 2016.
- [5] F. M. Alnahwi, A. A. Abdulhameed, H. L. Swadi, and A. S. Abdullah, "A planar integrated UWB/reconfigurable antenna with continuous and wide frequency tuning range for interweave cognitive radio applications," *Iranian Journal of Science and Technology, Transactions of Electrical Engineering*, pp. 1-11, 2019.
- [6] S. Kovář, V. Mach, J. Valouch, and M. Adámek, "Electromagnetic compatibility of arduino development platform in near and far-field," *International Journal of Applied Engineering Research*, vol. 12, no. 15, pp. 5047-5052, 2017.
- [7] A. Namahoot, P. Akkaraekthalin, and S. Chalermwisutkul, "Design of a low - cost 1 - 20 GHz magnetic near - field probe with FR - 4 printed circuit board," *International Journal of RF and Microwave Computer - Aided Engineering*, vol. 29, no. 12, p. e21958, 2019.
- [8] H. Kawakami, G. Sato, R. Wakabayashi, and K. Shimada, "Conical log-periodic spiral antenna for microwave EMC/EMI measurement," in *IEEE Antennas and Propagation Society International Symposium 1997. Digest*, 1997, vol. 1, pp. 538-541: IEEE.
- [9] C. A. Balanis, *Antenna theory: analysis and design*. John wiley & sons, 2015.
- [10] A. A. Abdulhameed and Z. Kubík, "Investigation of Broadband Printed Biconical Antenna with Tapered Balun for EMC Measurements," *Energies*, vol. 14, no. 13, p. 4013, 2021.
- [11] Q. Wu, X. Ding, and D. Su, "A compact dipole antenna with curved reflector for 1.0–4.2 GHz EMC measurement," *IEEE Transactions on Electromagnetic Compatibility*, vol. 57, no. 6, pp. 1289-1297, 2015.
- [12] I. E. C. CISPR16-1-2, "Specification for radio disturbance and immunity measuring apparatus and methods-Part 1-2: Radio disturbance and immunity measuring apparatus-Ancillary equipment-Conducted disturbances," 2006.
- [13] S. Z. Sapuan, A. Kazemipour, and M. Z. M. Jenu, "Direct feed biconical antenna as a reference antenna," in *2011 IEEE International RF & Microwave Conference*, 2011, pp. 5-8: IEEE.
- [14] J. McLean, R. Sutton, and R. Hoffman, "Interpreting antenna performance parameters for EMC applications: Part 3: Antenna Factor," *TDK RF Solutions Inc*, 2004.
- [15] M. G. Alijani, S. Sheikh, and A. Kishk, "Development of Closed-Form Formula for Quick Estimation of Antenna Factor," in *2021 15th European Conference on Antennas and Propagation (EuCAP)*, 2021, pp. 1-5: IEEE.
- [16] N. Sivaraman, K. Jomaa, and F. Ndagijimana, "Three dimensional scanning system for near-field measurements," in *2017 11th European Conference on Antennas and Propagation (EUCAP)*, 2017, pp. 2866-2870: IEEE.
- [17] N. Sivaraman, F. Ndagijimana, M. Kadi, and Z. Riah, "Broad band PCB probes for near field measurements," in *In 2017 International Symposium on Electromagnetic Compatibility-EMC EUROPE 2017*, pp. 1-5: IEEE.
- [18] N. Sivaraman, "Design of magnetic probes for near field measurements and the development of algorithms for the prediction of EMC," Doctoral dissertation, Optics / Photonic, Université Grenoble Alpes, 2017.
- [19] S.-Y. Lin, S.-K. Yen, W.-S. Chen, and P.-H. Cheng, "Printed magnetic field probe with enhanced performances," in *2009 Asia Pacific Microwave Conference*, 2009, pp. 649-652: IEEE.
- [20] P. A. Martinez *et al.*, "Design and study of a wide-band printed circuit board near-field probe," *Electronics*, vol. 10, no. 18, p. 2201, 2021.
- [21] C. M. J. C. S. T. Studio, "3D EM Simulation software," 2014.
- [22] K.-C. Kim, B. J. Choi, and S. W. Jung, "Characteristics of the Sleeve Dipole Antenna Used for EMC Applications," *IEEE Access*, vol. 8, pp. 86957-86961, 2020.

- [23] J. Bang, C. Han, K. Jung, and J. Choi, "High-Frequency Performance Improvement of LPDA for EMC/EMI Measurements," in *2020 International Symposium on Antennas and Propagation (ISAP)*, 2021, pp. 621-622: IEEE.
- [24] H. Kawakami, M. Tanioka, and R. Wakabayashi, "Circularly Polarized Log Periodic Dipole Antennas," in *2020 International Applied Computational Electromagnetics Society Symposium (ACES)*, 2020, pp. 1-2: IEEE.
- [25] M. Gerber, J. W. Odendaal, and J. Joubert, "DRGH Antenna With Improved Gain and Beamwidth Performance," *IEEE Transactions on Antennas and Propagation*, vol. 68, no. 5, pp. 4060-4065, 2019.
- [26] N. Gupta and A. Haque, "Design of printed log periodic EMI sensor," *Int. J. Microw. Optical Tech*, vol. 4, no. 4, pp. 211-215, 2009.
- [27] T. Limpiti and A. Y. Chantaveerod, "Design of a printed log-periodic dipole antenna (LPDA) for 0.8–2.5 GHz band applications," in *2016 13th International Conference on Electrical Engineering/Electronics, Computer, Telecommunications and Information Technology (ECTI-CON)*, 2016, pp. 1-4: IEEE.
- [28] L. Yu, S. Chai, H. Huang, L. Ding, K. Xiao, and F. Zhao, "A printed log-periodic dipole antenna with balanced feed structure," in *2016 Progress in Electromagnetic Research Symposium (PIERS)*, 2016, pp. 2035-2038: IEEE.
- [29] A. Kyei, D.-U. Sim, and Y.-B. Jung, "Compact log-periodic dipole array antenna with bandwidth-enhancement techniques for the low frequency band," *IET Microwaves, Antennas & Propagation*, vol. 11, no. 5, pp. 711-717, 2017.
- [30] K. K. Mistry, P. I. Lazaridis, Z. D. Zaharis, T. D. Xenos, E. N. Tziris, and I. A. Glover, "An optimal design of printed log-periodic antenna for L-band EMC applications," in *2018 IEEE International Symposium on Electromagnetic Compatibility and 2018 IEEE Asia-Pacific Symposium on Electromagnetic Compatibility (EMC/APEMC)*, 2018, pp. 1150-1155: IEEE.
- [31] K. Anim and Y.-B. Jung, "Shortened log-periodic dipole antenna using printed dual-band dipole elements," *IEEE Transactions on Antennas and Propagation*, vol. 66, no. 12, pp. 6762-6771, 2018.
- [32] K. K. Mistry, P. I. Lazaridis, Q. Ahmed, Z. D. Zaharis, T. H. Loh, and I. P. Chochliouros, "A printed LPDA antenna with improved low frequency response," in *2020 XXXIIIrd General Assembly and Scientific Symposium of the International Union of Radio Science*, 2020, pp. 1-4: IEEE.
- [33] D. Douzhang, F. Shang, and A. Pingpei, "A Small Dual Stacked Log Periodic Dipole Array Antenna as a Feed for Reflector Antennas," in *2021 International Conference on Microwave and Millimeter Wave Technology (ICMMT)*, 2021, pp. 1-3: IEEE.
- [34] H. Funato and T. Suga, "Magnetic near-field probe for GHz band and spatial resolution improvement technique," in *2006 17th International Zurich Symposium on Electromagnetic Compatibility*, 2006, pp. 284-287: IEEE.
- [35] D. Baudry, A. Louis, and B. Mazari, "Characterization of the open-ended coaxial probe used for near-field measurements in EMC applications," *Progress In Electromagnetics Research*, vol. 60, pp. 311-333, 2006.
- [36] J.-M. Kim, W.-T. Kim, and J.-G. Yook, "Resonance-suppressed magnetic field probe for EM field-mapping system," *IEEE transactions on microwave theory and techniques*, vol. 53, no. 9, pp. 2693-2699, 2005.
- [37] H. H. Chuang *et al.*, "A Magnetic-Field Resonant Probe With Enhanced Sensitivity for RF Interference Applications," (in English), *Ieee Transactions on Electromagnetic Compatibility*, vol. 55, no. 6, pp. 991-998, Dec 2013.
- [38] G. H. Li, K. Itou, Y. Katou, N. Mukai, D. Pommerenke, and J. Fan, "A Resonant E-Field Probe for RFI Measurements," (in English), *Ieee Transactions on Electromagnetic Compatibility*, vol. 56, no. 6, pp. 1719-1722, Dec 2014.
- [39] S. Shinde, S. Marathe, G. H. Li, R. Zoughi, and D. Pommerenke, "A Frequency Tunable High Sensitivity H-Field Probe Using Varactor Diodes and Parasitic Inductance," (in English), *Ieee Transactions on Electromagnetic Compatibility*, vol. 58, no. 1, pp. 331-334, Feb 2016.
- [40] Z. W. Yan, J. W. Wang, W. Zhang, Y. S. Wang, and J. Fan, "A Simple Miniature Ultrawideband Magnetic Field Probe Design for Magnetic Near-Field Measurements," (in English), *Ieee Transactions on Antennas and Propagation*, vol. 64, no. 12, pp. 5459-5465, Dec 2016.
- [41] R. Yang, X. C. Wei, Y. F. Shu, and Y. B. Yang, "A High-Frequency and High Spatial Resolution Probe Design for EMI Prediction," (in English), *Ieee Transactions on Instrumentation and Measurement*, vol. 68, no. 8, pp. 3012-3019, Aug 2019.

- [42] J. H. Bang, Y. T. Park, K. B. Jung, and J. H. Choi, "A Compact Low-Cost Wideband Shielded-Loop Probe With Enhanced Performance for Magnetic Near-Field Measurements," (in English), *Ieee Transactions on Electromagnetic Compatibility*, vol. 62, no. 5, pp. 1921-1928, Oct 2020.
- [43] S. S. Zhekov, A. Tatomirescu, and G. F. Pedersen, "Modified biconical antenna for ultrawideband applications," in *2016 10th European Conference on Antennas and Propagation (EuCAP)*, 2016, pp. 1-5: IEEE.
- [44] L.-C. Kuo, H.-R. Chuang, Y.-C. Kan, T.-C. Huang, and C.-H. Ko, "A study of planar printed dipole antennas for wireless communication applications," *Journal of Electromagnetic Waves and Applications*, vol. 21, no. 5, pp. 637-652, 2007.
- [45] D. Uduwawala, "A comprehensive study of resistor-loaded planar dipole antennas for ground penetrating radar applications," Doctoral dissertation, School of Electrical Engineering (EES), Electromagnetic Engineering., KTH, Stockholm, 2006.
- [46] P. M. Proudfoot, "A printed circuit folded dipole with integrated balun," ROME AIR DEVELOPMENT CENTER GRIFFISS AFB NY1989.
- [47] M. R. Islam, "Study and Implementation of Wideband Bow-Tie Antennas," Master of Science in Applied Engineering (M.S.A.E.), Department of Electrical Engineering, 2017.
- [48] S. Z. Sapuan, F. H. Herie, and M. Z. M. Jenu, "A new small sized wideband biconical antenna for Electromagnetic Compatibility (EMC) measurements," in *2016 IEEE Asia-Pacific Conference on Applied Electromagnetics (APACE)*, 2016, pp. 222-225: IEEE.
- [49] T. Tuovinen and M. Berg, "Impedance dependency on planar broadband dipole dimensions: An examination with antenna equivalent circuits," *Progress In Electromagnetics Research*, vol. 144, pp. 249-260, 2014.
- [50] S. Z. Sapuan, M. Z. M. Jenu, and A. Kazemipour, "Calibration of calculable wideband direct feed biconical antenna for EMC measurements," in *2013 Asia-Pacific Symposium on Electromagnetic Compatibility (APEMC)*, 2013, pp. 1-4: IEEE.
- [51] J. McLean, R. Sutton, and R. Hoffman, "Interpreting Antenna Performance Parameters for EMC Applications Part 1: Radiation Efficiency and Input Impedance Match," *TDK RF Solution Inc*, 2007.
- [52] A. Shop. *BicoLOG 20300*. Available: <https://aaronia-shop.com/products/biconical-antenna-bicolog-20300>.
- [53] D. Isbell, "Log periodic dipole arrays," *IRE transactions on antennas and propagation*, vol. 8, no. 3, pp. 260-267, 1960.
- [54] R. DuHamel and D. Isbell, "Broadband logarithmically periodic antenna structures," in *1958 IRE International Convention Record*, 1966, vol. 5, pp. 119-128: IEEE.
- [55] R. Carrel, "The design of log-periodic dipole antennas," in *1958 IRE International Convention Record*, 1966, vol. 9, pp. 61-75: IEEE.
- [56] B. Ivšić, F. Frišćić, M. Dadić, and D. Muha, "Design and Analysis of Vivaldi Antenna for Measuring Electromagnetic Compatibility," in *2019 42nd International Convention on Information and Communication Technology, Electronics and Microelectronics (MIPRO)*, 2019, pp. 491-495: IEEE.
- [57] A. Shop. (2023, 10-3-2023). *HyperLOG® 7060*. Available: <https://aaronia-shop.com/products/broadband-antenna-hyperlog7060>
- [58] A. A. Abdulhameed and Z. Kubik, "Design and Modelling of Printed Log Periodic Dipole Array Antenna with Different Feeding Methods," in *International Conference on Applied Electronics*, 2022, vol. 2022-September.
- [59] J. Smith. (2019). *Antenna Selection for IEC 61000-4-3*. Available: <https://absolute-emc.com/article/antenna-selection-for-iec-61000-4-3>
- [60] I. E. Commission. (2020). *Electromagnetic compatibility (EMC) - Part 4-3 : Testing and measurement techniques - Radiated, radio-frequency, electromagnetic field immunity test*. Available: <https://webstore.iec.ch/publication/59849>
- [61] S. R. Patre, S. Singh, and S. Singh, "Effect of dielectric substrate on performance of planar trapezoidal toothed log-periodic antenna," in *2013 Students Conference on Engineering and Systems (SCES)*, 2013, pp. 1-4: IEEE.
- [62] A. A. Abdulhameed and Z. Kubík, "Design a Compact Printed Log-Periodic Biconical Dipole Array Antenna for EMC Measurements," *Electronics*, vol. 11, no. 18, 2022.
- [63] S. M. E. OHG. (2021, 8-1-2023). *STLP 9129 - Stacked Log. Periodic Antenna*. Available: <https://www.schwarzbeck.de/en/component/content/article/38-stacked-logarithmic-periodic-broadband-antennas/292-stlp-9129-stacked-log-periodic-antenna.html>
- [64] S. M.-. ELEKTRONIK. (2007, 8-1-2023). *STLP 9149 - Stacked Microwave Log.-Per. Antenna*. Available: <https://www.schwarzbeck.de/en/antennas/logarithmic-periodic-broadband-antennas/stacked->

[logarithmic-periodic-broadband-antennas/278-stlp-9149-stacked-microwave-log-periodic-antenna.html?highlight=WzkxNDld](https://doi.org/10.1109/antennas.2021.9542914)

- [65] J. S. Bobowski, "Using split-ring resonators to measure the electromagnetic properties of materials: An experiment for senior physics undergraduates," (in English), *American Journal of Physics*, vol. 81, no. 12, pp. 899-906, Dec 2013.
- [66] A. A. Abdulhameed and Z. Kubik, "Design and Modeling of Spiral Circular Magnetic Probe for Near Field Measurements in CST Microwave Studio," presented at the 2021 International Conference on Applied Electronics (AE), 2021.
- [67] P. s.r.o. (2012). *PragoBoard s.r.o.* Available: <https://www.pragoboard.cz>
- [68] L. E.-T. GmbH. (2023, 19-6-2023). *XF-R 3-1 H-Field Probe 30 MHz up to 6 GHz*. Available: <https://www.langer-emv.de/en/download/34/278/22/xf-r-3-1-h-field-probe-30-mhz-up-to-6-ghz.pdf>
- [69] F. M. Alnahwi, K. M. Abdulhasan, and N. E. Islam, "An Ultrawideband to Dual-Band Switchable Antenna Design for Wireless Communication Applications," *IEEE Antennas and Wireless Propagation Letters*, vol. 14, pp. 1685-1688, 2015.
- [70] M. Nejatijahromi, M. Naghshvarianjahromi, and M. Rahman, "Switchable Planar Monopole Antenna between Ultra-Wideband and Narrow Band Behavior," *Progress In Electromagnetics Research Letters*, vol. 75, pp. 131-137, 2018.
- [71] N. Jacob, M. Kulkarni, and K. K., "An electronically switchable UWB to narrow band antenna for cognitive radio applications," *Microwave and Optical Technology Letters*, vol. 62, no. 9, pp. 2989-3001, 2020.
- [72] C. A. D. Environment, "IN AWR Microsoft Studio ", 14.8 ed, 2014.

## List of Student's Publications and Outputs related to the Dissertation

- [A1] Abdulhameed, A.A.: Design and modeling of spiral circular magnetic probe for near field measurements in CST Microwave Studio. In *Elektrotechnika a informatika 2020*. Elektrotechnika, elektronika, elektroenergetika. Plzeň: Západočeská univerzita v Plzni, 2020. s. 1-4. ISBN: 978-80-261-0949-5.
- [A2] Abdulhameed, A.A. and Kubík, Z.: Investigation of Broadband Printed Biconical Antenna with Tapered Balun for EMC Measurements. *Energies* 2021, 14, 4013. <https://doi.org/10.3390/en14134013>.
- [A3] Abdulhameed, A.A. and Kubík, Z.: Design and Modeling of Spiral Circular Magnetic Probe for Near Field Measurements in CST Microwave Studio," 2021 International Conference on Applied Electronics (AE), 2021, pp. 1-4, doi: 10.23919/AE51540.2021.9542914.
- [A4] Abdulhameed, A.A.: Design a Printed Log-Periodic Dipole Array Antenna for EMC Measurements. In *Elektrotechnika a informatika 2021*. Elektrotechnika, elektronika, elektroenergetika. Plzeň: Západočeská univerzita v Plzni, 2021. s. 1-4. ISBN: 978-80-261-1019-4.
- [A5] Abdulhameed, A.A. and Kubík, Z.: Design and Modelling of Printed Log Periodic Dipole Array Antenna with Different Feeding Methods," *2022 International Conference on Applied Electronics (AE)*, Pilsen, Czech Republic, 2022, pp. 1-4, doi: 10.1109/AE54730.2022.9919886.
- [A6] Abdulhameed, A.A. and Kubík, Z.: Design a Compact Printed Log-Periodic Biconical Dipole Array Antenna for EMC Measurements. *Electronics*. 2022; 11(18):2877. <https://doi.org/10.3390/electronics11182877>.
- [A7] Abdulhameed, A.A. and Kubík, Z.: Switchable Broadband-to-Tunable Narrowband Magnetic Probe for Near-field Measurements. *Sensors*. 2022; 22(19):7601. <https://doi.org/10.3390/s22197601>.

- [A8] A. A. Abdulhameed and Z. Kubík, "Using of LPDA Antenna for UFA Evaluation in Radiated Immunity Test," 2023 International Conference on Applied Electronics (AE), Pilsen, Czech Republic, 2023, pp. 1-4, doi: 10.1109/AE58099.2023.10274237.

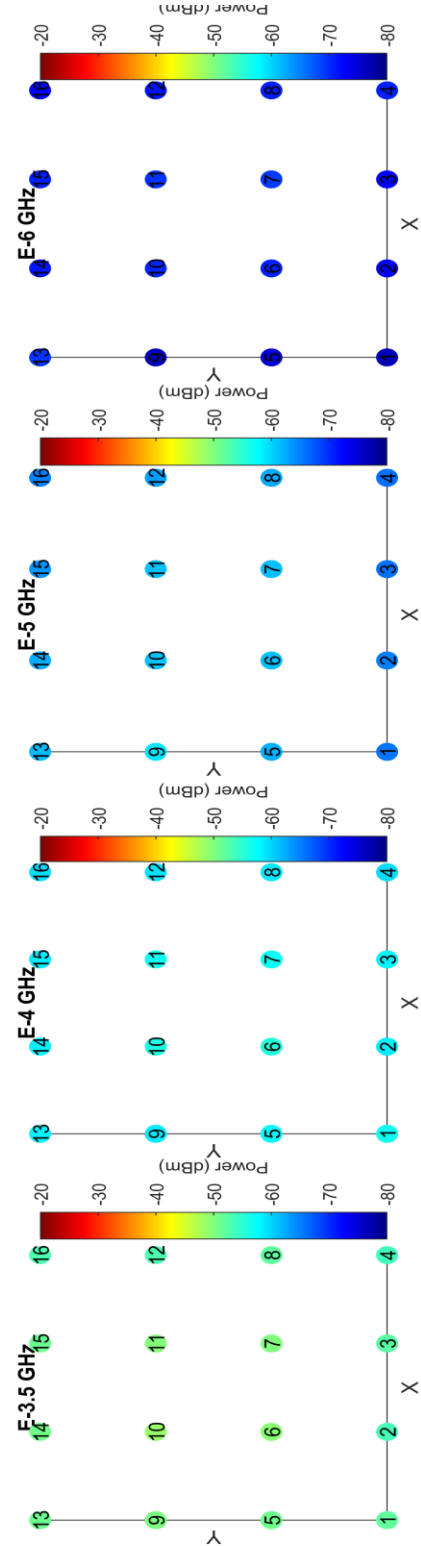
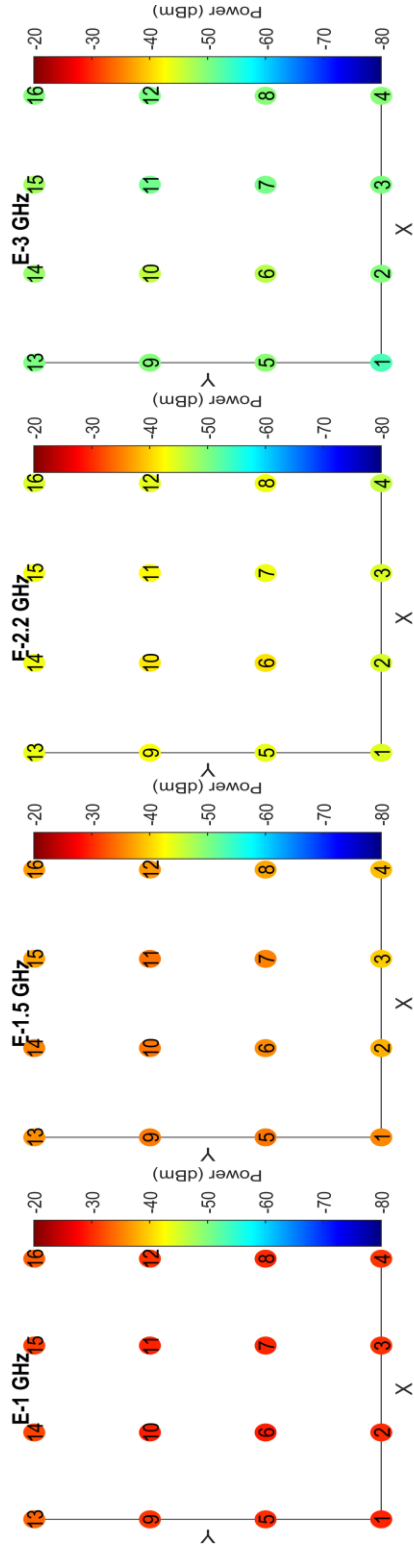
## Other Student's Publications and Outputs

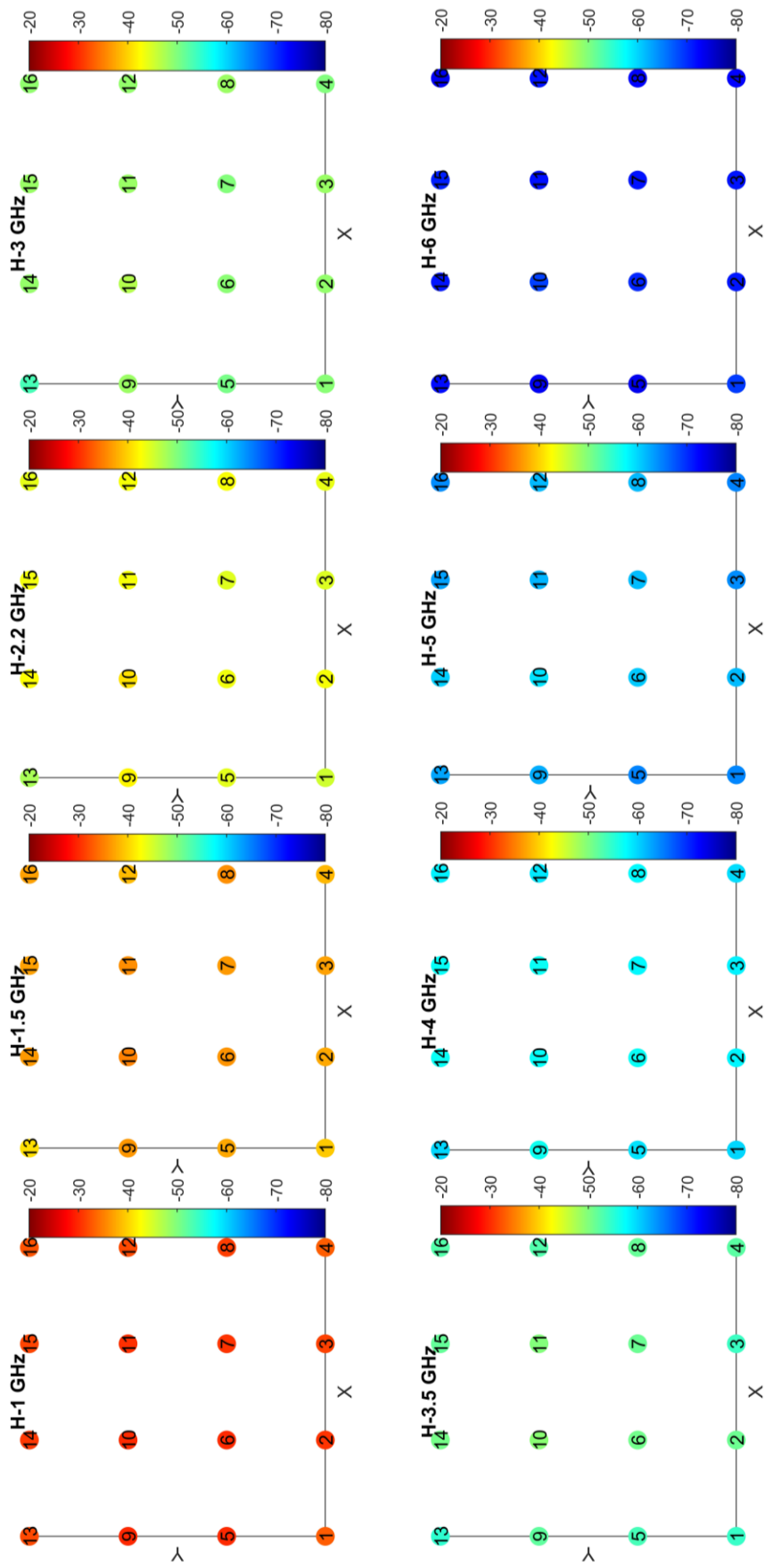
- [B1] SIAHKAMARI, H., JAHANBAKSHI, M., AL-ANBAGI, H. N. A., Abdulhameed, A.A., POKORNÝ, M., LINHART, R.: Trapezoid-shaped resonators to design compact branch line coupler with harmonic suppression. *AEU-INTERNATIONAL JOURNAL OF ELECTRONICS AND COMMUNICATIONS*, 2022, roč. 144, č. February 2022, s. 1-8.
- [B2] Abdullah, A. S., Sadeq, A. H., Al-Anbagi, H., & Abdulhameed, A. A. (2021): Power efficient wideband power LNA for WSN. *IOP Conference Series. Materials Science and Engineering*, 1076(1) doi:<https://doi.org/10.1088/1757-899X/1076/1/01201>.
- [B3] Abdulhameed, A.A., Falih M. Alnahwi, Haidar N. Al-Anbagi, Zdeněk Kubík & Abdulkareem S. Abdullah (2022): Frequency reconfigurable key-shape antenna for LTE applications, *Australian Journal of Electrical and Electronics Engineering*, DOI: [10.1080/1448837X.2022.2112316](https://doi.org/10.1080/1448837X.2022.2112316).
- [B4] Abdulhameed, A.A., Alnahwi, F. M., & Abdullah, A. S. (2023): Dual-band open-loop monopole (2×1) printed MIMO antenna for 4G and 5G applications. *Frequenz*, (0).
- [B5] Juma'a, F. K., Al-Mayoof, A. I., Abdulhameed, A.A., Alnahwi, F. M., Al-Yasir, Y. I., & Abd-Alhameed, R. A. (2022): Design and implementation of a miniaturized filtering antenna for 5G mid-band applications. *Electronics*, 11(19), 2979.
- [B6] H. Jalalian, H. N. Al-Anbagi, M. Jahanbakhshi and A. A. Abdulhameed, "A Compact and Wideband Wilkinson Power Divider Using Lowpass Microstrip Filters," 2023 International Conference on Applied Electronics (AE), Pilsen, Czech Republic, 2023, pp. 1-6, doi: 10.1109/AE58099.2023.10274379.
- [B7] Falih M. Alnahwi, Abdulhameed, A.A., Nazar T. Ali, Yasir I. A. Al-Yasir, Zdeněk Kubík, Abdulkareem S. Abdullah, and Raed A. Abd-Alhameed: A Compact Filtering Antenna with Step and Continuous Tuning Modes for WiMAX Cognitive Radio Communication, sent for publication to the IEEE Access.

## List of Functional Samples

- [1] ALMTROD, A. A. A., KUBÍK, Z. Složená logaritmicko-periodická anténa, 2023.
- [2] ALMTROD, A. A. A., KUBÍK, Z. Sada PCB antén pro měření v elektromagnetické kompatibilitě, 2023.
- [3] ALMTROD, A. A. A., KUBÍK, Z. Přepínatelná magnetická sonda blízkého pole a referenční mikropásková deska, 2023.

Annex A

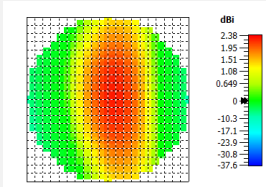
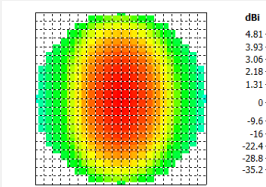
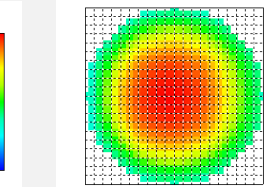
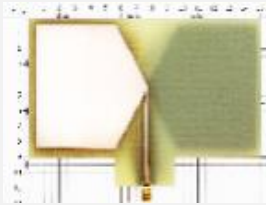








**Annex B**

**Proposed antennas for EMC measurements (far-field)**

Specifications	PBD antenna	PLPBDA antenna	DSL PBDA antenna
Frequency / GHz	0.7 – 2.3	0.6 – 6	0.8 – 6
Design methodology	$x$ (Basic design)	$12 \times x$	Double ( $12 \times x$ )
EMC applications	Fast evaluation of background noise in OATS	Radiated Emission	Radiated immunity
Radiation pattern / E-plane	Omnidirectional	Directive	Directive
Radiation pattern / H-plane	Omnidirectional	Omnidirectional	Directive
Projection of 3-D radiation pattern $\frac{x^2}{a^2} + \frac{y^2}{b^2} = r^2$			
	$a \gg b$ e.g., 3 times	$a > b$ , e.g., 1.5 times	$a = b$
	Gain / dBi	2.38	4.81
Picture			

**Proposed magnetic probes for EMC measurements (near-field)**

Specifications	Circular spiral magnetic probe	Tunable to Switchable Magnetic probe
Frequency / GHz	0.1 – 1	1 – 6
Design methodology	$x$ (Basic design circular loop)	Based on the 3 <sup>rd</sup> investigation results of ( $x$ )
EMC applications	Near field sensor	Pre-compliance test
Picture	